MECHANICS, VIBRATIONS, AND TENSION MEASUREMENT OF THIN WEBS IN ROLL-TO-ROLL MANUFACTURING FOR FLEXIBLE AND PRINTED ELECTRONICS

by

Dan Feng

A Dissertation

Submitted to the Faculty of Purdue University

In Partial Fulfillment of the Requirements for the degree of

Doctor of Philosophy

School of Mechanical Engineering

West Lafayette, Indiana

May 2021

THE PURDUE UNIVERSITY GRADUATE SCHOOL

STATEMENT OF COMMITTEE APPROVAL

Dr. Arvind Raman, Chair

School of Mechanical Engineering

Dr. George T. C. Chiu

School of Mechanical Engineering

Dr. Liang Pan

School of Mechanical Engineering

Dr. Mukerrem Cakmak

School of Materials Engineering

Approved by:

Dr. Nicole Key

ACKNOWLEDGMENTS

I could not have completed my work at Purdue University without the support from many people who deserve recognition. First and foremost, I am so grateful to my advisor, Professor Arvind Raman for his advice, support, and encouragement during my Ph.D. study. The skillset I obtained through his mentorship, both in research and personal conduct, is the treasure of my life. I want to express my deep gratitude to Professor Charles M. Krousgrill for the mentorship and guidance to help me become a better educator. I would like to thank Professor George T. C. Chiu, Professor Liang Pan, and Professor Mukerrem Cakmak for serving on my Ph.D. committee. I appreciate Professor Ryan Wagner for the helpful discussions and assistance in writing. I thank all other lab members, Devin Kalafut, Nurul Huda Shaik, Denise Cruise, Maria Jose Cadena, Bahram Rajabifar, Yuri Efremov, and Professor Ronald Reifenberger, for the helpful discussions, mental support, and friendship. I thank Jie Wang for his excellent work in research collaboration as well as Guy Telesnicki for training me to use commercial roll-to-roll systems.

I am grateful to my parents Kanyu Feng and Yuan Fang, and my uncle Renfei Feng. I could not have persisted till the end of my Ph.D. study without their support and endless love. I would also like to thank my friends for providing a joyful time.

Financial support of this research was provided by the National Science Foundation through grant number CMMI-1344654 and Professor Arvind Raman's Robert V. Adams Professorship. I acknowledge the copyright permission by Elsevier and ASME for re-using published articles in this dissertation.

TABLE OF CONTENTS

LIST OF TABLES

LIST OF FIGURES

ABSTRACT

Roll-to-roll processes provide a low-cost and high-throughput scheme for scalable flexible devices manufacturing. Multiple processes are used in roll-to-roll manufacturing, such as functional printing, evaporation/drying, UV curing, hot embossing, laser/heat annealing, laser ablation, plasma/ chemical growth, and sputtering. These processes change the web temperature field and/ or local properties. In addition, residual stresses by the process and web tension can destabilize the process and lead to wrinkling or undesirable performance of the products.

This dissertation investigates three different multi-physics problems relevant to the roll-to-roll processes, which are web thermomechanics, air-coupled web vibrations, and the measuring of nonuniform web tension. First, a mathematical model for predicting the in-plane temperature and heat induced stress distributions in a flexible, axially moving web under arbitrary shape of heat flux is presented. The computational approach is validated on experiments performed on moving paper and PET webs with infrared laser heating source. Second, a closed-form, semi-analytical, universal hydrodynamic functions is developed to accurately predict the lowest symmetric and anti-symmetric transverse frequency responses for any uniaxially tensioned web of arbitrary material and aspect ratio used in roll-to-roll processes with the surrounding air acting as distributed added mass. Experimental validation is carried out by using pointwise laser measurements of acoustically excited webs with different pre-tensions, web materials, and aspect ratios. Finally, we develop and test a non-contact resonance method and a gentle contact stiffness mapping method based on the first principles mechanical models of a tensioned plate to accurately measure the average web tension and its linear variation for a wide range of web properties, web path, web tension, measurement configurations, and environmental conditions. The two methods are cross−validated on a stationary test stand and the non-contact resonance method is used to study the web tension distribution within a commercial roll-to-roll system.

1. INTRODUCTION

1.1 Background

Bendable, foldable, and lightweight flexible thin films are broadly applied in human wearable devices [1-3], optoelectronics [4-12], thin film transistors [13-16], supercapacitors [2, 17-19], flexible displays [20-23], and sensors for Internet of Things [3, 24-33]. The growing interest in these applications requires highly reliable and repeatable products and spawns the roll-to-roll (R2R) processes for high-volume manufacturing of flexible devices with a potential global market exceeding US $41.3 Billion in 2023 [34]. Figure 1.1 shows some existing and potential applications by R2R manufacturing.

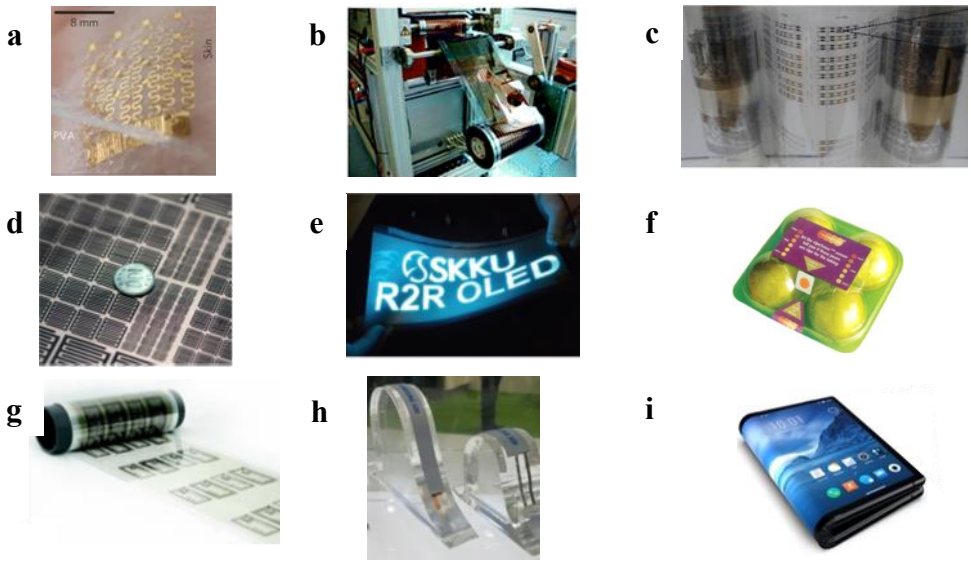

Figure 1.1. Existing and potential flexible thin film devices by R2R manufacturing: (a) thermal sensors adhered on skin (reproduced from [1] with permission from Nature Materials), (b) solar cell (reproduced from [6] with permission from the Royal Society of Chemistry), (c) dielectric layer of thin film transistors (reprinted Organic Electronics, 12, Noh, J. et al., Integrable single walled carbon nanotube (SWNT) network based thin film transistors using roll-to-roll gravure and inkjet, 2187, copyright (2011), with permission from Elsevier), (d) finger patterned supercapacitor [18], (e) organic light emitting diodes (reproduced from [23] with permission from the Royal Society of Chemistry), (f) *ripeSense*® the world's first smart ripeness indicator label for food packaging (reproduced from [24] with permission from Sensing and Instrumentation of Food Quality and Safety), (g) 13.56-MHz-operated 1-bit RF tags [25], (h) flexible batteries by Samsung SDI Division (photo courtesy of Samsung Corp.), (i) the world's first commercial foldable smartphone FlexPai (photo courtesy of Royole Corp.).

Figure 1.2(a) shows a sketch of multi-span R2R platform. Underlying substrates such as PET, PEN, and polyimide are released from an unwind roller, processed on the spans crossing internal rollers, and collected on a rewind roller. Toques are applied on the unwind and rewind rollers for creating a web tension and a web speed. Multiple processes are used in R2R manufacturing, such as functional printing [2-4, 6, 8, 10, 11, 13-16, 19-23, 25-33], evaporation/drying [3, 4, 6, 11, 13, 15, 19, 20, 22, 23, 25, 26, 28-32], UV curing [16, 22, 23, 25, 27, 33], hot embossing [33], laser /heat annealing [2, 21, 18, 29], laser ablation [14], plasma /chemical growth [10, 17, 35, 36], sputtering [5, 7, 21], and the measurements for quality controls [12, 37-40]. All these processes act on the web of a R2R system in the forms of heat, mass, and /or momentum fluxes and strongly affect the web local physical properties, such as temperature, crystal directions, mass, thickness, and surface roughness *etc*., as shown in Figure 1.2(b). On the other hand, these process-induced thermomechanics and vibrations of these webs and the residual stresses caused by pre-applied web tension are essential for ensuring process stability and product quality [41, 42].

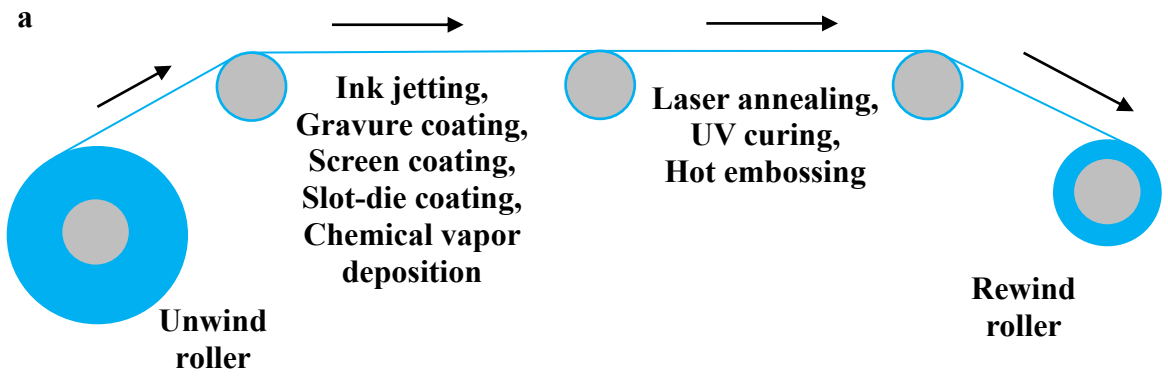

Figure 1.2. (a) A sketch of multi-span R2R platform, (b) a flexible axially moving web under various R2R processes for flexible electronics.

Figure 1.2 continued

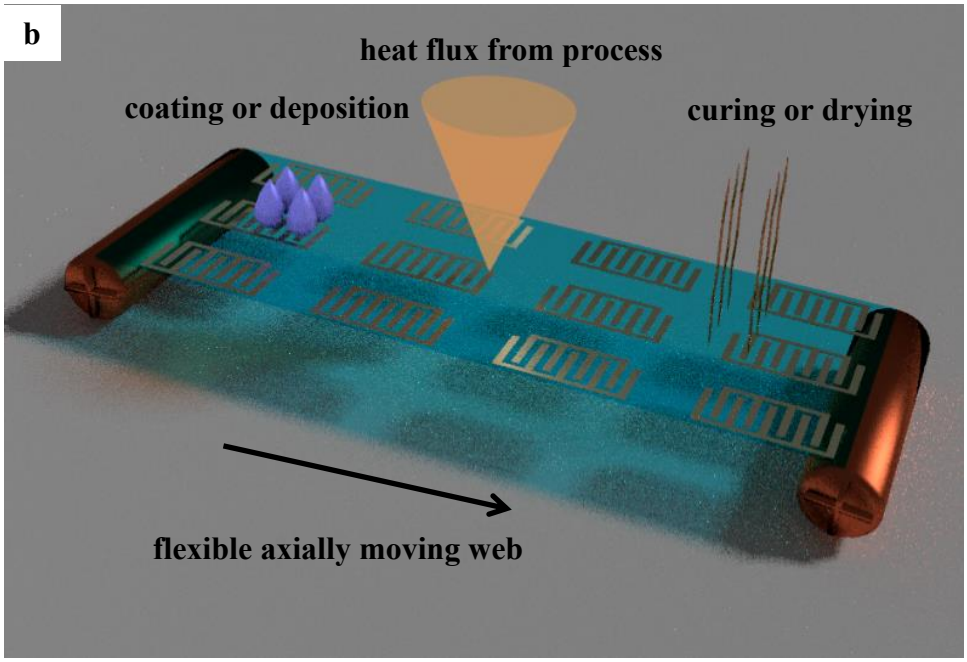

1.2 Literature Review

We briefly review the literature in thermal, vibrations, and tension measurement methods in this section. Previous works on thermal problems of axially moving media has mostly focused on thermoelastic vibration, tension control, and pure heat transfer. A thermal bending moment caused by spatially fixed temperature profile is included in the vibration of an axially moving beam [43-50]. The tension feedback control in a multi-span R2R system involves time-varying temperature by considering a temperature-dependent strain [51-56]. The pure heat transfer problem was investigated with assumptions with either uniform cross-width temperature [57, 58] or a constant film coefficient for the heat exchange between the media and surroundings [59, 60]. These works either study 1-D thermomechanics problems or only include part of the heat exchange mechanisms. Overall, accurate simulation tools for predicting the in-plane 2-D thermomechanics of webs are not available in the above works.

Web vibrations in R2R processes have been studied in the context of web vibration control, vibration-based in-line monitoring, and air-coupled web vibrations. Web systems designers are

interested in ensuring that the web frequencies are tuned away from the unexpected resonance by external excitation sources in the R2R process [61-63], such as inkjet firing frequency and roller-eccentricity induced boundary excitation frequencies. On the other hand, intentional excitation is used for web pre-tension measurement [39, 40] and rapid in-line reliability monitoring [12, 64]. The vibrations of thin flexible webs in R2R processes for flexible devices are significantly affected by surrounding air, which can reduce the frequencies and change the mode shapes in comparison to those *in vacuo*. The air-coupled web vibrations were firstly investigated using potential flow theory for the surrounding air and a uniaxially tensioned membrane model for the web [65, 66]. A uniaxially tensioned Kirchhoff plate model is used later since it defines the spatial dependence of eigenmodes in the direction transverse to the tension [67-72]. However, all these previous works for air-coupled web vibrations require significant computational work to determine the effect of surrounding air on the web vibration. As such these computational approaches are not easily accessible to web systems designers and operators.

The web tension measurement methods have been investigated using instrumented rollers, fundamental vibration frequency, and polynomial fitting or machine learning. Instrumented rollers are the most common tension measurement tools in R2R industry [73-75]. These methods typically assume the web tension is uniform. They need investment in customized rollers, do not include the friction between instrumented rollers and webs, and need re-calibration when web path changes. In addition, these sensors tend to shift and are sensitive to operation environment, such as temperature and vibrations [76]. Fundamental vibration frequency measurements are used in the literature without considering non-uniform web tension and the effect of air loading [38, 40, 77-79]. Using polynomial fitting or machine learning do not need to consider the air loading effect; however, they only used limited web properties (e.g. web line speed, web tension, materials, and web aspect ratios) in their database [40, 79, 80]. Training a universal model is not available and would require extensive amounts of training data. Overall, comprehensive, accurate, reliable, and inexpensive methods for measuring nonuniform web tension in R2R processes are an unsolved problem.

1.3 Contributions of This Dissertation

To improve the process control and product quality in R2R manufacturing, we investigate three different aspects of multi-physics R2R processes. First, the thermomechanics for

understanding the in-planes temperature and stress distributions of the web during R2R processes is studied to predict the thermal residual stress and prevent over /less heating and /or web wrinkling. Second, we discuss the web vibrations with the effect of air loading to web frequencies and mode shapes, which might be used to avoid harmful external excitation, generate functional patterns, and in-line monitor the bending and torsion reliability of the R2R products. Third, we present in-line monitor methods for measuring nonuniform web tension for control of the uniformity of product performance crossing the width of the web.

In Chapter 2, we theoretically develop and experimentally validate an accurate thermomechanics model of flexible, axially moving webs subjecting to arbitrary heat flux for the control of process stability and product quality in R2R flexible devices manufacturing. A mathematical model for predicting the temperature and stress distribution in an axially moving web under arbitrary shape of heat flux is presented, including axial transport, heat conduction, convective heat transfer, and thermal radiation. A MATLAB based nonlinear finite element code is developed to predict the temperature and stress fields during such processes. The experimentally measured temperature distribution in moving paper and PET webs subject to heating from an IR laser source is compared with theoretical predictions to validate the computational approach. Such computational models are expected to aid in the development of a range of R2R processes where temperature gradients and stress fields can influence the product quality or lead to mechanical instabilities such as wrinkling or excessive web vibration.

In Chapter 3, we investigate the air-coupled web vibrations and develop closed-form, semi-analytical, universal hydrodynamic functions used to accurately predict the lowest symmetric and anti-symmetric transverse frequency response for any uniaxially and uniformly tensioned web of arbitrary material and aspect ratio used in roll-to-roll processes. The surrounding air acts as distributed added mass and significantly affects the frequency responses of tensioned thin webs in ambient R2R processes in comparison to those *in vacuo*. We experimentally validate those functions using pointwise laser measurements of acoustically excited webs with different pre-tensions, web materials, and aspect ratios. These closed-form hydrodynamic functions provide R2R process designers a convenient way to predict the lowest frequencies of such web systems without the need to resort to computationally intensive methods; alternately these functions allow for the quick identification of conditions when air-coupling is important to determine the web's

vibration response. The results presented herein are expected to help ongoing efforts to improve process monitoring and control in a variety of R2R continuous manufacturing technologies.

In Chapter 4, we develop and test a non-contact resonance method and a gentle contact stiffness mapping method for measuring the average web tension and its linear variation. We inversely apply the closed-form equations in Chapter 3 and improve the method with a nonuniform tension. This method uses the lowest symmetric and anti-symmetric frequencies of a web with a closed-form expression to obtain its linearly varied tension. The closed-form expression includes the significant effects of air loading on web vibrations through accurate hydrodynamic functions. While the gentle contact stiffness mapping method is based on nonlinear regression of the contact stiffness on multiple locations of the web. Both methods are accurate, reliable, and inexpensive, and are compatible for a wide range of web properties, web path, web tension, measurement configurations, and environmental conditions. We cross-validate the two methods on a stationary test stand and in-line test the non-contact resonance method in two spans of a moving commercial R2R system. We expect the results presented in this chapter can improve quality control of R2R processes for flexible and printed electronics and maximize device yields.

We summarize the conclusions in Chapter 5 and give an outlook on future directions for multi-physics research in R2R processes for flexible devices.

1.4 References

[1] Webb, R. C., Bonifas, A. P., Behnaz, A., Zhang, Y., Yu, K. J., Cheng, H., ... & Rogers, J. A. (2013). Ultrathin conformal devices for precise and continuous thermal characterization of human skin. *Nature materials*, *12*(10), 938-944.

[2] Yeo, J., Kim, G., Hong, S., Kim, M. S., Kim, D., Lee, J., ... & Ko, S. H. (2014). Flexible supercapacitor fabrication by room temperature rapid laser processing of roll-to-roll printed metal nanoparticle ink for wearable electronics application. *Journal of Power Sources*, *246*, 562-568.

[3] Bariya, M., Shahpar, Z., Park, H., Sun, J., Jung, Y., Gao, W., ... & Javey, A. (2018). Roll-to-roll gravure printed electrochemical sensors for wearable and medical devices. *ACS nano*, *12*(7), 6978-6987.

[4] Krebs, F. C. (2009). All solution roll-to-roll processed polymer solar cells free from indium-tin-oxide and vacuum coating steps. *Organic Electronics*, *10*(5), 761-768.

[5] Park, Y. S., Choi, K. H., & Kim, H. K. (2009). Room temperature flexible and transparent ITO/Ag/ITO electrode grown on flexile PES substrate by continuous roll-to-roll sputtering for flexible organic photovoltaics. *Journal of Physics D: Applied Physics*, *42*(23), 235109.

[6] Krebs, F. C., Tromholt, T., & Jørgensen, M. (2010). Upscaling of polymer solar cell fabrication using full roll-to-roll processing. *Nanoscale*, *2*(6), 873-886.

[7] Park, Y. S., & Kim, H. K. (2010). Flexible indium zinc oxide/Ag/indium zinc oxide multilayer electrode grown on polyethersulfone substrate by cost-efficient roll-to-roll sputtering for flexible organic photovoltaics. *Journal of Vacuum Science & Technology A: Vacuum, Surfaces, and Films*, *28*(1), 41-47.

[8] Perelaer, J., Abbel, R., Wünscher, S., Jani, R., Van Lammeren, T., & Schubert, U. S. (2012). Roll-to-roll compatible sintering of inkjet printed features by photonic and microwave exposure: from non-conductive ink to 40% bulk silver conductivity in less than 15 seconds. *Advanced materials*, *24*(19), 2620-2625.

[9] Søndergaard, R., Hösel, M., Angmo, D., Larsen-Olsen, T. T., & Krebs, F. C. (2012). Roll-to-roll fabrication of polymer solar cells. *Materials today*, *15*(1-2), 36-49.\

[10] Griffith, M. J., Cooling, N. A., Vaughan, B., Elkington, D. C., Hart, A. S., Lyons, A. G., ... & Dastoor, P. C. (2015). Combining printing, coating, and vacuum deposition on the roll-to-roll scale: a hybrid organic photovoltaics fabrication. *IEEE Journal of Selected Topics in Quantum Electronics*, *22*(1), 112-125.

[11] Hwang, K., Jung, Y. S., Heo, Y. J., Scholes, F. H., Watkins, S. E., Subbiah, J., ... & Vak, D. (2015). Toward large scale roll-to-roll production of fully printed perovskite solar cells. *Advanced materials*, *27*(7), 1241-1247.

[12] Finn III, M., Martens, C. J., Zaretski, A. V., Roth, B., Søndergaard, R. R., Krebs, F. C., & Lipomi, D. J. (2018). Mechanical stability of roll-to-roll printed solar cells under cyclic bending and torsion. *Solar Energy Materials and Solar Cells*, *174*, 7-15.

[13] Noh, J., Jung, M., Jung, K., Lee, G., Lim, S., Kim, D., ... & Cho, G. (2011). Integrable single walled carbon nanotube (SWNT) network based thin film transistors using roll-to-roll gravure and inkjet. *Organic Electronics*, *12*(12), 2185-2191.

[14] Hassinen, T., Ruotsalainen, T., Laakso, P., Penttilä, R., & Sandberg, H. G. (2014). Roll-to-roll compatible organic thin film transistor manufacturing technique by printing, lamination, and laser ablation. *Thin Solid Films*, *571*, 212-217.

[15] Kim, J., Hassinen, T., Lee, W. H., & Ko, S. (2017). Fully solution-processed organic thin-film transistors by consecutive roll-to-roll gravure printing. *Organic Electronics*, *42*, 361-366.

[16] Grubb, P. M., Mokhtari Koushyar, F., Lenz, T., Asghari, A., Gan, G., Xia, W., ... & Chen, R. T. (2019). High speed roll-to-roll printable transistor enabled by a pulsed light curable CNT ink. *Journal of Manufacturing and Materials Processing*, *3*(2), 33.

[17] Arcila-Velez, M. R., Zhu, J., Childress, A., Karakaya, M., Podila, R., Rao, A. M., & Roberts, M. E. (2014). Roll-to-roll synthesis of vertically aligned carbon nanotube electrodes for electrical double layer capacitors. *Nano Energy*, *8*, 9-16.

[18] Kang, S., Lim, K., Park, H., Park, J. B., Park, S. C., Cho, S. P., Kang, K., & Hong, B. H. (2018). Roll-to-Roll Laser-Printed Graphene–Graphitic Carbon Electrodes for High-Performance Supercapacitors. *ACS applied materials & interfaces*, *10*(1), 1033-1038.

[19] Li, H., Guo, H., Tong, S., Huang, K., Zhang, C., Wang, X., ... & Yang, J. (2019). High-performance supercapacitor carbon electrode fabricated by large-scale roll-to-roll micro-gravure printing. *Journal of Physics D: Applied Physics*, *52*(11), 115501.

[20] Sandström, A., Dam, H. F., Krebs, F. C., & Edman, L. (2012). Ambient fabrication of flexible and large-area organic light-emitting devices using slot-die coating. *Nature communications*, *3*(1), 1-5.

[21] Furukawa, T., & Koden, M. (2017). Novel Roll-to-Roll Deposition and Patterning of ITO on Ultra-Thin Glass for Flexible OLEDs. *IEICE Transactions on Electronics*, *100*(11), 949-954.

[22] Jung, E., Kim, C., Kim, M., Chae, H., Cho, J. H., & Cho, S. M. (2017). Roll-to-roll preparation of silver-nanowire transparent electrode and its application to large-area organic light-emitting diodes. *Organic Electronics*, *41*, 190-197.

[23] Sim, H., Kim, C., Bok, S., Kim, M. K., Oh, H., Lim, G. H., ... & Lim, B. (2018). Five-minute synthesis of silver nanowires and their roll-to-roll processing for large-area organic light emitting diodes. *Nanoscale*, *10*(25), 12087-12092.

[24] Kuswandi, B., Wicaksono, Y., Abdullah, A., Heng, L. Y., & Ahmad, M. (2011). Smart packaging: sensors for monitoring of food quality and safety. *Sensing and Instrumentation for Food Quality and Safety*, *5*(3), 137-146.

[25] Jung, M., Kim, J., Noh, J., Lim, N., Lim, C., Lee, G., ... & Cho, G. (2010). All-printed and roll-to-roll-printable 13.56-MHz-operated 1-bit RF tag on plastic foils. *IEEE Transactions on Electron Devices*, *57*(3), 571-580.

[26] Zichner, R., & Baumann, R. R. (2013). Roll-to-roll screen printed radio frequency identification transponder antennas for vehicle tracking systems. *Japanese Journal of Applied Physics*, *52*(5S1), 05DC24.

[27] Wi, J. S., Lee, S., Lee, S. H., Oh, D. K., Lee, K. T., Park, I., ... & Ok, J. G. (2017). Facile three-dimensional nanoarchitecturing of double-bent gold strips on roll-to-roll nanoimprinted transparent nanogratings for flexible and scalable plasmonic sensors. *Nanoscale*, *9*(4), 1398-1402.

[28] Park, J., Nam, D., Park, S., & Lee, D. (2018). Fabrication of flexible strain sensors via roll-to-roll gravure printing of silver ink. *Smart Materials and Structures*, *27*(8), 085014.

[29] Jeong, H., Noh, Y., & Lee, D. (2019). Highly stable and sensitive resistive flexible humidity sensors by means of roll-to-roll printed electrodes and flower-like TiO2 nanostructures. *Ceramics International*, *45*(1), 985-992.

[30] Lee, S. H., & Lee, S. (2019). Fabrication and Characterization of Roll-to-Roll Printed Air-Gap Touch Sensors. *Polymers*, *11*(2), 245.

[31] Lee, S. H., & Lee, S. (2020). Cantilever Type Acceleration Sensors Made by Roll-to-Roll Slot-Die Coating. *Sensors*, *20*(13), 3748.

[32] Lee, S. H., & Lee, S. (2020). Fabrication and Characterization of Roll-to-Roll-Coated Cantilever-Structured Touch Sensors. *ACS Applied Materials & Interfaces*, *12*(41), 46797-46803.

[33] Liedert, C., Rannaste, L., Kokkonen, A., Huttunen, O. H., Liedert, R., Hiltunen, J., & Hakalahti, L. (2020). Roll-to-roll manufacturing of integrated immunodetection sensors. *ACS sensors*, *5*(7), 2010-2017.

[34] Gagliardi, Margareth. (2019, May). *Global Markets for Roll-to-roll Technologies for Flexible Devices*. BCC Research database: SMC082C.

[35] Bae, S., Kim, H., Lee, Y., Xu, X., Park, J. S., Zheng, Y., ... & Iijima, S. (2010). Roll-to-roll production of 30-inch graphene films for transparent electrodes. *Nature nanotechnology*, *5*(8), 574.

[36] Kobayashi, T., Bando, M., Kimura, N., Shimizu, K., Kadono, K., Umezu, N., ... & Hobara, D. (2013). Production of a 100-m-long high-quality graphene transparent conductive film by roll-to-roll chemical vapor deposition and transfer process. *Applied Physics Letters*, *102*(2), 023112.

[37] Ridgway, P. L., Russo, R. E., Lafond, E. F., Habeger, C. C., & Jackson, T. (2003). Laser ultrasonic system for online measurement of elastic properties of paper. *Journal of pulp and paper science*, *29*(9).

[38] Vedrines, M., Gassmann, V., & Knittel, D. (2008). Moving web-tension determination by out-of-plane vibration measurements using a laser. *IEEE Transactions on Instrumentation and Measurement*, *58*(1), 207-213.

[39] Ma, L., Chen, J., Tang, W., & Yin, Z. (2017). Transverse vibration and instability of axially travelling web subjected to non-homogeneous tension. *International Journal of Mechanical Sciences*, *133*, 752-758.

[40] Ma, L., Chen, J., Tang, W., & Yin, Z. (2017). Vibration-based estimation of tension for an axially travelling web in roll-to-roll manufacturing. *Measurement Science and Technology*, *29*(1), 015102.

[41] Huang, Y., Chen, J., Yin, Z., & Xiong, Y. (2011). Roll-to-roll processing of flexible heterogeneous electronics with low interfacial residual stress. *IEEE Transactions on Components, Packaging and Manufacturing Technology*, *1*(9), 1368-1377.

[42] Feng, D., & Raman, A. (2019). Thermomechanics of axially moving webs in roll-to-roll manufacturing processes. *International Journal of Heat and Mass Transfer*, *129*, 1317-1327.

[43] Abouelregal, A. E., & Zenkour, A. M. (2015). Thermoelastic problem of an axially moving microbeam subjected to an external transverse excitation. *Journal of Theoretical and Applied Mechanics*, *53*(1), 167-178.

[44] Guo, X., Wang, Z., Wang, Y., & Zhou, Y. (2009). Analysis of the coupled thermoelastic vibration for axially moving beam. *Journal of Sound and Vibration*, *325*(3), 597-608.

[45] Guo, X., & Wang, Z. (2010). Thermoelastic coupling vibration characteristics of the axially moving beam with frictional contact. *Journal of vibration and acoustics*, *132*(5).

[46] Guo, X., Wang, Z., & Wang, Y. (2011). Dynamic stability of thermoelastic coupling moving plate subjected to follower force. *Applied acoustics*, *72*(2-3), 100-107.

[47] Kazemirad, S., Ghayesh, M. H., & Amabili, M. (2013). Thermo-mechanical nonlinear dynamics of a buckled axially moving beam. *Archive of Applied Mechanics*, *83*(1), 25-42.

[48] Kazemirad, S., Ghayesh, M. H., & Amabili, M. (2013). Thermal effects on nonlinear vibrations of an axially moving beam with an intermediate spring-mass support. *Shock and Vibration*, *20*(3), 385-399.

[49] Kwon, K., & Lee, U. (2006). Spectral element modeling and analysis of an axially moving thermoelastic beam-plate. *Journal of Mechanics of Materials and Structures*, *1*(4), 605-632.

[50] Zenkour, A. M., Abouelregal, A. E., & Abbas, I. A. (2014). Generalized thermoelastic vibration of an axially moving clamped microbeam subjected to ramp-type thermal loading. *Journal of Thermal Stresses*, *37*(11), 1302-1323.

[51] Seo, I. S., Song, J. H., Shin, J. M., & Kim, J. S. (2009, August). A tension control for web transportation in continuous annealing processes. In *2009 7th Asian Control Conference* (pp. 1420-1425). IEEE.

[52] Lee, C., Kang, H., & Shin, K. (2010). A study on tension behavior considering thermal effects in roll-to-roll E-printing. *Journal of mechanical science and technology*, *24*(5), 1097-1103.

[53] Frechard, J., & Knittel, D. (2012, July). Advanced optimization of industrial large-scale roll-to-roll systems under parametric uncertainties. In *Engineering Systems Design and Analysis* (Vol. 44847, pp. 263-270). American Society of Mechanical Engineers.

[54] Lu, Y., & Pagilla, P. R. (2013, October). Modeling the effects of heat transfer processes on material strain and tension in roll to roll manufacturing. In *Dynamic Systems and Control Conference* (Vol. 56147, p. V003T48A004). American Society of Mechanical Engineers.

[55] Lu, Y., & Pagilla, P. R. (2014, June). Adaptive control of web tension in a heat transfer section of a roll-to-roll manufacturing process line. In *2014 American Control Conference* (pp. 1799-1804). IEEE.

[56] Lu, Y., & Pagilla, P. R. (2015, October). A Nonlinear Tension Control Scheme for Web Transport Through Heating Processes. In *Dynamic Systems and Control Conference* (Vol. 57250, p. V002T32A006). American Society of Mechanical Engineers.

[57] Lu, Y., & Pagilla, P. R. (2012, October). Modeling of temperature distribution in a moving web transported over a heat transfer roller. In *Dynamic Systems and Control Conference* (Vol. 45301, pp. 405-414). American Society of Mechanical Engineers.

[58] Lu, Y., & Pagilla, P. R. (2014). Modeling of temperature distribution in moving webs in roll-to-roll manufacturing. *Journal of Thermal Science and Engineering Applications*, *6*(4).

[59] Brockmann, R., Dickmann, K., Geshev, P., & Matthes, K. J. (2003). Calculation of temperature field in a thin moving sheet heated with laser beam. *International journal of heat and mass transfer*, *46*(4), 717-723.

[60] Brockmann, R., Dickmann, K., Geshev, P., & Matthes, K. J. (2003). Calculation of laser-induced temperature field on moving thin metal foils in consideration of Stefan problem. *Optics & Laser Technology*, *35*(2), 115-122.

[61] Nguyen, Q. C., & Hong, K. S. (2011). Transverse vibration control of axially moving membranes by regulation of axial velocity. *IEEE Transactions on Control Systems Technology*, *20*(4), 1124-1131.

[62] Kimbrough, B. (2015, September). In-line roll-to-roll metrology for flexible electronics. In *Applied Advanced Optical Metrology Solutions* (Vol. 9576, p. 957603). International Society for Optics and Photonics.

[63] Eum, S., Lee, J., & Nam, K. (2016, October). Robust tension control of roll to roll winding equipment based on a disturbance observer. In *IECON 2016-42nd Annual Conference of the IEEE Industrial Electronics Society* (pp. 625-630). IEEE.

[64] Palavesam, N., Marin, S., Hemmetzberger, D., Landesberger, C., Bock, K., & Kutter, C. (2018). Roll-to-roll processing of film substrates for hybrid integrated flexible electronics. *Flexible and Printed Electronics*, *3*(1), 014002.

[65] Niemi, J., & Pramila, A. (1987). FEM-analysis of transverse vibrations of an axially moving membrane immersed in ideal fluid. *International journal for numerical methods in engineering*, *24*(12), 2301-2313.

[66] Koivurova, H., & Pramila, A. (1997). Nonlinear vibration of axially moving membrane by finite element method. *Computational Mechanics*, *20*(6), 573-581.

[67] Raman, A., Wolf, K. D., & Hagedorn, P. (2000, June). Observations on the vibrations of paper webs. *11th Annual Symposium on Information Storage and Processing Systems*.

[68] Chang, Y. B., & Moretti, P. M. (2002). Flow-induced vibration of free edges of thin films. *Journal of fluids and structures*, *16*(7), 989-1008.

[69] Vaughan, M., & Raman, A. (2010). Aeroelastic stability of axially moving webs coupled to incompressible flows. *Journal of Applied Mechanics*, *77*(2).

[70] Hara, K., & Watanabe, M. (2013). Stability analysis of rectangular plates in incompressible flow with Fourier multiplier operators. In *ASME 2013 Pressure Vessels and Piping Conference*. American Society of Mechanical Engineers Digital Collection.

[71] Hara, K., & Watanabe, M. (2014, July). Formulation of the Aeroelastic Instability Problem of Rectangular Plates in Uniform Flow Based on the Hamiltonian Mechanics for the Constrained System. In *Pressure Vessels and Piping Conference* (Vol. 46018, p. V004T04A060). American Society of Mechanical Engineers.

[72] Yao, G., & Zhang, Y. M. (2016). Dynamics and stability of an axially moving plate interacting with surrounding airflow. *Meccanica*, *51*(9), 2111-2119.

[73] Koç, H., Knittel, D., De Mathelin, M., & Abba, G. (2002). Modeling and robust control of winding systems for elastic webs. *IEEE Transactions on control systems technology*, *10*(2), 197-208.

[74] Jeong, J., Gafurov, A. N., Park, P., Kim, I., Kim, H., Kang, D., ... & Lee, T. M. (2021). Tension Modeling and Precise Tension Control of Roll-to-Roll System for Flexible Electronics. *Flexible and Printed Electronics*, *6*, 015005

[75] Schultheis, F. (2007). *U.S. Patent Application No. 11/175,628*.

[76] Linna, H., Parola, M., & Virtanen, J. (2001). Better productivity by measuring web tension profile. In *55th Appita Annual Conference, Hobart, Australia 30 April-2 May 2001: Proceedings* (p. 305). Appita Inc.

[77] Eriksson, L. (1978). *U.S. Patent No. 4,109,520*. Washington, DC: U.S. Patent and Trademark Office.

[78] Strom, V. E., Johansson, B. L. I., & Karlsson, H. I. (1987). *U.S. Patent No. 4,655,093*. Washington, DC: U.S. Patent and Trademark Office.

[79] Yan, J., & Du, X. (2020). Real-time web tension prediction using web moving speed and natural vibration frequency. *Measurement Science and Technology*, *31*(11), 115205.

[80] Jin, Y., Chen, J., & Yin, Z. (2020). Web Tension Estimation by Local Contact Force Measurement in Roll-to-Roll Manufacturing. *International Journal of Precision Engineering and Manufacturing*, *21*(11), 2067-2075.

2. THERMOMECHANICS OF AXIALLY MOVING WEBS IN ROLL-TO-ROLL MANUFACTURING PROCESSES

This Chapter was published in International Journal of Heat and Mass Transfer (DOI: 10.1016/j.ijheatmasstransfer.2018.10.038). We acknowledge the author rights provided by Elsevier to include it in this dissertation.

2.1 Introduction

Roll-to-roll (R2R) systems for nano-manufacturing /flexible electronics involve a flexible, axially moving web subject to non-uniform heat fluxes. These incident heat fluxes are often intrinsic features of processes such as sputtering, deposition, coating, drying, chemical growth, imprint lithography, hot embossing, heat annealing, and laser ablation [1-9], as shown in Figure 2.1(a).

The thermomechanical response of moving webs in R2R systems for nano-manufacturing and flexible electronics is closely coupled to the product quality and process stability. For example, the local web temperature encountered in the process strongly affects the resulting physical properties of the grown /deposited /cured layers and the web temperature field can lead to thermal stresses, wrinkling and excessive vibration. On the other hand, process variables such as web speed and tension strongly influence the temperature distribution as do the physical properties of the web. Thus, the web thermomechanics, process variables and stability, and quality of the deposited/grown layers are closely interconnected.

Accurate simulation tools for predicting web thermomechanics are currently not available for this broad category of nanomanufacturing /flexible electronics processes. Previous work on thermal problems of axially moving media has mostly focused on thermoelastic vibration, tension control, or pure heat transfer. The vibration of an axially moving beam subject to a spatially fixed temperature profile was studied by including thermal load in the form of a bending moment [10-17]. The decentralized feedback control of tension in a multi-span R2R system with time-varying temperature was developed using simple axial deformation elements in each span, including tension-dependent strain and temperature-dependent strain [18-23]. Additionally, Lu and Pagilla presented some results of modeling the axial temperature distribution in a moving web assuming uniform temperature along the lateral direction (along web width) [24,25]. Kurki *et al*. studied the

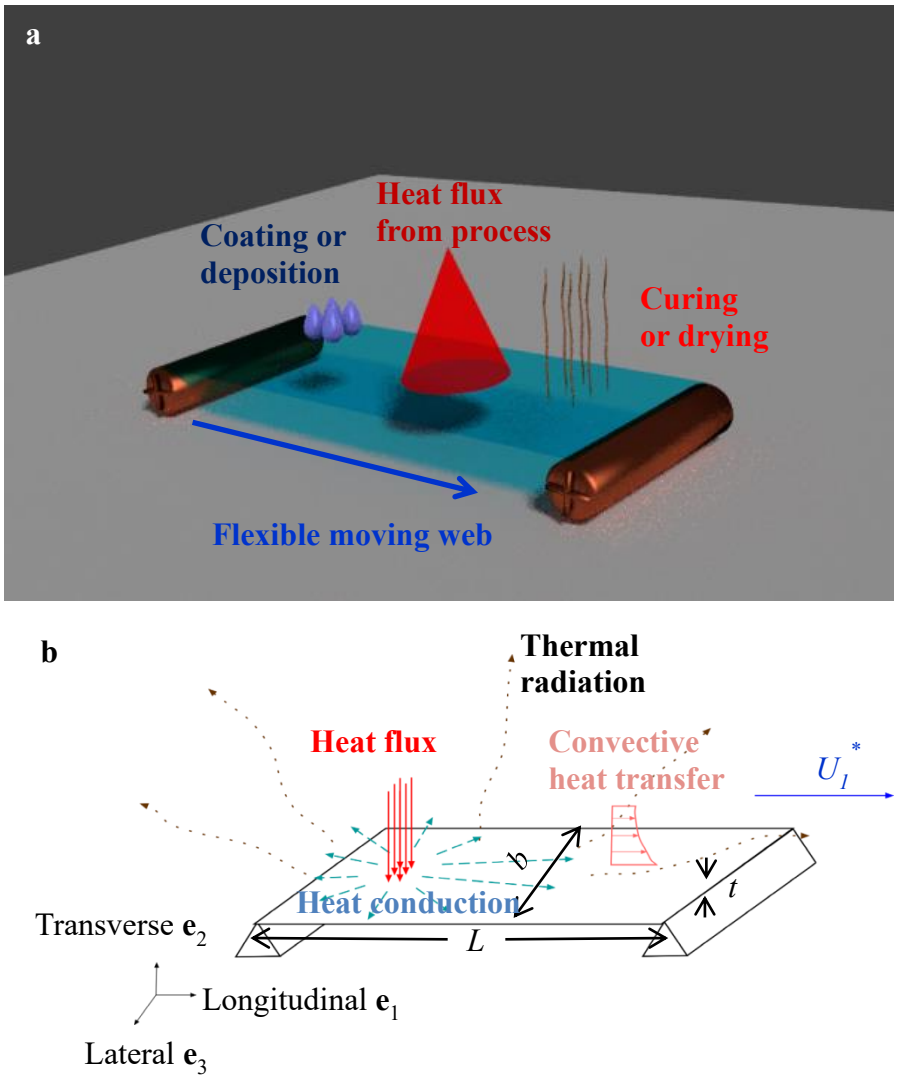

Figure 2.1. (a) Axially moving web under locally heat flux respecting to various R2R processes (e.g. coating, deposition, heating, curing or evaporation). (b) A sketch of the mathematical model for thermomechanics of an axially moving web subject to heat flux, including heat conduction, convective heat transfer and thermal radiation. $\mathbf{e}_1$, $\mathbf{e}_2$, and $\mathbf{e}_3$ are longitudinal, transverse, and lateral directions, respectively. U_1^* is the transport speed in the $\mathbf{e}_1$ direction, L is the length of web in longitudinal direction, b is the width of web in lateral direction, t is the thickness of web in the $\mathbf{e}_2$ direction.

in-plane stresses of an axially moving web with in-plane flow control, without considering thermal effects [26]. Other works model the temperature field in the longitudinal-lateral plane under a given heat flux without thermomechanics coupling. Brockmann *et al*. aimed at understanding the temperature behavior in the longitudinal-lateral plane of a moving web at large distance from heating point in laser hardening, cutting or welding. They took into account the effects of both

convective heat transfer and thermal radiation via a constant heat transfer coefficient and as linear term of temperature [27, 28]. Baïri neglected the contribution of both thermal radiation and convection, since they modeled the heat transfer in a very thick moving body with a coated film on it [29]. Both Brockmann and Baïri use Fourier transformation to solve for the temperature fields on the moving webs.

In R2R processes for nanomanufacturing /flexible electronics with thin film webs, the in-plane temperature and stress field gradients are much greater than those in the through-thickness direction. Hence, an accurate thermomechanics model of the axially moving web is needed to illuminate the contribution of each physical term to the temperature and stress fields and to help to better control the product quality. Only a handful of prior works are relevant to this broad category of problems where the in-plane thermomechanics are important. Amongst those works (such as [27,28]), none consider the effects of thermal radiation which is of relevance to those processes where higher temperatures are involved. Equally importantly, we are not aware of any experimental validation of 2D thermomechanics models on moving media with applied heating sources.

In order to understand the thermomechanics mechanisms in R2R manufacturing, we present a mathematical model of an axially moving web subject to arbitrary heat flux. The model includes linear heat conduction, nonlinear convective heat transfer, thermal radiation, and thermomechanical coupling. With the purpose of validating the model, we set up an experiment with moving paper and PET webs subject to local heating from a CO_2 laser. The temperature field in the Eulerian reference frame is mapped using an IR camera to measure the at various web transport speeds. The model can be used to predict the temperature and stress distributions of the web during R2R processes, and to prevent over/less heating and/or web wrinkling.

2.2 Mathematical Model

We focus on the thermomechanics of a thin flexible web subject to non-uniform, arbitrary heat flux distribution, as shown in Figure 2.1(b). $\mathbf{e}_1$, $\mathbf{e}_2$, and $\mathbf{e}_3$ are longitudinal, transverse, and lateral directions, respectively. U_1^* is the steady transport speed (*i.e.* web speed) in the $\mathbf{e}_1$ direction, L is the length of web in longitudinal direction, b is the width of web in lateral direction, t is the thickness of web in transverse direction. A steady axially transported thin web is used in the model

since the web is continuously fed in most R2R processes. An Eulerian description (as opposed to Lagrangian) is used for the temperature, stress, and deformation fields. Stress and temperature gradients in the transverse direction are negligible for thin webs. Nonlinear terms in the model include temperature and deformation coupling, nonlinear convective heat transfer, and thermal radiation.

2.2.1 Derivation of Governing Equations

We first begin from the governing equations for a stationary web using a Lagrangian description where the field symbols are written with hats. The internal convection terms will be added via coordinate transformation to an Eulerian description. Cauchy's infinitesimal strain tensor gives strain-displacement relations as

$$\hat{\varepsilon}_{ij} = \frac{1}{2}(\hat{u}_{i,j} + \hat{u}_{j,i}), \tag{2.1}$$

where $\hat{\varepsilon}_{ij}$ are the components of infinitesimal strain tensor, $\hat{u}_i$ is the displacement in $\mathbf{e}_i$ direction after applying pre-tension. From the linear elastic constitutive equations with thermal expansion, the stress-to-strain relations (*i.e.* Duhamel-Neumann relations) yield [30, 31]

$$\hat{\sigma}_{ij} = c_{ijkl}\hat{\varepsilon}_{kl} - \beta_{ij}(\hat{T} - T_0), \tag{2.2}$$

where $\hat{\sigma}_{ij}$ are the components of the stress tensor in the chosen reference frame, c_{ijkl} are the components in the tensor of elastic stiffness, β_{ij} are the stress-to-temperature coupling parameters ($\beta_{11} = \beta_{22} = \beta_{33} = \frac{E\alpha_T}{1-2\upsilon}$, $\beta_{23} = \beta_{13} = \beta_{12} = 0$. With E, α_T , υ denoting, respectively, Young's modulus, coefficient of thermal expansion, and Poisson's ratio), $\hat{T}$ is the absolute web temperature, and T_0 is the reference, stress-free absolute temperature. $c_{ijkl}\hat{\varepsilon}_{kl} = c_{ij11}\hat{\varepsilon}_{11} + c_{ij12}\hat{\varepsilon}_{12} + \cdots + c_{ij33}\hat{\varepsilon}_{33}$ follows the indicial summation convention. The balance of linear momentum yields

$$\hat{\sigma}_{ji,j} + \hat{X}_i = \rho\ddot{\hat{u}}_i, \tag{2.3}$$

where $\hat{X}_i$ is the body force, ρ is mass density. The extended equation of thermal conductivity is derived from the expression for Helmholtz free energy [32], the determination of heat capacity,

and Fourier's law of heat conduction [33]. The details of derivation are shown in [34, 35]. The extended equation of thermal conductivity is

$$\hat{T}\beta_{ij}\dot{\hat{\varepsilon}}_{ij} + \rho c\dot{\hat{T}} = \lambda_{ij}\hat{T}_{,ij} + s, \tag{2.4}$$

where c is the specific heat capacity, s is the heat source acting in the body, λ_{ij} is the thermal conductivity.

Moving on to the case for an axially moving web with a transport speed U_1^*, the governing equations are transformed to an Eulerian description (unhatted quantities). In the Eulerian description, Eqs. (2.1) and (2.2) remain unchanged while Eqs. (2.3) and (2.4) can be rewritten as

$$\sigma_{ji,j} + X_i = \rho(\ddot{u}_i + \dot{U}_1^* u_{i,1} + 2U_1^* \dot{u}_{i,1} + U_1^{*2} u_{i,11}), \tag{2.5}$$

$$\lambda_{ij}T_{,ij} - \rho c(\dot{T} + U_1^* T_{,1}) - T\beta_{ij}(\dot{\varepsilon}_{ij} + U_1^* \varepsilon_{ij,1}) = -s. \tag{2.6}$$

Next, we assume:

1. the material is homogeneous and isotropic, and linear thermoelastic constitutive relations apply (c_{ijkl} can be described by E and υ, $\lambda_{ij} = k$),
2. the mechanical and thermal properties of the solid web are independent of temperature change and strain,
3. the temperature and stress fields can be modeled as two-dimensional (i = 1, 3), for these for thin webs ($\sigma_{22} = \sigma_{23} = \sigma_{12} = 0$, $\varepsilon_{23} = \varepsilon_{12} = 0$, $\beta_{11} = \beta_{33} = \dfrac{E\alpha_T}{1-\upsilon}$, all other β_{ij}'s $= 0$),
4. there are no body forces ($X_i = 0$),
5. the web thermomechanics are at steady state, *i.e.* all time derivatives are evaluated to zero.

Rewriting the governing equations under the above assumptions, the strain-displacement relations become

$$\varepsilon_{11} = u_{1,1}, \quad \varepsilon_{22} = u_{2,2}, \quad \varepsilon_{33} = u_{3,3}, \quad \varepsilon_{13} = \frac{1}{2}(u_{1,3} + u_{3,1}); \tag{2.7}$$

the constitutive equations with thermal expansion become

$$\sigma_{11} = \frac{E}{1-\upsilon^2}\varepsilon_{11} + \frac{\upsilon E}{1-\upsilon^2}\varepsilon_{33} - \frac{E}{1-\upsilon}\alpha_T(T - T_0), \tag{2.8}$$

$$\sigma_{33} = \frac{E}{1-\upsilon^2}\varepsilon_{33} + \frac{\upsilon E}{1-\upsilon^2}\varepsilon_{11} - \frac{E}{1-\upsilon}\alpha_T(T - T_0), \tag{2.9}$$

$$\sigma_{13} = \frac{E}{1+\upsilon}\varepsilon_{13}, \tag{2.10}$$

where ε_{13} is the true shear strain and equals to half of engineering shear strain γ_{13}; the balances of linear momentum become

$$\sigma_{11,1} + \sigma_{31,3} = \rho U_1^{*2} u_{1,11}, \tag{2.11}$$

$$\sigma_{13,1} + \sigma_{33,3} = \rho U_1^{*2} u_{3,11}; \tag{2.12}$$

and the extended equation of thermal conductivity is

$$k(T_{,11} + T_{,33}) - \rho c U_1^* T_{,1} - T\frac{E\alpha_T}{1-\upsilon} U_1^* (\varepsilon_{11,1} + \varepsilon_{33,1}) = -s. \tag{2.13}$$

Substituting Eqs. (2.7) - (2.10) into Eqs. (2.11) and (2.12) yields

$$(\frac{E}{1-\upsilon^2} - \rho U_1^{*2}) u_{1,11} + \frac{E}{2(1+\upsilon)} u_{1,33} + \frac{E}{2(1-\upsilon)} u_{3,13} = \frac{E}{1-\upsilon}\alpha_T (T - T_0)_{,1}, \tag{2.14}$$

$$[\frac{E}{2(1+\upsilon)} - \rho U_1^{*2}] u_{3,11} + \frac{E}{2(1-\upsilon)} u_{1,13} + \frac{E}{1-\upsilon^2} u_{3,33} = \frac{E}{1-\upsilon}\alpha_T (T - T_0)_{,3}. \tag{2.15}$$

Similar equations without the web transport terms can be found in Boley and Weiner's book [36]. Substituting Eq. (2.7) into Eq. (2.13) yields

$$k(T_{,11} + T_{,33}) - \rho c U_1^* T_{,1} - T\frac{E\alpha_T}{1-\upsilon} U_1^* (u_{1,11} + u_{3,13}) = -s. \tag{2.16}$$

For thin webs, the heat source $s(x_1, x_3)$ acting in the body includes the heat transfer from convective heat transfer and thermal radiation between the surfaces of web and surroundings, and the heat flux from outer heat sources. Introducing these terms into Eq. (2.16), we get

$$k(T_{,11} + T_{,33}) - \rho c U_1^* T_{,1} - T\frac{E\alpha_T}{1-\upsilon} U_1^* (u_{1,11} + u_{3,13}) = \frac{h(T, U_1^*)}{t}(T - T_a) + \frac{2\tilde{\varepsilon}\tilde{\sigma}}{t}(T^4 - T_f^4) - \frac{q_{flux}}{t}, \tag{2.17}$$

where T_a is the absolute ambient temperature, T_f is the absolute far field temperature. q_{flux} is density of the heat flux from external heat sources, $h(T, U_1^*)$ is convection coefficient, $\tilde{\varepsilon}$ is emissivity factor of medium, $\tilde{\sigma}$ is Stefan-Boltzmann constant ($= 5.67 \times 10^{-8}$ W/(m$^2 \cdot$K^4)). The nonlinear temperature and deformation coupling term can be shown to be negligible compared with other terms (see in Appendix A). Hence, we can simplify Eq. (2.17) to the following partial differential equation for the temperature field only as

$$k(T_{,11}+T_{,33})-\rho cU_1^*T_{,1}=\frac{h(T,U_1^*)}{t}(T-T_a)+\frac{2\tilde{\varepsilon}\tilde{\sigma}}{t}(T^4-T_f^4)-\frac{q_{flux}}{t}. \quad (2.18)$$

Comparing with the method used by [27], who used a constant convection coefficient without fourth order thermal radiation term, our model includes both convective heat transfer and thermal radiation as nonlinear terms. This improves the adaptability of the model, especially to those processes with low web speed and high-density heat flux.

2.2.2 Computational Approach

An in-house MATLAB code for a finite element model (FEM) is used to solve simultaneously equations (2.14), (2.15) and (2.18) to determine the temperature and in-plane displacement fields induced by non-uniform heating sources on a moving web. We choose 8-noded serendipity elements to mesh the web and Newton-Raphson method for nonlinear iterations. We can rewrite governing equations (2.14), (2.15) and (2.18) in matrix-vector form for finite element analysis

$$\underset{m\times m}{[K_{1\_u1}]}\underset{m\times 1}{\{u_1\}}+\underset{m\times m}{[K_{1\_u3}]}\underset{m\times 1}{\{u_3\}}+\underset{m\times m}{[K_{1\_T}]}\underset{m\times 1}{\{T-T_0\}}=0, \quad (2.19)$$

$$\underset{m\times m}{[K_{2\_u1}]}\underset{m\times 1}{\{u_1\}}+\underset{m\times m}{[K_{2\_u3}]}\underset{m\times 1}{\{u_3\}}+\underset{m\times m}{[K_{2\_T}]}\underset{m\times 1}{\{T-T_0\}}=0, \quad (2.20)$$

$$\underset{m\times m}{[K_{cond\_T}]}\underset{m\times 1}{\{T\}}+\underset{m\times m}{[K_{conv\_T}]}\underset{m\times 1}{\{T\}}+\underset{m\times m}{[K_{rad\_T}]}\underset{m\times 1}{\{T^4\}}=\underset{m\times 1}{\{F\}}=\underset{m\times 1}{\{Q_{flux}\}}+\underset{m\times 1}{\{Q_{conv}\}}+\underset{m\times 1}{\{Q_{rad}\}}, \quad (2.21)$$

where the element stiffness matrices and the vectors of element forces are

$$[K_{1\_u1}^{(e)}]=\{N\}_{,1}\left(\frac{E}{1-\upsilon^2}-\rho U_1^{*2}\right)\{N\}_{,1}^T+\{N\}_{,3}\frac{E}{2(1+\upsilon)}\{N\}_{,3}^T,$$

$$[K_{1\_u3}^{(e)}]=\{N\}_{,3}\frac{E}{4(1-\upsilon)}\{N\}_{,1}^T+\{N\}_{,1}\frac{E}{4(1-\upsilon)}\{N\}_{,3}^T,$$

$$[K_{1\_T}^{(e)}]=-\{N\}_{,1}\frac{E}{1-\upsilon}\alpha_T\{N\}^T,$$

$$[K_{2\_u1}^{(e)}]=[K_{1\_u3}^{(e)}]^T,$$

$$[K_{2\_u3}^{(e)}]=\{N\}_{,1}\left[\frac{E}{2(1+\upsilon)}-\rho U_1^{*2}\right]\{N\}_{,1}^T+\{N\}_{,3}\frac{E}{1-\upsilon^2}\{N\}_{,3}^T,$$

$$[K_{2\_T}^{(e)}]=-\{N\}_{,3}\frac{E}{1-\upsilon}\alpha_T\{N\}^T,$$

$$[K_{cond\_T}^{(e)}]=\{N\}_{,1}k\{N\}_{,1}^T+\{N\}_{,3}k\{N\}_{,3}^T+\{N\}\rho cU_1^*\{N\}_{,1}^T,$$

$$[K^{(e)}_{conv\_T}]=\{N\}\frac{h(T)}{t}\{N\}^T,\quad [K^{(e)}_{rad\_T}]=\{N\}\frac{2\tilde{\varepsilon}\tilde{\sigma}}{t}\{N\}^T,$$
$$\{Q^{(e)}_{flux}\}=\{N\}\frac{q_{flux}}{t},\qquad \{Q^{(e)}_{conv}\}=\{N\}\frac{h(T)}{t}T_a,\qquad \{Q^{(e)}_{rad}\}=\{N\}\frac{2\tilde{\varepsilon}\tilde{\sigma}}{t}T_f^4. \tag{2.22}$$

We choose the following boundary conditions:

1. the temperature of the leading-edge roller equals to the ambient temperature $T(x_1=0)=T_a$,
2. there is no slip between the web and both two rollers after applying pre-tension $u_1(x_1=0,L)=u_3(x_1=0,L)=0$,
3. the lateral edges ($x_3=\pm\frac{b}{2}$) are traction free.

We consider the stress-free state after tension applied on the web but before heat loading applied. The stress-free temperature, the far field temperature, and the initial guess of temperature for Newton-Raphson method are chosen as same as ambient temperature. The iteration stops when the 2-norm of nth step residual vector in Newton-Raphson method is less or equal to 10^{-9}.

2.2.3 Fitting Convection Coefficient

Apart from vacuum R2R processes such as sputtering and chemical vapor deposition, the heat transfers of all other R2R processes involve non-ignorable convection. The model for non-vacuum processes should include both free and forced convection. To describe these convection coefficients, the characteristic length of a web is used [33]:

$$L_{ch}=\frac{area}{perimeter}=\frac{L_{effect}b}{2(L_{effect}+b)}, \tag{2.23}$$

where L_{effect} is the effective length of the web. In a hot plate, the free convection coefficients on upper and lower surfaces are different. Using the standard relations between the corresponding Nusselt and Rayleigh numbers [33], the free convection coefficients for the upper and lower surfaces are

$$h_u(T)=\frac{0.52k_a^{4/5}}{L_{ch}^{2/5}}\left(\frac{g\rho_a c_a}{\tilde{\upsilon}_a T_{bl}}\right)^{1/5}(T-T_a)^{1/5}, \tag{2.24}$$

$$h_l(T)=\frac{0.54k_a^{3/4}}{L_{ch}^{1/4}}\left(\frac{g\rho_a c_a}{\tilde{\upsilon}_a T_{bl}}\right)^{1/4}(T-T_a)^{1/4}, \tag{2.25}$$

where g is the gravitational acceleration, $k_a, \rho_a, c_a, \tilde{\upsilon}_a$ are the thermal conductivity, mass density, specific heat capacity and kinematic viscosity of ambient, respectively, of the surrounding air and T_{bl} is the absolute boundary layer temperature used to determine the properties of surrounding air:

$$T_{bl} \equiv (T + T_a)/2. \tag{2.26}$$

The forced convection coefficient on one side of the web is determined using standard relations between Nusselt, Reynolds, and Prandtl numbers [33]:

$$h_f(T, U_1^*) = \frac{0.453 k_a^{2/3} (\rho_a c_a)^{1/3}}{L_{ch}^{1/2} \tilde{\upsilon}_a^{1/6}} U_1^{*1/2}. \tag{2.27}$$

In order to determine L_{ch} we use Eq. (2.23) with L_{effect} estimated as infinity. This estimate is expected to over-predict the temperature field lightly. The characteristic length becomes

$$\lim_{L_{effect} \to \infty} L_{ch} = \frac{b}{2}. \tag{2.28}$$

Substituting Eq. (2.28) into Eqs. (2.24), (2.25), and (2.27), gives

$$h_u(T) = \frac{1.04 k_a^{4/5}}{b^{2/5}} \left(\frac{g \rho_a c_a}{8 \tilde{\upsilon}_a T_{bl}}\right)^{1/5} (T - T_a)^{1/5}, \tag{2.29}$$

$$h_l(T) = \frac{1.08 k_a^{3/4}}{b^{1/4}} \left(\frac{g \rho_a c_a}{8 \tilde{\upsilon}_a T_{bl}}\right)^{1/4} (T - T_a)^{1/4}, \tag{2.30}$$

$$h_f(T, U_1^*) = \frac{0.906 k_a^{2/3} (\rho_a c_a)^{1/3}}{(2b)^{1/2} \tilde{\upsilon}_a^{1/6}} U_1^{*1/2}. \tag{2.31}$$

Both free and forced convection need to be considered in order to adapt the model to different web speeds (see Appendix B.). Free convection is not negligible especially for low speed processes. Thus, the total convection coefficient is

$$h(T, U_1^*) = h_u(T) + h_l(T) + 2h_f(T, U_1^*). \tag{2.32}$$

Polynomial regression is used to fit the convection coefficients, since all the ambient properties depend on to the local temperature. We use the data from Bergman's book [33] for the fitting. We choose T_{bl} from 300 K to 700 K, which covers both the range of working temperatures for non-vacuum R2R processes [9 37, 38] and the range of working temperatures of the most common substrates (*e.g.* PET and PEN films [39,40]). With known g, b and T_a, the free convection coefficients are fitted up to fourth order of T, forced convection coefficient is fitted as a linear function of T multiplying $U_1^{*1/2}$. Eq. (2.32) can be rewritten as

$$h(T,U_1^*) = C_1(U_1^*) + C_2(U_1^*)T + C_3T^2 + C_4T^3 + C_5T^4. \tag{2.33}$$

In the FEM solver, the above temperature dependence is brought in by modifying Eq. (2.21) as follows

$$\begin{aligned} &[K_{\underset{m\times m}{cond\_T}}]\{T\}+[K_{\underset{m\times m}{c1}}]\{T\}+[K_{\underset{m\times m}{c2}}]\{T^2\}+[K_{\underset{m\times m}{c3}}]\{T^3\}+[K_{\underset{m\times m}{c4}}]\{T^4\}+[K_{\underset{m\times m}{c5}}]\{T^5\} \\ &+[K_{\underset{m\times m}{rad\_T}}]\{T^4\} = \{F\} = \{Q_{\underset{m\times 1}{flux}}\}+\{Q_{\underset{m\times 1}{conv}}\}+\{Q_{\underset{m\times 1}{rad}}\}, \end{aligned} \tag{2.34}$$

where

$$\begin{aligned} &[K_{c1}^{(e)}] = \{N\}\frac{C_1 - C_2T_a}{t}\{N\}^T, [K_{c2}^{(e)}] = \{N\}\frac{C_2 - C_3T_a}{t}\{N\}^T, \\ &[K_{c3}^{(e)}] = \{N\}\frac{C_3 - C_4T_a}{t}\{N\}^T, [K_{c4}^{(e)}] = \{N\}\frac{C_4 - C_5T_a}{t}\{N\}^T, \\ &[K_{c5}^{(e)}] = \{N\}\frac{C_5}{t}\{N\}^T, \end{aligned} \tag{2.35}$$

and $\{Q_{conv}^{(e)}\}$ is changed to be $\{Q_{conv}^{(e)}\} = \{N\}\frac{C_1T_a}{t}$.

Once the temperature field is computed with the fitted convection coefficients, we can compute the displacement field by substituting the temperature field into Eqs. (2.14) and (2.15). Then the stress field will be obtained from Eqs. (2.7) - (2.10). Web wrinkling can be predicted by checking if the magnitude of in-plane principal compressive stress exceeds the critical value [19, 41-45].

2.3 Computational Results

In this section, we provide computational results on temperature and stress distributions of non-uniformly heated axially moving webs in air and in vacuum. These two cases cover most processes in R2R nanomanufacturing and flexible electronics systems. The goals of the computational results are to demonstrate the key physical variables that effect web temperature and stress fields and how process variables such as web speed and incident heat flux can be adjusted to achieve stable operation and desired product quality.

We first present results for PET films that are commonly used for slot die coating, micro gravure coating, and blade coating. The web properties and simulation parameters are described in Table 2.1. The web speed is chosen from 0 m/min to 6 m/min, according to a Mirwec Custom Mini-Labo™ Deluxe R2R system we have in our laboratory (stable working speed 1 m/min - 10 m/min),

which also in the range of most R2R coating processes [2, 4, 5]. R2R printing systems will have a faster speed [19].

Table 2.1. Physical properties of the PET film.

Mass density ρ (kg/m^3) [a]	Young's Modulus E (GPa) [a]	Thermal conductivity k $(W/(m\cdot K))$ [a]	Specific heat capacity c $(kJ/(kg\cdot K))$ [a]	Coefficient of thermal expansion $\alpha_T (m/(m\cdot K))$ [a]	Web width b (cm) [a]
1.390×10^3	4.8	0.155	1.172	1.7×10^{-5}	15.24 (*i.e.* 6 *in*)
Web thickness t (μm) [a]	Emissivity factor $\tilde{\varepsilon}$ [b]	Poisson's ratio v [c]	Gravitational acceleration g (m/s^2)	Ambient temperature T_a $(^\circ C)$	
96.52 (*i.e.* 3.8 *mil*)	0.88	0.33	9.8	25 (*i.e.* 298.15 *K*)	

a *'s are provided by DuPont.*
b *is measured by a ThermaCAM® SC 300 IR camera. The IR camera is calibrated with an electrical tape with a known emissivity of 0.97.*
c *is from Wilson's paper* [57].

For this case, convective heat transfer should be included in the model. We consider a white opaque Melinex® 329 PET film from DuPont Teijin Film under a Gaussian distributed heat flux (the FEM method is suitable for heat flux with any shape) as shown in Figure 2.2(a), with maximal heat flux density 2.865 kW/m^2 and effective beam radius 2.36 cm. With this heat flux, we ensure that the peak temperature in our results 392.48 K is below the maximum working temperature, which is 470 K, as reported by DuPont for the Melinex/Mylar® PET film [39].

Figures 2.2(b)-(h) show the temperature distributions of the web under different web speeds under the fixed Gaussian shaped heat flux. As shown in Figure 2.2(b) the temperature field is symmetric along the web longitudinal direction with respect to the center of the Gaussian heat flux for a stationary web. This is expected since the material is homogeneous and isotropic, the Gaussian distributed heat flux chosen here is symmetric about the center of the heat flux, and the temperature field vanishes before reaching the web boundary.

Web axial transport has a strong influence of temperature distribution, specifically:

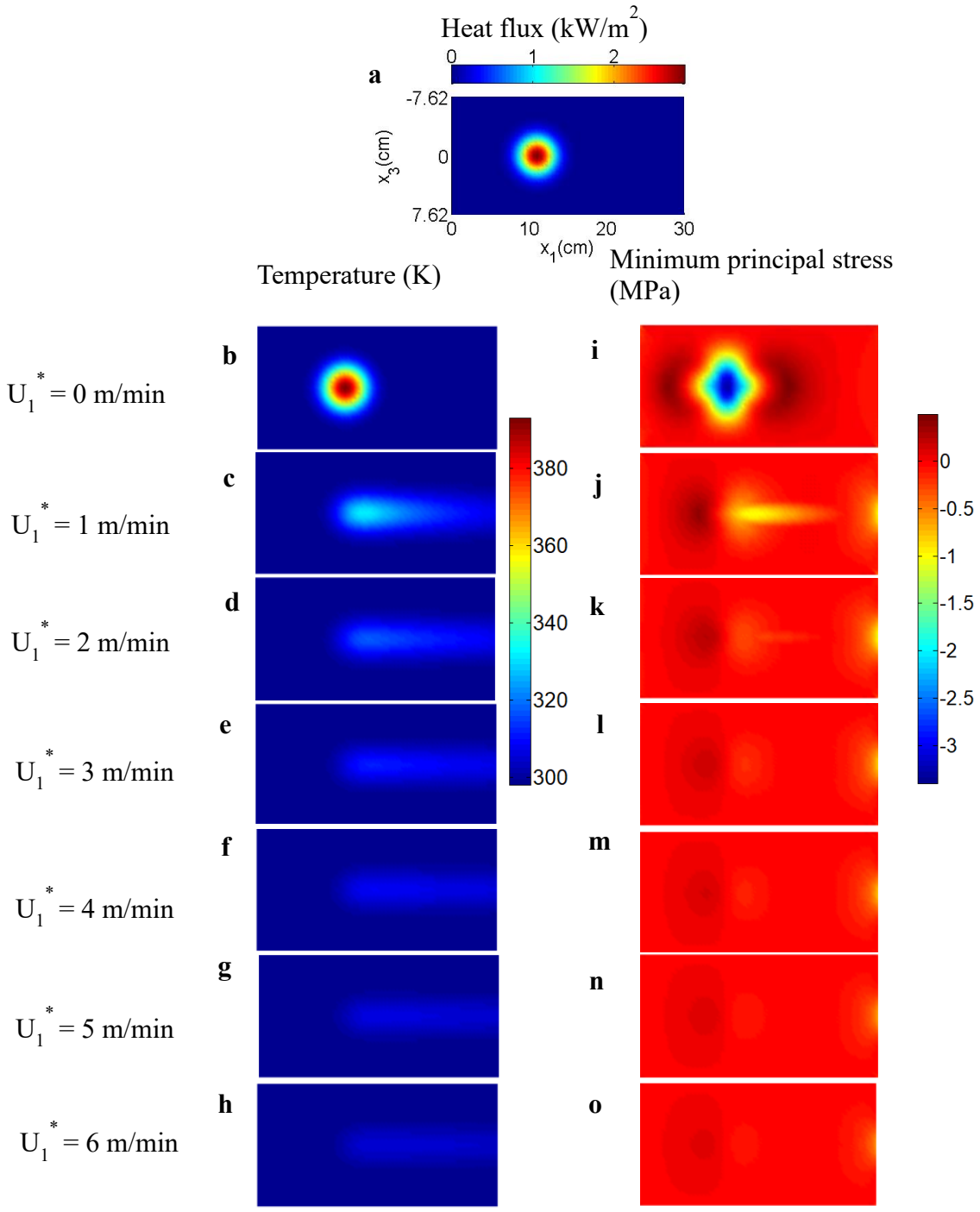

Figure 2.2. The temperature and stress distributions of a PET web in solution based R2R processes in air at different transport speeds. (a) The shape of a Gaussian distributed input heat flux with maximal heat flux density 2.865 kW/m^2, effective beam radius 2.36 cm. (b)-(h) temperature distributions under different web speeds. (i)-(o) minimum principal stress distributions under different web speeds with a pre-tension along longitudinal direction of 100 N/m, i.e. axial pre-stress of 1.036 MPa.

(a) Web axial transport of web drives the temperature field to become asymmetric with respect to the center of the incident heat flux and along transport direction, as shown in Figures 2.2 (c)-(h). The asymmetry is because of the internal convection term due to web transport, $-\rho c U_1^* T_{,1}$ in Eq. (2.18). The web transport thus drags the temperature field along the transport direction making the field asymmetric with respect to the heat flux center.

(b) The web transport not only drags the temperature field to become asymmetric with respect to the heat flux center, but also brings down the peak temperature of the temperature field. As shown in Figures 2.2 (c)-(h), the peak temperature decreases with a higher transport speed which agrees with our expectation.

(c) Additionally, the relation between peak temperature and transport speed is nonlinear, for example, doubling the transport speed does not half the peak temperature. This is a direct consequence of nonlinear terms in the equations arising from convection and radiation terms.

The distribution of minimum in-plane principal stresses is shown in Figures 2.2(i)-(o), with a pre-tension along longitudinal direction of 100 N/m, *i.e.* axial tensile pre-stress of 1.036 MPa with the minimum principal stress being 0 MPa. We choose to plot the minimum principal stresses since web regions with negative principal stresses are candidates for wrinkling to occur.

(d) Non-uniform heating significantly changes the in-plane stresses.

(e) The minimum compressive stress can become negative in the heating region of leading to the possibility of wrinkling.

(f) When the web is transported axially, similar to the temperature field, the principal stress field becomes asymmetric with respect to the heat flux center and with its peak magnitude reduces.

(g) With the same heat flux, increasing transport speed reduces the peak magnitude of compressive principal stress thus reducing the possibility of web wrinkling. However, increasing of transport speed will also increase the heat reaction region, and may cause other stability issues, such as aeroelastic flutter [46].

In comparison with in-air coating/curing based R2R systems simulated above, vacuum based R2R systems do not involve convective heat transfer. Such vacuum R2R systems include the Applied SmartWeb® sputter system from Applied Materials, Deposition Systems from Mustang

Vacuum Systems, and Tetra system from Diener Electronic Plasma Surface Technology. The general working temperature for these systems is from 1000 K to 1500 K [3, 47, 48] so that radiation effects become especially important. The speeds of vacuum processes are slower than in-air processes, around 0.1 m/min - 0.2 m/min [3, 6]. To make a case study of the temperature and stress distributions in vacuum R2R processes, we choose a carbon cloth film with the same dimension as the PET film shown in Figure 2.2, under the same shape, location and effective beam radius heat flux but with a higher maximal heat flux density 229.1831 kW/m^2. The physical properties for the computation are shown in Table 2.2 [49-52]. With these parameters, the peak temperature for the stationary web is 1102.01 K, which is in the range of typical working temperature for such vacuum systems.

(h) For the identical transport speed as for the PET web computation, the temperature field in Figure 2.3(f) is much wider due to web transport/internal convection than that in Figure 2.2 (c). This is because the conductivity term, $k(T_{,11}+T_{,33})$ in Eq. (2.18), plays a more important role compared to web transport related internal convection term for conductive webs such as for carbon cloth.

(i) Regions with compressive principle stresses correspond to regions of incident heat flux as expected.

(j) Similar to PET films in air, as shown in Figure 2.3, the temperature and stress fields become asymmetric due to web transport.

Table 2.2. Physical properties of the carbon cloth film.

Mass density ρ (kg/m^3) [d]	Young's Modulus E (GPa) [d]	Thermal conductivity k $(W/(m\cdot K))$ [d]	Specific heat capacity c $(kJ/(kg\cdot K))$ [d]	Coefficient of thermal expansion α_T $(m/(m\cdot K))$[d]	Web width b (cm)
2.26×10^3	9.5	110	0.71	2.5×10^{-5}	15.24
Web thickness t (μm)	Emissivity factor $\tilde{\varepsilon}$ [e]	Poisson's ratio v [d]	Gravitational acceleration g (m/s^2)	Ambient temperature T_a $(^\circ C)$	
96.52	0.9	0.15	9.8	25	

d *'s are from literatures* [49-52].
e *is measured by a ThermaCAM® SC 300 IR* camera.

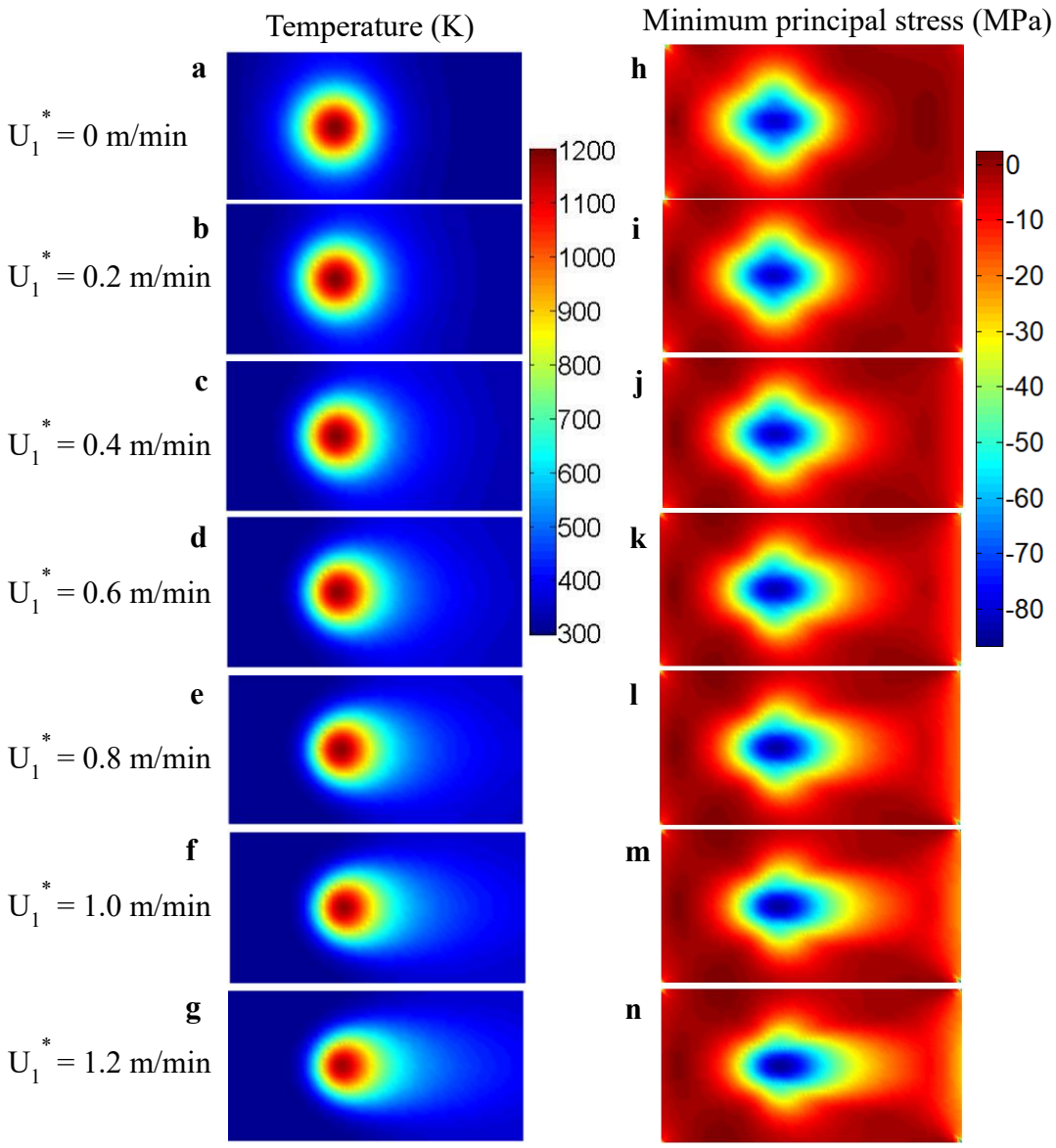

Figure 2.3. The temperature and stress distributions of a carbon cloth film in vacuum R2R processes at different transport speeds. The heat flux used here is a same one as in Figure 2.2(a) but with maximal heat flux density 229.1831 kW/m^2. (a)-(g) are the temperature distributions under different web speeds. (h)-(n) are the minimum principal stress distributions under different web speeds with a pre-tension along longitudinal direction of 100 N/m, i.e. axial pre-stress of 1.036 MPa.

2.4 Experimental Validation

We are not aware of any prior experimental validation of R2R web thermomechanics in the literature. Arguably, the biggest challenges to experimental validation include (a) the choice of an

appropriate non-uniform heat source, and (b) the identification of the incident heat flux distribution on the web.

To make sure the heat flux is consistent in the experiments we must choose a heat source whose shape and magnitude will not change under different web speeds. Non-contact heat sources such as local convection heaters will result in incident heat flux that varies with web transport since the web transport can modify local convection coefficients. Hence, we must choose a heat source based on thermal radiation only, and a CO_2 continuous wave IR laser is used as a heat source. The laser head we chose is Diamond C-20A from Coherent® with wavelength from 10.55 um to 10.63 um. In this wavelength range, both white paper and PET have a strong absorption. A Diamond GEM PC-1 controller from Coherent® is used to adjust output power of the laser head from 200 mW to 20 W. The controller is slightly tuned in order to obtain a power which can raise the peak temperature to a value that can easily be measured but yet that is not enough to burn the web. The power supply for laser head we used is Mean Well RSP-750-48. A 6× beam expander (BECZ-10.6-C0.9:2.79-D6-MI) from II-VI infrared is aligned to expend the laser beam size. The laser beam transports through beam expander and heating on the web.

To identify the incident heat flux distribution experimentally for each type of web material tested, we use the following inverse method. First, we heat up the stationary web with the CO_2 continuous wave IR laser operated at a fixed power input. We use an IR camera to measure the resulting temperature distribution. A ThermaCAM® SC 300 IR camera is used to help align the laser head, beam expander, and web, and to capture IR images of temperature distribution on the web. Plugging all known web properties in Eq. (2.21), we can obtain the shape of heat flux at the computational nodes. Once the incident heat flux is identified for the stationary web, the computational model for the axially moving web is validated by comparing the resulting temperature distributions from FEM and experiments on the moving web.

In our validation, we compared the temperature fields from experiments to predictions from our model as well as by using Brockmann's method [27] under a same heat flux input.

Figure 2.4(a) shows the setup of the system and the 2D measured temperature maps of an opaque PET web. As shown in Figures 2.4(b)-(i), we used two types of web for validation: white paper web (ER019BX17 from Anchor Paper) and white opaque PET web (Melinex® 329 from DuPont Teijin Film). The properties of environment are $g = 9.8m/s^2, T_a = 21°C$. Other properties of PET web can be found in Table 2.1. The properties of white paper web are in Table 2.3 [38, 53,

54]. The background noise in experimental data comes from the sensor of the IR camera, such as focal plane array non-uniformity and infrared camera spatial noise [55,56].

For the experimental validation, we change the web speed from 0 to 3 m/min. The convection coefficient used in Brockmann's method is a constant value (not a function of temperature) equaling the average of nonlinear fitted convection coefficients from 300 K to 700 K and 0 to 3 m/min.

The results are shown in Figures 2.4(b)-(i). The experimental data are in blue. The red lines show the simulated results from our model, and the green lines show simulated data from Brockmann's method. Both experimental and simulated data show the asymmetry with respect to the center of the web caused by transport. We can also clearly see the decreasing of peak temperature, which has a nonlinear relation with transport speed.

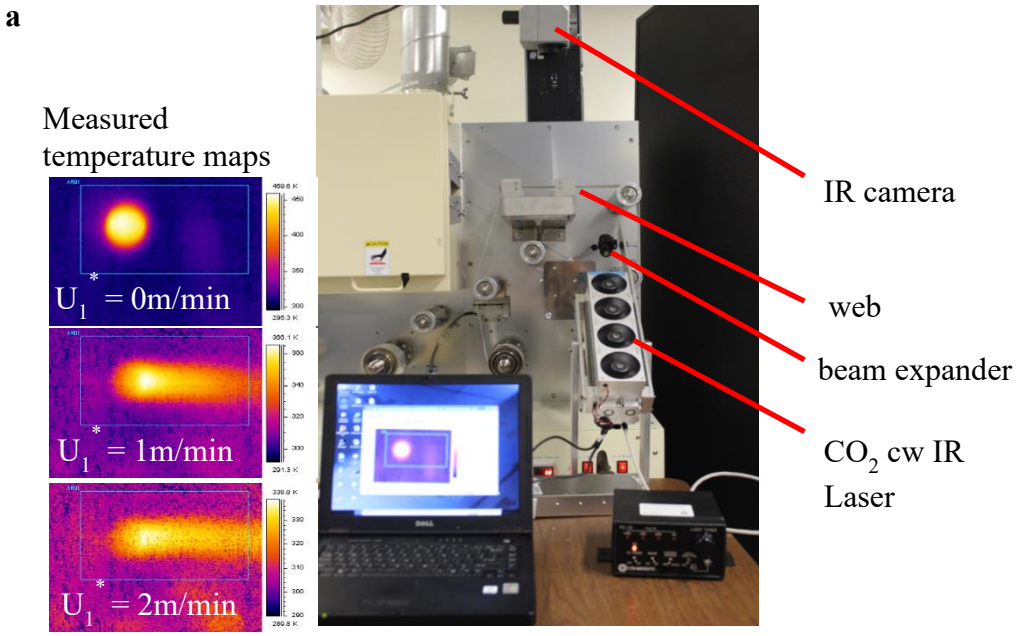

Figure 2.4. (a) The setup of experimental validation and the 2D measured temperature maps of an opaque PET web. (b)-(e) Temperature distributions in midline of white paper web ($x_3 = 0$) under different web speeds. (f)-(i) Temperature distributions in midline of opaque PET web ($x_3 = 0$) under different web speeds. In (b)-(i), comparisons can be made between experimental data (blue circles), our model predictions (red line), and simulated data from Brockmann's method (green line) with constant convection coefficient as the average value of nonlinear fitted convection coefficients.

Figure 2.4 continued

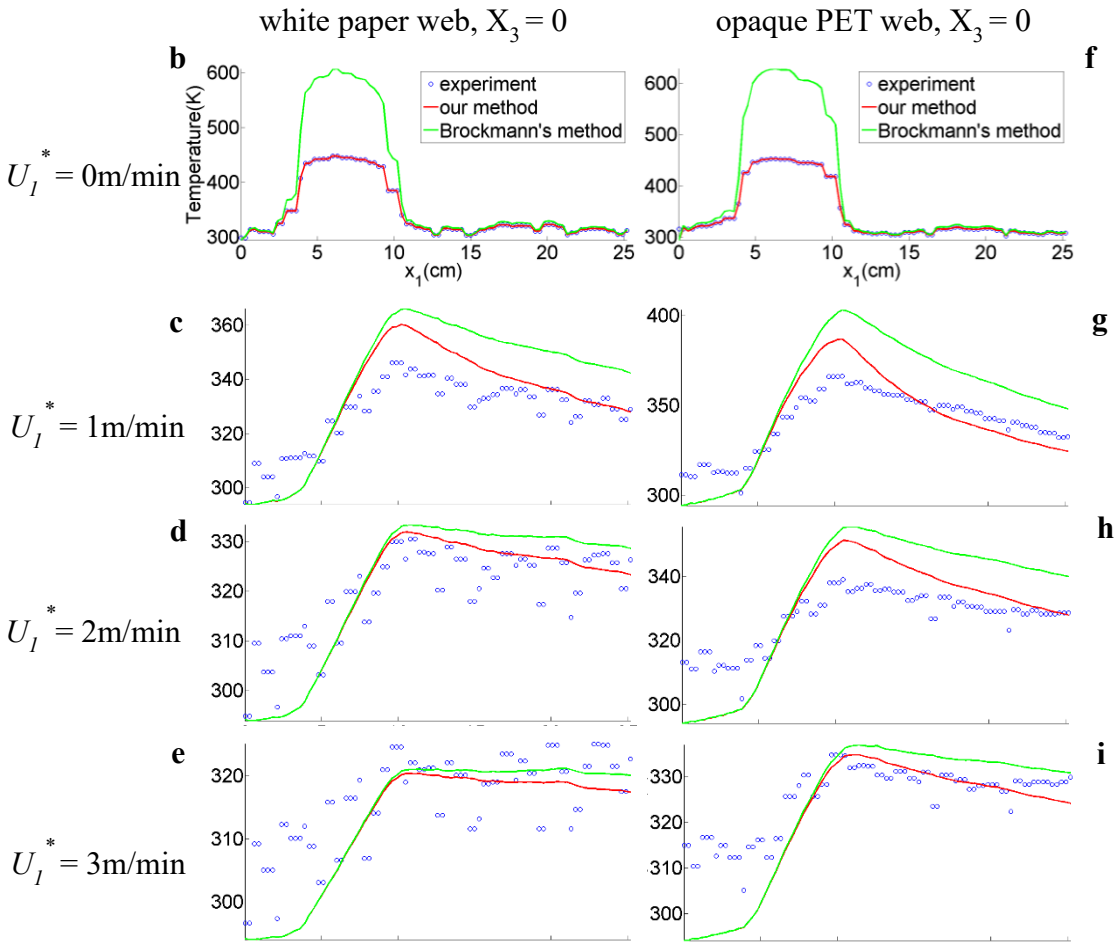

From Figures 2.4(b)-(i), data from our model predictions better matches with experimental data compared with Brockmann's. For paper web with transport speed 1 m/min as in Figure 2.4 (c), our model over predicts the peak temperature increase by 27.06% while Brockmann's model does so by 38.13%; with transport speed 2 m/min as in Figure 2.4(d), our model over predicts the peak temperature by 2.48% while Brockmann's model does so by 6.37%. For PET web with transport speed 1 m/min as in in Figure 2.4(g), our model over predicts the peak temperature by 32.78% while Brockmann's model does so by 54.75%; with transport speed 2 m/min as in Figure 2.4(h), our model over predicts the peak temperature by 28.96% while Brockmann's model does so by 37.53%. Hence, Brockmann's method over predicts the measured temperature distribution compared with our method because of the absence of radiation term in Brockmann's model. However, as the web speed increases both model predictions come closer to experimental data

since the effect of thermal convection (included in both models) increases in comparison to radiation effects.

Table 2.3. Physical properties of the white paper web.

Mass density ρ (kg/m^3) [f]	Young's Modulus E (GPa) [f]	Thermal conductivity k $(W/(m\cdot K))$ [g]	Specific heat capacity c $(kJ/(kg\cdot K))$ [g]	Coefficient of thermal expansion α_T $(m/(m\cdot K))$ [g]	Web width b (cm) [f]
1.169×10^3	3.225	0.1	1.26	6.4×10^{-6}	15
Web thickness t (μm) [f]	Emissivity factor $\tilde{\varepsilon}$ [f]	Poisson's ratio v [g]	Gravitational acceleration g (m/s^2)	Ambient temperature T_a $(^\circ C)$ [f]	
160	0.86	0.2	9.8	21 (*i.e.* 294.15 K)	

f*'s are self-measured.*
g*'s are from literatures* [38, 53, 54].

2.5 Conclusions

An accurate thermomechanics model of an axially moving web subject to arbitrary heat flux is theoretically developed and experimentally validated. We studied cases representative of both R2R processes in air and in vacuum. Web transport drives asymmetry in both temperature and stress fields and significantly influences the peak values of temperature increase and principal stress. Compressive stresses may cause web wrinkling, which mostly happens around the regions of incident heat flux. With a fixed heat flux, the magnitudes of peak temperature and compressive stress reduce with increasing web speed. The local web temperature can be controlled in a workable range and local web wrinkling can be avoided by adjusting the amplitude of heat flux for different web speeds. With aid of such modeling and simulation tools, we hope that a variety of R2R systems for nanomanufacturing and flexible electronics manufacturing can be optimized for improved yield and product quality.

2.6 References

[1] Bae, S., Kim, H., Lee, Y., Xu, X., Park, J. S., Zheng, Y., ... & Iijima, S. (2010). Roll-to-roll production of 30-inch graphene films for transparent electrodes. *Nature nanotechnology*, *5*(8), 574.

[2] Guo, Y., Batra, S., Chen, Y., Wang, E., & Cakmak, M. (2016). Roll to roll electric field "Z" alignment of nanoparticles from polymer solutions for manufacturing multifunctional capacitor films. *ACS applied materials & interfaces*, *8*(28), 18471-18480.

[3] Kobayashi, T., Bando, M., Kimura, N., Shimizu, K., Kadono, K., Umezu, N., ... & Hobara, D. (2013). Production of a 100-m-long high-quality graphene transparent conductive film by roll-to-roll chemical vapor deposition and transfer process. *Applied Physics Letters*, *102*(2), 023112.

[4] Krebs, F. C. (2009). All solution roll-to-roll processed polymer solar cells free from indium-tin-oxide and vacuum coating steps. *Organic Electronics*, *10*(5), 761-768.

[5] Krebs, F. C., Tromholt, T., & Jørgensen, M. (2010). Upscaling of polymer solar cell fabrication using full roll-to-roll processing. *Nanoscale*, *2*(6), 873-886.

[6] Park, Y. S., Choi, K. H., & Kim, H. K. (2009). Room temperature flexible and transparent ITO/Ag/ITO electrode grown on flexile PES substrate by continuous roll-to-roll sputtering for flexible organic photovoltaics. *Journal of Physics D: Applied Physics*, *42*(23), 235109.

[7] Perelaer, J., Abbel, R., Wünscher, S., Jani, R., Van Lammeren, T., & Schubert, U. S. (2012). Roll-to-roll compatible sintering of inkjet printed features by photonic and microwave exposure: from non-conductive ink to 40% bulk silver conductivity in less than 15 seconds. *Advanced materials*, *24*(19), 2620-2625.

[8] Søndergaard, R., Hösel, M., Angmo, D., Larsen-Olsen, T. T., & Krebs, F. C. (2012). Roll-to-roll fabrication of polymer solar cells. *Materials today*, *15*(1-2), 36-49.

[9] Yeo, L. P., Ng, S. H., Wang, Z., Wang, Z., & de Rooij, N. F. (2009). Micro-fabrication of polymeric devices using hot roller embossing. *Microelectronic engineering*, *86*(4-6), 933-936.

[10] Abouelregal, A. E., & Zenkour, A. M. (2015). Thermoelastic problem of an axially moving microbeam subjected to an external transverse excitation. *Journal of Theoretical and Applied Mechanics*, *53*(1), 167-178.

[11] Guo, X., Wang, Z., Wang, Y., & Zhou, Y. (2009). Analysis of the coupled thermoelastic vibration for axially moving beam. *Journal of Sound and Vibration*, *325*(3), 597-608.

[12] Guo, X., & Wang, Z. (2010). Thermoelastic coupling vibration characteristics of the axially moving beam with frictional contact. *Journal of vibration and acoustics*, *132*(5).

[13] Guo, X., Wang, Z., & Wang, Y. (2011). Dynamic stability of thermoelastic coupling moving plate subjected to follower force. *Applied acoustics*, *72*(2-3), 100-107.

[14] Kazemirad, S., Ghayesh, M. H., & Amabili, M. (2013). Thermo-mechanical nonlinear dynamics of a buckled axially moving beam. *Archive of Applied Mechanics*, *83*(1), 25-42.

[15] Kazemirad, S., Ghayesh, M. H., & Amabili, M. (2013). Thermal effects on nonlinear vibrations of an axially moving beam with an intermediate spring-mass support. *Shock and Vibration*, *20*(3), 385-399.

[16] Kwon, K., & Lee, U. (2006). Spectral element modeling and analysis of an axially moving thermoelastic beam-plate. *Journal of Mechanics of Materials and Structures*, *1*(4), 605-632.

[17] Zenkour, A. M., Abouelregal, A. E., & Abbas, I. A. (2014). Generalized thermoelastic vibration of an axially moving clamped microbeam subjected to ramp-type thermal loading. *Journal of Thermal Stresses*, *37*(11), 1302-1323.

[18] Frechard, J., & Knittel, D. (2012, July). Advanced optimization of industrial large-scale roll-to-roll systems under parametric uncertainties. In *Engineering Systems Design and Analysis* (Vol. 44847, pp. 263-270). American Society of Mechanical Engineers.

[19] Lee, C., Kang, H., & Shin, K. (2010). A study on tension behavior considering thermal effects in roll-to-roll E-printing. *Journal of mechanical science and technology*, *24*(5), 1097-1103.

[20] Lu, Y., & Pagilla, P. R. (2013, October). Modeling the effects of heat transfer processes on material strain and tension in roll to roll manufacturing. In *Dynamic Systems and Control Conference* (Vol. 56147, p. V003T48A004). American Society of Mechanical Engineers.

[21] Lu, Y., & Pagilla, P. R. (2014, June). Adaptive control of web tension in a heat transfer section of a roll-to-roll manufacturing process line. In *2014 American Control Conference* (pp. 1799-1804). IEEE.

[22] Lu, Y., & Pagilla, P. R. (2015, October). A Nonlinear Tension Control Scheme for Web Transport Through Heating Processes. In *Dynamic Systems and Control Conference* (Vol. 57250, p. V002T32A006). American Society of Mechanical Engineers.

[23] Seo, I. S., Song, J. H., Shin, J. M., & Kim, J. S. (2009, August). A tension control for web transportation in continuous annealing processes. In *2009 7th Asian Control Conference* (pp. 1420-1425). IEEE.

[24] Lu, Y., & Pagilla, P. R. (2012, October). Modeling of temperature distribution in a moving web transported over a heat transfer roller. In *Dynamic Systems and Control Conference* (Vol. 45301, pp. 405-414). American Society of Mechanical Engineers.

[25] Lu, Y., & Pagilla, P. R. (2014). Modeling of temperature distribution in moving webs in roll-to-roll manufacturing. *Journal of Thermal Science and Engineering Applications*, *6*(4).

[26] Kurki, M., Jeronen, J., Saksa, T., & Tuovinen, T. (2016). The origin of in-plane stresses in axially moving orthotropic continua. *International Journal of Solids and Structures*, *81*, 43-62.

[27] Brockmann, R., Dickmann, K., Geshev, P., & Matthes, K. J. (2003). Calculation of temperature field in a thin moving sheet heated with laser beam. *International journal of heat and mass transfer*, *46*(4), 717-723.

[28] Brockmann, R., Dickmann, K., Geshev, P., & Matthes, K. J. (2003). Calculation of laser-induced temperature field on moving thin metal foils in consideration of Stefan problem. *Optics & Laser Technology*, *35*(2), 115-122.

[29] Baïri, A., De Maria, J. G., & Laraqi, N. (2004). Effect of thickness and physical properties of films on the thermal behavior of a moving rough interface. *The European Physical Journal-Applied Physics*, *26*(1), 29-34.

[30] Duhamel, J. M. (1837). Second memoire sur les phenomenes thermo-mecaniques. *Journal de l'École polytechnique*, *15*(25), 1-57.

[31] Voigt, W. (1910). *Lehrbuch der kristallphysik:(mit ausschluss der kristalloptik)* (Vol. 34). BG Teubner.

[32] Landau, L. D., & Lifshitz, E. M. (1959). *Course of theoretical physics*. (Vol. 7): Theory and Elasticity, Pergamon Press.

[33] Bergman, T. L., Incropera, F. P., DeWitt, D. P., & Lavine, A. S. (2011). *Fundamentals of heat and mass transfer*. John Wiley & Sons.

[34] Kovalenko, A. D. (1969). *Thermoelasticity: basic theory and applications*. Wolters-Noordhoff.

[35] Nowacki, W. (1968). Couple-stresses in the theory of thermoelasticity. In *Irreversible Aspects of Continuum Mechanics and Transfer of Physical Characteristics in Moving Fluids* (pp. 259-278). Springer, Vienna.

[36] Boley, B. A., & Weiner, J. H. (2012). *Theory of thermal stresses*. Courier Corporation.

[37] Iimure, N. (1958). Ignition temperature. *Manual for Dangerous Article Treating (Kikenbutsu Toriatsukai Hikkei). Sangyo Tosho Co., Tokyo*, 62-63.

[38] Mark, R. E., Borch, J., & Habeger, C. (Eds.). (2002). *Handbook of physical testing of paper* (Vol. 1). Crc Press.

[39] DuPont Teijin Films, Mylar Physical Properties. (2018, August 17). Retrieved from http://usa.dupontteijinfilms.com/wp-content/uploads/2017/01/Mylar_Physical_Properties.pdf

[40] TEIJIN Film Solutions Limited, PEN film. (2018, August 17). Retrieved from http://www.teijinfilmsolutions.jp/english/product/pen_teo.html

[41] Hashimoto, H. (2007). Prediction model of paper-web wrinkling and some numerical calculation examples with experimental verifications. *Microsystem technologies*, *13*(8-10), 933-941.

[42] Kim, T. Y., Puntel, E., & Fried, E. (2012). Numerical study of the wrinkling of a stretched thin sheet. *International Journal of Solids and Structures*, *49*(5), 771-782.

[43] Roisum, D. R. (1996). The mechanics of wrinkling. *Tappi journal*, *79*(10), 217-226.

[44] Puntel, E., Deseri, L., & Fried, E. (2011). Wrinkling of a stretched thin sheet. *Journal of Elasticity*, *105*(1-2), 137-170.

[45] Lin, C. C., & Mote Jr, C. D. (1996). The wrinkling of thin, flat, rectangular webs. ASME *Journal of Applied Mechanics*, 63(3), 774-779

[46] Vaughan, M., & Raman, A. (2010). Aeroelastic stability of axially moving webs coupled to incompressible flows. *Journal of Applied Mechanics*, *77*(2).

[47] Shivkumar, G., Tholeti, S. S., Alrefae, M. A., Fisher, T. S., & Alexeenko, A. A. (2016). Analysis of hydrogen plasma in a microwave plasma chemical vapor deposition reactor. *Journal of Applied Physics*, *119*(11), 113301.

[48] Xiong, G., Hembram, K. P. S. S., Zakharov, D. N., Reifenberger, R. G., & Fisher, T. S. (2012). Controlled thin graphitic petal growth on oxidized silicon. *Diamond and related materials*, *27*, 1-9.

[49] Ho, F. H. (1988). *Graphite design handbook* (No. DOE/HTGR-88111). General Atomics, San Diego, CA (US).

[50] Klett, J. W., & Edie, D. D. (1995). Flexible towpreg for the fabrication of high thermal conductivity carbon/carbon composites. *Carbon*, *33*(10), 1485-1503.

[51] Pierson, H. O. (2012). *Handbook of carbon, graphite, diamonds and fullerenes: processing, properties and applications*. William Andrew.

[52] Shackelford, J. F., Han, Y. H., Kim, S., & Kwon, S. H. (2016). *CRC materials science and engineering handbook*. CRC press.

[53] Cao, X., Bi, Z., Wei, X., & Xie, Y. (2012). Determination of Poisson's ratio of Kraft paper using digital image correlation. In *Mechanical Engineering and Technology* (pp. 51-57). Springer, Berlin, Heidelberg.

[54] Lavrykov, S. A., & Ramarao, B. V. (2012). Thermal properties of copy paper sheets. *Drying Technology*, *30*(3), 297-311.

[55] Mooney, J. M., & Shepherd, F. D. (1996). Characterizing IR FPA nonuniformity and IR camera spatial noise. *Infrared physics & technology*, *37*(5), 595-606.

[56] Ibarra-Castanedo, C., Gonzalez, D., Klein, M., Pilla, M., Vallerand, S., & Maldague, X. (2004). Infrared image processing and data analysis. *Infrared physics & technology*, *46*(1-2), 75-83.

[57] Wilson, I., Ladizesky, N. H., & Ward, I. M. (1976). The determination of Poisson's ratio and extensional modulus for polyethylene terephthalate sheets by an optical technique. *Journal of Materials Science*, *11*(12), 2177-2180.

3. VIBRATIONS OF AIR-COUPLED WEB SYSTEMS

This Chapter was published in Journal of Vibration and Acoustics (DOI: 10.1115/1.4047702). We acknowledge the permission of copyright by ASME to include it in this dissertation.

3.1 Introduction

Flexible hybrid electronics and stretchable electronics are rapidly growing technology sector with a global market expected to exceed $75 Billion the early 2020's as reported by the National Academies [1]. Because of the diverse applications of flexible electronics to photovoltaics, batteries, sensors for Internet of Things (IoT), human wearable devices, flexible lighting, and flexible displays [2-5], the growth of flexible electronics coincides with the digital transformation of many industry sectors.

Roll-to-roll (R2R) processes offer generic technology platforms for scale-up of flexible electronics manufacturing to reduce the cost and increase the volume throughput [6-9]. Figure 3.1 shows a flexible thin web cross a span between two rollers in a typical R2R manufacturing set up for flexible electronics manufacturing. There is increasing interest the thermomechanics [8, 9] and vibrations of tensioned webs in R2R processes for process monitoring, quality control, and process stability [10-19].

Web vibration can be detrimental to process control; thus, several groups have worked on web vibration control [12, 14, 15]. Web systems designers are interested in ensuring that the web frequencies are tuned away from several external excitation sources in the R2R process. For example, in printing applications, the web vibration frequency will need to be tuned away from the firing frequency of printer heads. In addition, web frequencies need to be tuned away from roller-eccentricity induced boundary excitation frequencies in processes.

On the other hand, intentional excitation and measurement of vibration modes may serve as a way for generating non-uniform distributed functional patterns (such as Chladni patterns) in wet coated layer on flexible thin substrates [20-23] or to measure web pre-tension instead of using load cells [16, 17]. Intentional modal vibrations might also be used for rapid in-line reliability monitoring of R2R products, including thin film delamination and cracking, instead of traditional off-line cyclic bending and torsion tests [6, 24]. Characterization of web vibration may also enable

new ways of strain distribution monitoring or damage detection in R2R flexible electronics manufacturing.

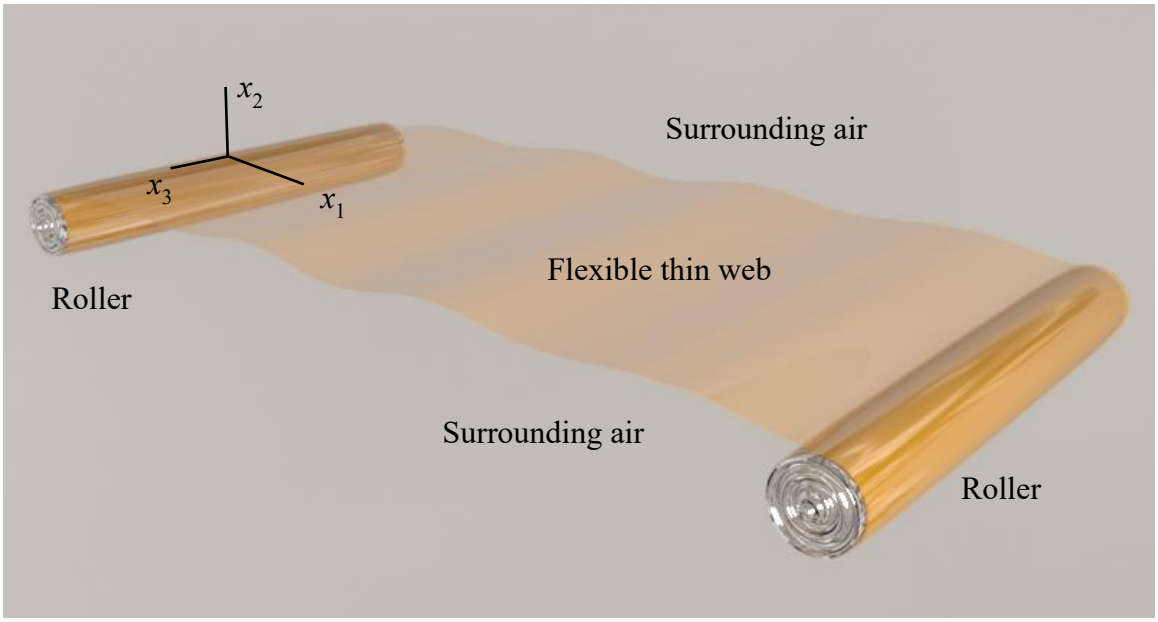

Figure 3.1. An air-coupled flexible thin spans between two rollers in R2R processes. Web vibration utilization or mitigation applications in such R2R processes include: Vibration isolation or vibration control [12, 14, 15]; Web pre-tension prediction [16, 17]; Self-assembly of patterns [20-23]; Cyclic bending and torsion tests [6, 24].

The vibrations of thin flexible webs in R2R processes in flexible electronics manufacturing are significantly affected by surrounding air, which can reduce the frequencies and changes the mode shapes in comparison to those *in vacuo*. This is primarily because the mass density of thin polymer or paper typically used as substrates in flexible electronics manufacturing are much smaller compared to sheet metal. As such the surrounding air couples strongly with the transverse vibration of such taut webs over their large area and must be considered to accurately predict web frequencies, mode shapes, or web pre-tension. Pramila *et al.* [25, 26] first investigated this using potential flow theory for the surrounding air and a uniaxially tensioned membrane model for the web. However, the linear eigenvalue problem for out-of-plane vibration of a uniaxially tensioned membrane is ill-posed, in that the spatial dependence of any eigenmode in a direction transverse to the tension cannot be defined. The work is followed by Chang and Moretti [27], Vaughan and Raman [10, 11], Hara and Watanabe [28, 29], Yao and Zhang [30] who used a uniaxially tensioned Kirchhoff plate model and investigated free edge flutter and web stability caused by cross flow.

Most of these works assume the air is incompressible, inviscid, and irrotational. Kulachenko, Gradin, and Koivurova [31] used the Helmholtz equation since they assume surrounding air is compressible. Noting that potential flow theory is not suitable for edge wake phenomena when airflow occurs transverse to the tensioned direction, Bidkar, Raman, and Bajaj [32] used a vortex-lattice method for inviscid and incompressible flows. However, all these previous works require significant computational work to determine the effect of surrounding air on the web vibration. As such these computational approaches are not easily accessible to web systems designers and controllers.

One way to make aerodynamic/ hydrodynamic coupling easily accessible is by generating easy-to-use semi-analytical expressions for the coupling based on detailed computations. The trick here is to make the hydrodynamic functions as "Universal" as possible, so that they represent a wide range of operating conditions, properties, and geometries relevant to the application. One such example of accessible and thus highly utilized hydrodynamic functions are Sader's functions [33, 34] that can predict the added mass and viscous damping of multiple modes of microcantilevers immersed in fluids for use in the Atomic Force Microscope. Sader's hydrodynamic functions are based on two-dimensional computational solutions of linearized, unsteady, incompressible Navier Stokes equations and are valid over a wide range of unsteady Reynold's numbers, microcatilever geometries and surrounding fluid properties.

In this chapter we present closed-form, semi-analytical hydrodynamic functions for the accurate prediction of air-coupled vibration response of uniaxially tensioned webs valid over two orders of magnitude of range of web aspect ratio, and for arbitrary web material mass density and tension. The taut webs are considered stationary because many flexible electronics manufacturing operations work at low speeds (less than 3.5 m/min [3,6,9]). The primary interest is on the added mass effect of air-coupling. Thus, the hydrodynamic functions presented here are based on three-dimensional computations of webs coupled with incompressible, inviscid, irrotational surrounding fluid. Specifically, we present hydrodynamic functions for the two lowest frequency eigenmodes of the web. The hydrodynamic functions for other eigenmodes can be obtained following our method shown in Section 3.2.4. The hydrodynamic functions are validated in experiments using acoustically excited and laser-measured web vibrations with three different types of web materials with various in-span length to width ratios and pre-tensions. The hydrodynamic functions for air-coupled web vibrations derived in this chapter will allow R2R web system designers, and R2R

system dynamics and control engineers estimate the transverse web frequencies using simple formulas rather than through the use of expensive computational models. The only data needed to determine the air-added effects for lowest eigenmodes are the uniaxial tension, length, aspect ratio, and mass areal density of any rectangular web, as well as the density of surrounding air (or other fluid).

3.2 Mathematical Models of Air-Coupled Web Systems

3.2.1 Field Equations for the Coupled System and Their Discretization

Inspired by prior works on vibration of metal plates submerged in water with applications to ship research [35-37], in this section we develop a solution method to couple a 2D tensioned web model with a 3D potential flow model for surrounding air. The ratio of air mass density to web material mass density is an important indicator of the strength of the air-coupling effect on web vibrations and is much greater for typical web materials (plastics, papers) used in R2R manufacturing than for metal webs. As a result, the effect of surrounding air on the vibrations of flexible taut webs in R2R processes is expected to be significant in a similar manner as the effect of surrounding water on the vibration of submerged metal plates.

We assume the rectangular web cross a span between two rollers in R2R with 2D isotropic, linearly elastic, uniaxially tensioned Kirchhoff plate. A linear membrane model for a uniaxially tensioned web leads to non-unique eigenfunction dependence along the direction transverse to the tension. Hence, we choose to include very small but finite bending stiffness of a uniaxially tensioned plate in the model for the vibrating web. In-plane oscillations and out-of-plane oscillations are uncoupled in this flat tensioned plate model. The equation of motion for out-of-plane vibrations of an axially stationary web can be derived from Hamilton's principle as [10, 11, 38]

$$\rho_{web}\ddot{w}(x_1, x_3, \tau) + D\nabla^4 w(x_1, x_3, \tau) - N_{11} w_{,11}(x_1, x_3, \tau) = p, \tag{3.1}$$

where x_1, x_2, and x_3 are the coordinates along longitudinal (in the plane of the web along the direction of applied tension), transverse (normal to web surface), and lateral directions (in the plane of the web), respectively, as shown in Figure 3.1; τ is the time, $w(x_1, x_3, \tau)$ is the web deflection transverse to the plane of the web; ρ_{web} is the web areal mass density; $D = Eh^3/[12(1-\upsilon^2)]$ is the

web bending stiffness, with E, h, and υ denoting Young's modulus, thickness, and Poisson's ratio of the web, respectively; ∇^4 is the biharmonic operator; N_{11} is the web's uniaxial pre-tension per unit width; p is the aerodynamic pressure differential between the bottom surface and upper surface of the vibrating web.

We choose a 3D potential flow model for the surrounding air assuming the surrounding air is initially quiescent (no bulk velocity or transport) and is incompressible, inviscid, and irrotational. This is because compared to broad R2R applications, the R2R processes for flexible electronics are typically with low speed (less than 3.5 m/min [3, 6, 9]) with quiet manufacturing environments and thus near-quiescent conditions. In addition, the flow can be considered incompressible since the transverse vibration frequencies are very slow. Since the focus of the work is on added mass effect of the air, we assume that the surrounding fluid is inviscid. The assumption of irrotational flow follows from the fact that we are not considering steady air flows over free edges which would lead to vortices [32]. Then the aerodynamics of surrounding air is coupled to the web vibration through the surface pressure differential as [10, 11, 25]

$$p = 2\rho_{air}\dot{\phi}(x_1, 0^+, x_3, \tau), \tag{3.2}$$

where the factor "2" comes from the anti-symmetric aerodynamic pressure on the two surfaces of the web; ρ_{air} is the density of surrounding air; $\phi(x_1, 0^+, x_3, \tau)$ is the velocity potential of air on the web; and $\dot{\phi}(x_1, 0^+, x_3, \tau) = \dfrac{\partial \phi(x_1, 0^+, x_3, \tau)}{\partial \tau}$. Substituting Eq. (3.1) into Eq. (3.2), we obtain the governing equation of the vibrating web coupled to surrounding air as

$$\rho_{web}\ddot{w}(x_1, x_3, \tau) + D\nabla^4 w(x_1, x_3, \tau) - N_{11}w_{,11}(x_1, x_3, \tau) = 2\rho_{air}\dot{\phi}(x_1, 0^+, x_3, \tau). \tag{3.3}$$

The continuity equation of the surrounding potential flow can be written as a Laplace's equation

$$\nabla^2\phi(x_1, x_2, x_3, \tau) = \frac{\partial^2\phi(x_1, x_2, x_3, \tau)}{\partial x_1^2} + \frac{\partial^2\phi(x_1, x_2, x_3, \tau)}{\partial x_2^2} + \frac{\partial^2\phi(x_1, x_2, x_3, \tau)}{\partial x_3^2} = 0, \tag{3.4}$$

where ∇^2 is the Laplace operator, $\phi(x_1, x_2, x_3, \tau)$ is the velocity potential of air. The gradient of the velocity potential gives component of velocity of air along its direction. Thus, the velocity of air normal to the web equals the normal vibrating velocity of the web, *i.e.*

$$-\phi_{,2}(x_1, 0^+, x_3, \tau) = \dot{w}(x_1, x_3, \tau). \tag{3.5}$$

Next we nondimensionalize Eqs. (3.3) - (3.5) as [10,11]

$$x_1' = \frac{x_1}{L}, x_2' = \frac{x_2}{L}, w' = \frac{w}{L}, x_3' = \frac{x_3}{L},$$
$$\varepsilon = \frac{D}{L^2 N_{11}}, \Lambda = \frac{L\rho_{air}}{\rho_{web}}, \tau' = \frac{\tau}{L}\sqrt{\frac{N_{11}}{\rho_{web}}}, \phi' = \frac{\phi}{L}\sqrt{\frac{\rho_{web}}{N_{11}}}, \tag{3.6}$$

where L is the in-span length of web in longitudinal direction, ε is the bending stiffness to tension ratio, and Λ is some measure of air density to areal mass density of web. The primes denote the nondimensional quantities. ε is normally very small, ranging from 10^{-6} to 10^{-4}, but non-negligible for taut webs used in flexible electronics applications. It distinguishes the spatial dependence of eigenmodes in lateral direction. Using Eq. (3.6), we can rewrite Eqs. (3.3) - (3.5) in nondimensional form as

$$\ddot{w}'(x_1', x_3', \tau') + \varepsilon\nabla^4 w'(x_1', x_3', \tau') - w'_{,11}(x_1', x_3', \tau') = 2\Lambda\dot{\phi}'(x_1', 0^+, x_3', \tau'), \tag{3.7}$$

$$\nabla^2\phi'(x_1', x_2', x_3', \tau') = 0, \tag{3.8}$$

$$-\phi'_{,2}(x_1', 0^+, x_3', \tau') = \dot{w}'(x_1', x_3', \tau'). \tag{3.9}$$

The associated boundary conditions are:

1. Turnbull *et al*. [39] proved that simply supported boundary conditions are adequately accurate assumptions to predict linear vibrations of pre-tensioned webs across finite radius rollers

$$w'(0, x_3', \tau') = w'(1, x_3', \tau') = 0, w'_{,11}(0, x_3', \tau') = w'_{,11}(1, x_3', \tau') = 0; \tag{3.10}$$

2. there is no shear force or bending moment for the free edges

$$w'_{,33}(x_1', \pm 1/(2\kappa), \tau') + \upsilon w'_{,11}(x_1', \pm 1/(2\kappa), \tau) = 0,$$
$$w'_{,333}(x_1', \pm 1/(2\kappa), \tau') + (2-\upsilon) w'_{,311}(x_1', \pm 1/(2\kappa), \tau') = 0; \tag{3.11}$$

3. the fluid is allowed to exchange between the upper and lower half space, *i.e.* the web is unbaffled

$$\phi'(x_1', 0, x_3', \tau') = 0, \quad \text{outside the area of web;} \tag{3.12}$$

4. the fluid is stationary in the far field

$$\lim_{\sqrt{x_1'^2 + x_2'^2 + x_3'^2} \to \infty} \phi'_{,normal}(x_1', x_2', x_3', \tau') = 0. \tag{3.13}$$

To solve the coupled eigenvalue problem underlying the free vibrations of the air-coupled web (*i.e.* Eqs. (3.7) - (3.9)), we separate the time and space variables for both the web deflection and the velocity potential of air as

$$w'(x_1', x_3', \tau') = \sum_{m=1}^{\infty}\sum_{n=1}^{\infty} q'_{mn}(\tau') W'_{mn}(x_1', x_3'), \tag{3.14}$$

$$\phi'(x_1', x_2', x_3', \tau') = \sum_{m=1}^{\infty}\sum_{n=1}^{\infty} A'_{mn2}(\tau') \varphi'_{mn2}(x_1', x_2', x_3'). \tag{3.15}$$

where $W'_{mn}(x_1', x_3')$ represents a nondimensional admissible set of basis functions for web vibration, $q'_{mn}(\tau')$ is the generalized coordinate. Basis functions with m and n as odd numbers are symmetric with respect to $x_1' = 0.5$ and $x_3' = 0$, respectively; while those with even-numbered m and n values are anti-symmetric with respect to $x_1' = 0.5$ and $x_3' = 0$, respectively. φ'_{mn2} is the three-dimensional aerodynamic function corresponding to web vibration in the corresponding basis function $W'_{mn}(x_1', x_3')$. The 2's in the subscripts of A'_{mn2} and φ'_{mn2} signify that the components are caused by vibration in the direction normal to the plane of the web. There is no initial cross flow along longitudinal or lateral direction, so no additional terms due to flow transport appear in the equations [11]. Substituting Eqs. (3.14) and (3.15) into (3.9) gives

$$A'_{mn2}(\tau') = -\dot{q}'_{mn}(\tau'), \tag{3.16}$$

$$\varphi'_{mn2,2}(x_1', 0^+, x_3') = W'_{mn}(x_1', x_3'). \tag{3.17}$$

We normalize the web vibration basis functions $W'_{mn}(x_1', x_3')$ as

$$\int_{-1/(2\kappa)}^{1/(2\kappa)} \int_0^1 W'^2_{mn}(x_1', x_3') dx_1' dx_3' = 1, \tag{3.18}$$

where $\kappa \equiv L/b$ is the in-span length to width ratio (*i.e.* aspect ratio) of web, b is the width of web in lateral direction. Combining Eq. (3.7) and Eqs. (3.14) - (3.18) and applying Assumed Modes Method (AMM) with inner products with W'_{mn} yields

$$(\mathbf{I} + 2\Lambda \mathbf{M}'_{air})\ddot{\mathbf{q}}' + \mathbf{K}'\mathbf{q}' = 0, \tag{3.19}$$

where

$$\begin{aligned}(\mathbf{K}')_{ij;mn} = &\int_{-1/(2\kappa)}^{1/(2\kappa)} \int_0^1 \varepsilon [W'_{ij,11}(x_1', x_3') W'_{mn,11}(x_1', x_3') + W'_{ij,33}(x_1', x_3') W'_{mn,33}(x_1', x_3') \\ &+ 2(1-\upsilon) W'_{ij,13}(x_1', x_3') W'_{mn,13}(x_1', x_3') + \upsilon W'_{ij,11}(x_1', x_3') W'_{mn,33}(x_1', x_3') \\ &+ \upsilon W'_{ij,33}(x_1', x_3') W'_{mn,11}(x_1', x_3')] + W'_{ij,1}(x_1', x_3') W'_{mn,1}(x_1', x_3') dx_1' dx_3',\end{aligned} \tag{3.20}$$

$$\left(\mathbf{M}'_{air}\right)_{ij;mn} = \int_{-1/(2\kappa)}^{1/(2\kappa)} \int_0^1 W'_{ij}(x'_1, x'_3)\varphi'_{mn2}(x'_1, 0^+, x'_3)dx'_1dx'_3. \tag{3.21}$$

$\mathbf{q}'$ is the vector of the generalized coordinates $q'_{mn}(\tau')$. The stiffness matrix $\mathbf{K}'$ is symmetric and diagonal. The added air mass matrix $\mathbf{M}'_{air}$ is symmetric but with off-diagonal terms, since the inner products of any two symmetric $W'_{mn}(x'_1, x'_3)$ and $\varphi'_{mn2}(x'_1, 0^+, x'_3)$ or any two anti-symmetric $W'_{mn}(x'_1, x'_3)$ and $\varphi'_{mn2}(x'_1, 0^+, x'_3)$ are not necessarily zero. $\mathbf{M}' = \mathbf{I} + 2\Lambda\mathbf{M}'_{air}$ gives the new mass matrix for the coupled system.

3.2.2 Exact Solutions to the *In Vacuo* Eigenvalue Problem

In the absence of air-coupling ($\Lambda = 0$), exact solutions to the eigenvalue problem can be found conveniently. The *in vacuo* eigenmode W'_{mn} that satisfies the simply supported boundary conditions in Eq. (3.10) can be shown to be

$$W'_{mn}(x'_1, x'_3) = \sin(m\pi x'_1)Y'_{mn}(x'_3), \tag{3.22}$$

where

$$Y'_{mn}(x'_3) = C'_1 \cosh\gamma'_{1mn}x'_3 + C'_2 \sinh\gamma'_{1mn}x'_3 + C'_3 \cos\gamma'_{2mn}x'_3 + C'_4 \sin\gamma'_{2mn}x'_3, \tag{3.23}$$

$$\gamma'_{1mn} = \sqrt{\sqrt{\frac{\omega'^2_{mn} - m^2\pi^2}{\varepsilon}} + m^2\pi^2}, \gamma'_{2mn} = \sqrt{\sqrt{\frac{\omega'^2_{mn} - m^2\pi^2}{\varepsilon}} - m^2\pi^2}. \tag{3.24}$$

Additionally, the boundary conditions in Eq. (3.11) can be simplified as

$$\begin{bmatrix} B'_1 \cosh\frac{\gamma'_{1mn}}{2\kappa} & -B'_2 \cos\frac{\gamma'_{2mn}}{2\kappa} \\ B'_3 \sinh\frac{\gamma'_{1mn}}{2\kappa} & B'_4 \sin\frac{\gamma'_{2mn}}{2\kappa} \end{bmatrix} \begin{Bmatrix} C'_1 \\ C'_3 \end{Bmatrix} = 0, \tag{3.25}$$

or

$$\begin{bmatrix} B'_1 \sinh\frac{\gamma'_{1mn}}{2\kappa} & -B'_2 \sin\frac{\gamma'_{2mn}}{2\kappa} \\ B'_3 \cosh\frac{\gamma'_{1mn}}{2\kappa} & -B'_4 \cos\frac{\gamma'_{2mn}}{2\kappa} \end{bmatrix} \begin{Bmatrix} C'_2 \\ C'_4 \end{Bmatrix} = 0, \tag{3.26}$$

where $B'_1 = \gamma'^2_{1mn} - \upsilon m^2\pi^2$, $B'_2 = \gamma'^2_{2mn} + \upsilon m^2\pi^2$, $B'_3 = \gamma'^3_{1mn} - 2m^2\pi^2\gamma'_{1mn} + \upsilon m^2\pi^2\gamma'_{1mn}$, $B'_4 = \gamma'^3_{2mn} + 2m^2\pi^2\gamma'_{2mn} - \upsilon m^2\pi^2\gamma'_{2mn}$. The *in vacuo* mode frequency ω'_{mn} can be solved by letting

$$\begin{vmatrix} B_1' \cosh \frac{\gamma_{1mn}'}{2\kappa} & -B_2' \cos \frac{\gamma_{2mn}'}{2\kappa} \\ B_3' \sinh \frac{\gamma_{1mn}'}{2\kappa} & B_4' \sin \frac{\gamma_{2mn}'}{2\kappa} \end{vmatrix} = 0, \text{ or } \begin{vmatrix} B_1' \sinh \frac{\gamma_{1mn}'}{2\kappa} & -B_2' \sin \frac{\gamma_{2mn}'}{2\kappa} \\ B_3' \cosh \frac{\gamma_{1mn}'}{2\kappa} & -B_4' \cos \frac{\gamma_{2mn}'}{2\kappa} \end{vmatrix} = 0. \tag{3.27}$$

We obtain γ_{1mn}' and γ_{2mn}' by substituting ω_{mn}' into Eq. (3.24), and solve for C_1', C_2', C_3', and C_4' by Eqs. (3.25) and (3.26) with normalization of W_{mn}' as in Eq. (3.18).

The lowest symmetric and anti-symmetric *in vacuo* eigenmodes corresponding to $m=1$, $n=1$ and $m=1$, $n=2$ respectively can be seen in the inset of Figure 3.2. They can be understood as the lowest bending and torsion dominated modes of the web, respectively. The air-coupling significantly changes both the natural frequencies as well as the shapes of these eigenfunctions as will be discussed in subsequent sections.

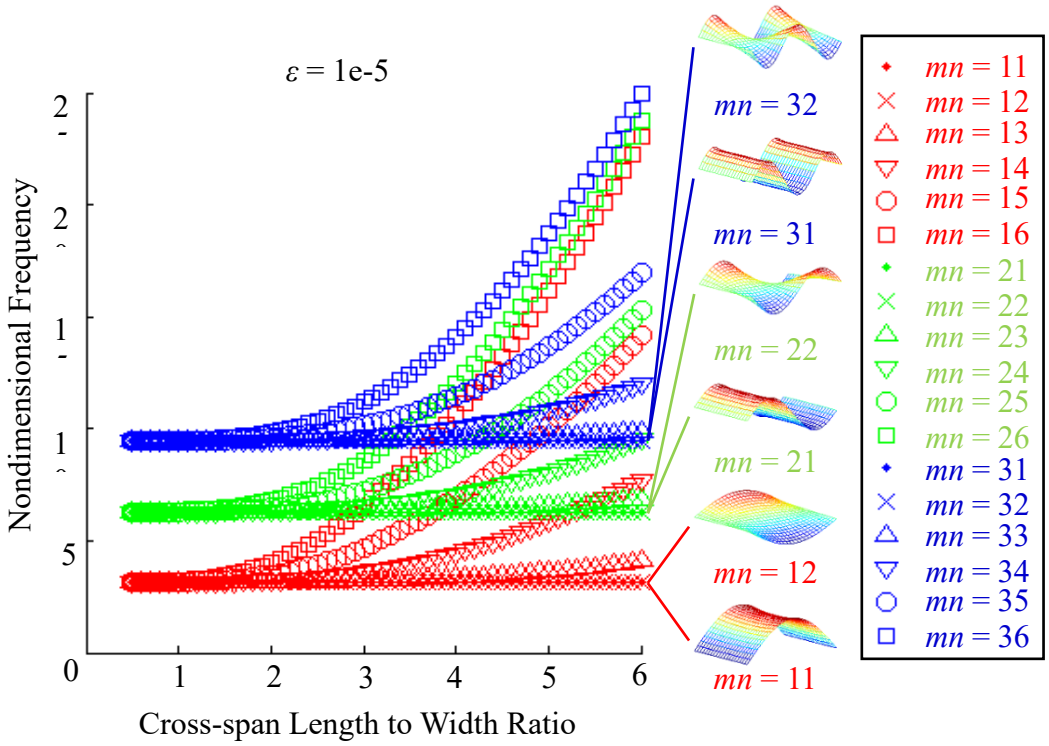

Figure 3.2. Frequency clustering of an *in vacuo*, stationary, uniformly tensioned web as a function of in-span length to width ratio κ, computed using the exact solution to the *in vacuo* eigenvalue problem Eq. (3.27) with $\varepsilon = 10^{-5}$.

The *in vacuo* mode frequencies are clustered tightly about the equivalent frequencies of a tensioned string and are not easy to distinguish either by varying the bending stiffness to tension ratio ε (usually very small but finite, see in reference [11]) or web in-span length to width ratio κ (as shown in Figure 3.2). As shown in Figure 3.2, all mode frequencies with the same m cluster close together when κ is small. The mode frequencies separate when κ increases, however the lowest symmetric and anti-symmetric mode frequencies (*i.e.* $n=1,2$) with the same m remain tightly clustered.

3.2.3 Discretized System Analysis of Coupled Eigenvalue Problem

In the presence of air-coupling ($\Lambda \neq 0$), analytical solutions to the eigenvalue problem are not available. Rather, the discretized system (Eq. (3.19)) needs to be solved. We choose an admissible function basis (normalized as Eq. (3.18)) for an assumed AMM process as follows:

$$\begin{aligned} &W'_{mn}(x'_1,x'_3)=\sin(m\pi x'_1)Y'_{mn}(x'_3),\ Y'_{mn}(x'_3)=C'_{mn}(x'_3)^{n-1},\\ &C'_{m1}=\sqrt{2\kappa},C'_{m2}=\sqrt{24\kappa^3},C'_{m3}=\sqrt{160\kappa^5},C'_{m4}=\sqrt{896\kappa^7},\\ &C'_{m5}=\sqrt{4608\kappa^9},C'_{m6}=\sqrt{22528\kappa^{11}},C'_{m7}=\sqrt{106496\kappa^{13}},C'_{m8}=\sqrt{491520\kappa^{15}}. \end{aligned} \tag{3.28}$$

While the exact *in vacuo* eigenfunctions can also be used as a comparison function basis for this discretization, the exact *in vacuo* eigenfunctions depend on web material and aspect ratio. As our goal is to develop "Universal" hydrodynamic functions, the computational effort required to calculate the discretization basis for every web material and aspect ratio considered is substantial. Instead the use of a polynomial basis in the x_3 direction allows the same basis function to be used for the all web aspect ratios and materials used, thus substantially reducing the computational effort with little effect on the accuracy of prediction.

To solve for the corresponding aerodynamic potentials φ'_{mn2}, we apply ABAQUS [40], a 3D finite element solver, to Eqs. (3.8) and (3.15) with boundary conditions (3.12), (3.13), and (3.17). Figure 3.3 shows the admissible function basis $W'_{mn}(x'_1,x'_3)$, the corresponding 2D on-web air velocity potentials $\varphi'_{mn2}(x'_1,0^+,x'_3)$, and 3D air velocity potentials $\varphi'_{mn2}(x'_1,x'_2,x'_3)$ with cross-sections views. The infinite fluid boundary is truncated to an inner domain with higher mesh density and an outer domain with lower mesh density to reduce the computational cost. The inner

domain is a uniform cube and the outer domain is the volume between the inner domain and a larger cube containing the inner domain.

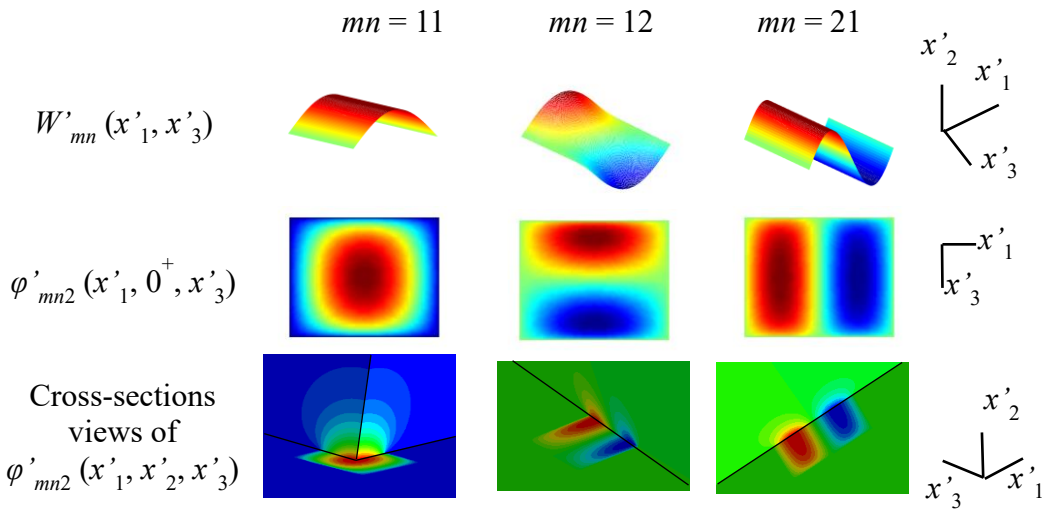

Figure 3.3. *In vacuo* admissible function bases $W'_{11} = \sqrt{2}\sin(\pi x'_1)$, $W'_{12} = \sqrt{24}\sin(\pi x'_1)x'_3$, and $W'_{21} = \sqrt{2}\sin(2\pi x'_1)$ for $\kappa = 1$, and the corresponding air velocity potentials on the web $\varphi'_{mn2}(x'_1, 0^+, x'_3)$, 3D air velocity potentials $\varphi'_{mn2}(x'_1, x'_2, x'_3)$ with cross-sections views. A 3D finite element solver is used to solve the corresponding air velocity potentials φ'_{mn2} from Eqs. (3.8) and (3.15) with boundary conditions (3.12), (3.13), and (3.17).

A convergence study determines the mesh density and size of each domain. We take $\kappa = 1$ for the study and use basis functions $W'_{11}, W'_{12}, W'_{13}, W'_{14}$ to check all diagonal entries in $\mathbf{M}'_{air}$, as discussed in Section 3.2.1. We first fix the inner and outer domain cubic side lengths to be one time and two times of the largest dimension of the web, respectively. Then, the mesh density convergence is determined when the diagonal entries in $\mathbf{M}'_{air}$ change by less than 1% in progressive computations where the mesh density is doubled in each computation. With mesh density converged, we increase the cubic domain side length by twice the largest dimension of the web in progressive computations until the diagonal entries in $\mathbf{M}'_{air}$ changes by less than 1%. Based on the convergence study, we use 512,000 elements with 531,441 nodes in the inner domain cube of side length equaling twice the largest dimension of the web; and we use 3,250 elements with 4,016 nodes in the outer domain cube whose extent ranges from two times to six times of the

largest dimension of the web. After obtaining W'_{mn} and φ'_{mn2}, $(\mathbf{K}')_{ij;mn}$ and $\left(\mathbf{M}'_{air}\right)_{ij;mn}$ can be solved by numerical integration of Eqs. (3.20) and (3.21). Substituting $(\mathbf{K}')_{ij;mn}$ and $\left(\mathbf{M}'_{air}\right)_{ij;mn}$ into Eq. (3.19), we will obtain the air-coupled natural frequencies for the webs.

Using this approach, we compare in Table 3.1 the two lowest frequencies of an air-coupled web as predicted by (a) using a comparison function basis, the exact *in vavuo* eigenfunctions and (b) using the polynomial admissible function basis in Eq. (3.28) for a web with parameters chosen as $\varepsilon = 1.6\times10^{-5}, \Lambda = 5.7, \kappa = 2.5$. We increase the sizes of $\mathbf{M}'$ and $\mathbf{K}'$ matrices from 1×1 to 4×4. The polynomial admissible function basis approximates well both two lowest frequencies of air-coupled web with less than 6% error compared to when the *in vacuo* eigenfunctions are used as a basis.

Table 3.1. The two lowest frequencies solved by AMM with exact *in vacuo* eigenfunctions and estimated admissible polynomial function basis (Eq. (3.28)), $\varepsilon = 1.6\times10^{-5}, \Lambda = 5.7, \kappa = 2.5$.

Sizes of $\mathbf{M}'$ and $\mathbf{K}'$	ω'_{11}		ω'_{12}	
	In vacuo eigenfunctions	Admissible function basis	*In vacuo* eigenfunctions	Admissible function basis
In vacuo	3.14182	3.14184	3.14445	3.14445
1×1	2.00485	2.00018	2.49805	2.49914
2×2	1.83017	1.93806	2.42958	2.45271
3×3	1.82556	1.93691	2.42904	2.42984
4×4	1.82426	1.93690	2.42901	2.42902

The computational approach above, which has also been described in prior works (see in reference [11]), has some disadvantages: (a) it is computationally expensive, (b) it requires a new computation for every aspect ratio and web material properties, (c) it requires expertise in fluid-structure interaction computations, and (d) has not been validated experimentally. In what follows we present an approach to overcome these disadvantages using hydrodynamic functions and validate it in experiments.

3.2.4 Hydrodynamic Function

Here we develop closed-form, semi-analytical, hydrodynamic functions for the first symmetric and anti-symmetric basis functions of the pre-tensioned web as a way to estimate the air-coupling on the lowest two eigenmodes of tensioned webs. The method outlined can be easily extended to compute hydrodynamic functions for other basis functions.

With the basis in place, we solve the air velocity potentials with different aspect ratios. So that we can use a same integration domain for different κ's , we rescale the coordinates $x_1^* = x_1', x_3^* = \kappa x_3'$; all the properties with $\kappa = 1$ are denoted with *. The hydrodynamic functions then are a multiplicative functions that depend on κ's that allow the added air mass entries computed for any aspect ratio to be expressed in terms of the "reference" added air mass entries when $\kappa = 1$. Thus, we have

$$\left(\mathbf{M}_{air}\right)_{ij;mn} = L\left(\mathbf{M}'_{air}\right)_{ij;mn} = LF_{ijmn2}(\kappa)\left(\mathbf{M}^*_{air}\right)_{ij;mn}, \qquad F_{ijmn2}(1) = 1. \tag{3.29}$$

$F_{ijmn2}(\kappa)$'s are functions relating the magnitudes of $\left(\mathbf{M}'_{air}\right)_{ij;mn}$ with respect to web aspect ratio for different basis functions W_{ij}' and different air velocity potentials on the surface of web $\varphi'_{mn2}(x'_1, 0^+, x'_3)$. Specifically, we use the basis functions $(m,1)$ and $(m,2)$ in Eq. (3.28) to fit $F_{11112}(\kappa)$ and $F_{12122}(\kappa)$, the hydrodynamic functions for the lowest symmetric and anti-symmetric basis functions. They are fitted to computed values with κ from 0.1 to 10 using a functional form in terms of a polynomial in terms of $\log_{10}(\kappa)$ along the lines of Sader's hydrodynamic functions [33,34], since it will balance the fitting range for both $\kappa > 1$ and $\kappa < 1$. The fitted hydrodynamic functions are determined to be:

$$\begin{aligned}
&F_{11112}(\kappa) = 1 - 1.17557[\log_{10}(\kappa)] - 0.10578[\log_{10}(\kappa)]^2 + 0.54019[\log_{10}(\kappa)]^3 \\
&+0.16507[\log_{10}(\kappa)]^4 - 0.25226[\log_{10}(\kappa)]^5 - 0.00822[\log_{10}(\kappa)]^6; \\
&F_{12122}(\kappa) = 1 - 1.91774[\log_{10}(\kappa)] + 1.16202[\log_{10}(\kappa)]^2 + 0.46179[\log_{10}(\kappa)]^3 \\
&-0.82329[\log_{10}(\kappa)]^4 - 0.19040[\log_{10}(\kappa)]^5 + 0.38791[\log_{10}(\kappa)]^6.
\end{aligned} \tag{3.30}$$

Figure 3.4 shows a comparison of nondimensional added mass from finite element method and fitted functions with admissible function basis $W_{11}' = \sqrt{2\kappa}\sin(\pi x_1')$, and $W_{12}' = \sqrt{24\kappa^3}\sin(\pi x_1')x_3'$. As can be seen, in the fitting range the maximum absolute related errors

between the semi-analytical hydrodynamic functions (*i.e.*, Eq. (3.30)) and the finite element computed solutions are 0.197% and 0.644% for $ij = mn = 11$ and $ij = mn = 12$, respectively.

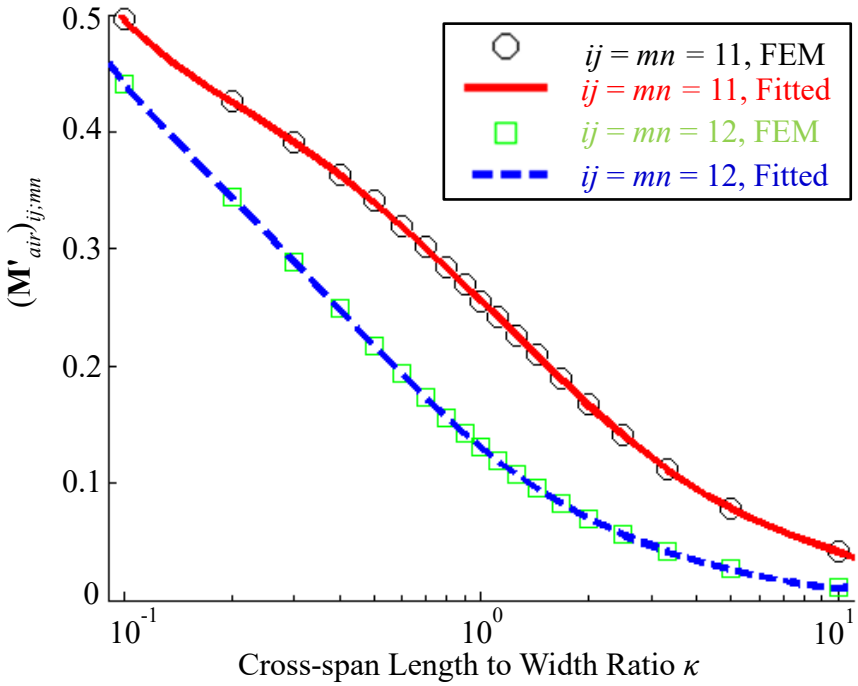

Figure 3.4. Comparison of nondimensional added mass from finite element method and fitted functions with admissible function basis $W'_{11} = \sqrt{2\kappa}\sin(\pi x'_1)$, and $W'_{12} = \sqrt{24\kappa^3}\sin(\pi x'_1)x'_3$, with κ from 0.1 to 10. The maximum absolute related errors for fitting $ij = mn = 11$ and $ij = mn = 12$ are 0.197% and 0.644%, respectively.

With the 1 term approximation the lowest symmetric and anti-symmetric frequencies of an air-coupled web can be determined using the hydrodynamic function as follows

$$(f_{air})_{11} = \frac{(\omega_{air})_{11}}{2\pi} = \frac{1}{2}\sqrt{\frac{\frac{D}{L^4}\pi^2 + \frac{N_{11}}{L^2}}{\rho_{web} + 0.51048\rho_{air}LF_{11112}(\kappa)}}\,(Hz),$$
$$(f_{air})_{12} = \frac{(\omega_{air})_{12}}{2\pi} = \frac{1}{2}\sqrt{\frac{\frac{D}{L^4}[\pi^2 + 24(1-\upsilon)\kappa^2] + \frac{N_{11}}{L^2}}{\rho_{web} + 0.26150\rho_{air}LF_{12122}(\kappa)}}\,(Hz). \qquad (3.31)$$

Recall since $\varepsilon = \dfrac{D}{L^2 N_{11}}$ is very small for industrial flexible electronics applications, typically from 10^{-6} to 10^{-4}, we can simplify Eq. (3.31) as

$$\begin{aligned} \left(f_{air}\right)_{11} &= \frac{\left(\omega_{air}\right)_{11}}{2\pi} \approx \frac{1}{2L}\sqrt{\frac{N_{11}}{\rho_{web}+0.51048\rho_{air}LF_{11112}(\kappa)}}\left(Hz\right), \\ \left(f_{air}\right)_{12} &= \frac{\left(\omega_{air}\right)_{12}}{2\pi} \approx \frac{1}{2L}\sqrt{\frac{N_{11}}{\rho_{web}+0.26150\rho_{air}LF_{12122}(\kappa)}}\left(Hz\right). \end{aligned} \tag{3.32}$$

Thus, R2R web designers and R2R system dynamics and control researchers only need to substitute physical properties into Eq. (3.32) to find the mode frequencies. These hydrodynamic functions can be used for a broad range of in-span length to width ratios from 0.1 to 10.

The analysis above assumes no air-coupling between different basis functions in the mass matrix. However, in principle different basis functions couple due to the off-diagonal terms in the added air mass matrix $\mathbf{M}'_{air}$. Although there is no closed-form solution for the correct eigenmodes, they can be calculated computationally.

We use AMM to estimate the mode shapes for air-coupled webs. We return to Eq. (3.19) and rewrite as $\mathbf{M}'\ddot{\mathbf{q}}' + \mathbf{K}'\mathbf{q}' = 0$, the corresponding eigenvectors of the matrix $\left(\mathbf{M}'\right)^{-1}\mathbf{K}'$ determine the contribution of each basis function to the air-coupled eigenmodes. This is discussed later in more detail in the context of the experimental measurements in Section 3.4.

In what follows we study the use of these hydrodynamic functions in the analysis of web vibration characteristics. Figure 3.5 shows the ratios of air-coupled to *in vacuo* mode frequencies computed using Eq. (3.32) for the lowest symmetric and anti-symmetric modes for three materials as a function of in-span length to width ratio. All these webs are with fixed width = 215.9 mm and pre-tension $N_{11} = 200N/m$, in the typical range of industrial usage [41-43], with related web areal mass densities as $\rho_{web} = 116.01g/m^2$, $71.55g/m^2$, and $42.58g/m^2$, air density $\rho_{air} = 1.225kg/m^3$ [10]. From Figure 3.5 we can see that air-coupling reduces the lowest natural frequencies from 20% to 60% compared to the *in vacuo* values in the range we investigated. Air-coupling effect on web natural frequencies is more pronounced for webs with large in-span length to width ratio and for webs with lower areal mass density. The latter observation is in line with Eq. (3.7) which suggests that air-coupling is modulated by the magnitude of $\Lambda = \dfrac{L\rho_{air}}{\rho_{web}}$, which implies

that lighter webs (low areal mass density) are more sensitive to air-coupling than heavier webs. Air-coupling also separates the clustered frequencies since the mode frequency of lowest symmetric mode reduces more than that of lowest anti-symmetric mode.

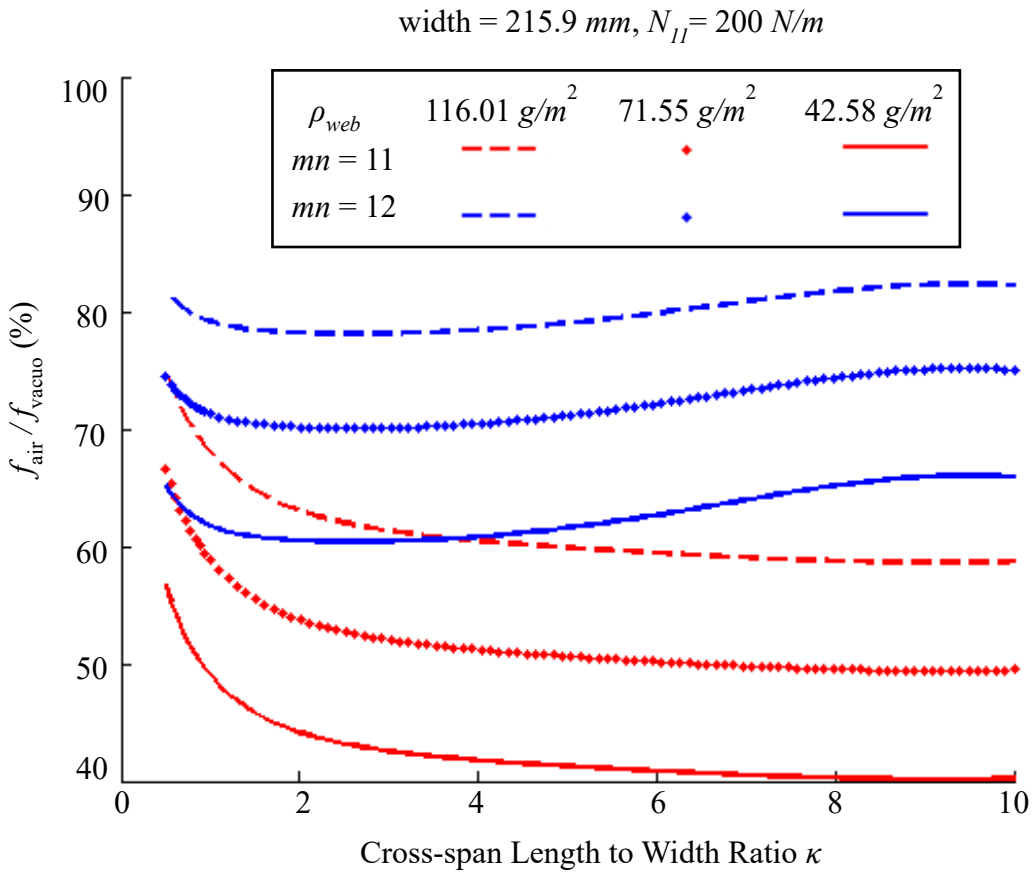

Figure 3.5. The ratios of estimated air-coupled to the exact *in vacuo* mode frequencies for the lowest symmetric and anti-symmetric modes for three materials as a function of in-span length to width ratio, using Eq. (3.32). All the three types of web are with width = 215.9 *mm*, $N_{11} = 200 N/m$. While their areal mass densities are $\rho_{web} = 116.01 g/m^2$, $71.55 g/m^2$, and $42.58 g/m^2$, referring to Table 3.2.

Table 3.2. Properties of the webs

Property	DuPont Nomex 410 Paper		Polyimide Film	Unit
Young's Modulus [a]	2.75	2.75	2.50	GPa
Poisson's Ratio [a]	0.30	0.30	0.34	–
Web Areal Density [b]	42.58 ± 0.653	116.01 ± 2.024	71.55 ± 0.676	g / m^2
Thickness	50.8	127.0	50.8	μm
Width	215.9	215.9	215.9	mm
In-span Length to Width Ratios	1.5:1, 2:1, 2.5:1, and 3:1			–

a *Given in* [43,44].

b *Measured by averaging the weights of six area-known rectangular films. Means and stand deviation values are listed.*

3.3 Experimental Setup

To experimentally validate the hydrodynamic functions, we use acoustically excited and laser-measured web vibrations with three different types of web materials with various in-span length to width ratios and pre-tensions. We conduct tests on rectangular webs with geometric dimensions and material properties given in Table 3.2. Each web is wrapped onto four live rollers (Hex-axls 1.9" diameter conveyor rollers with bearing-in, McMaster-Carr) which are mounted on an aluminum frame via brackets (Conveyor roller mounting brackets for hex axle, McMaster-Carr) as shown in Figure 3.6(a). The aluminum frame is built with $25.4mm \times 25.4mm$ framing rails (T-Slotted Framing Rails, McMaster-Carr) and fastened by associated fasteners and brackets (McMaster-Carr). Two rollers in intermediate height are used for adjusting κ. We load in-span tension to the web by hanging a weight-known dumbbell on one end of web wrapping over the lowest roller. A small portion of web is wrapped on the dumbbell bar and taped uniformly afterwards. The other end of web is wound onto the small upper roller which has a pin hole for rotation lockage. Pre-tensions in our experiments are $111.64N/m$ and $163.33N/m$. These values are industrially relevant [41-43]. Due to the frictional interactions with the rollers, low pre-tension cannot stretch the web evenly and high pre-tension can lead to wrinkles. We mount a speaker (5Watts, Creative A220, Creative Technology Ltd.) on a boom stand which is separated from the aluminum frame for vibration isolation and place it close to one free edge of the web as Figure 3.6 shows. We measure frequency response function (FRF) of the speaker before we use it as the excitation source. Swept sine waves are sent to the speaker from Dynamics Signal Analyzer (DSA) (HP 35670A, The Keysight Technologies, Inc) with increment of 0.1 Hz. The speaker cone

displacement is sensed by a laser-based triangulation measurement system (Microtrak 7000, MTI Instruments) whose sensor head is fixed to a tripod for non-contact measurement. The cone displacement to the input voltage ratio is found fairly constant in the frequency range up to 100Hz and phase response drops from 0° smoothly. We measure FRFs of 15 points for $\kappa = 1.5$, and $\kappa = 2$, and 25 points for $\kappa = 2.5$, and $\kappa = 3$ where these points are equally distributed in the $x_1 - x_3$ plane as shown in Figure 3.6(b). We choose the swept upper cutoff frequency to be slightly higher than the estimated frequencies $\left(f_{air} \right)_{12}$ and the lower cutoff frequency to be lower than the first resonant frequency for time saving. We average the frequencies from FRFs of these points to attain web measured resonant frequencies. The associated mode shapes are approximated subsequently by fitting the amplitudes of these measured points at the resonant frequencies. We fit the measured mode shapes to obtain smooth surfaces as

$$W_{1n}^{(measured)}(x_1, x_3) = \sin(\pi x_1 / \mathrm{L})(a_1 + a_2 x_3 + a_3 x_3^2 + a_4 x_3^3 + a_5 x_3^4), \tag{3.33}$$

where $a_1, a_2, a_3, a_4,$ and a_5 are multiplicative constants.

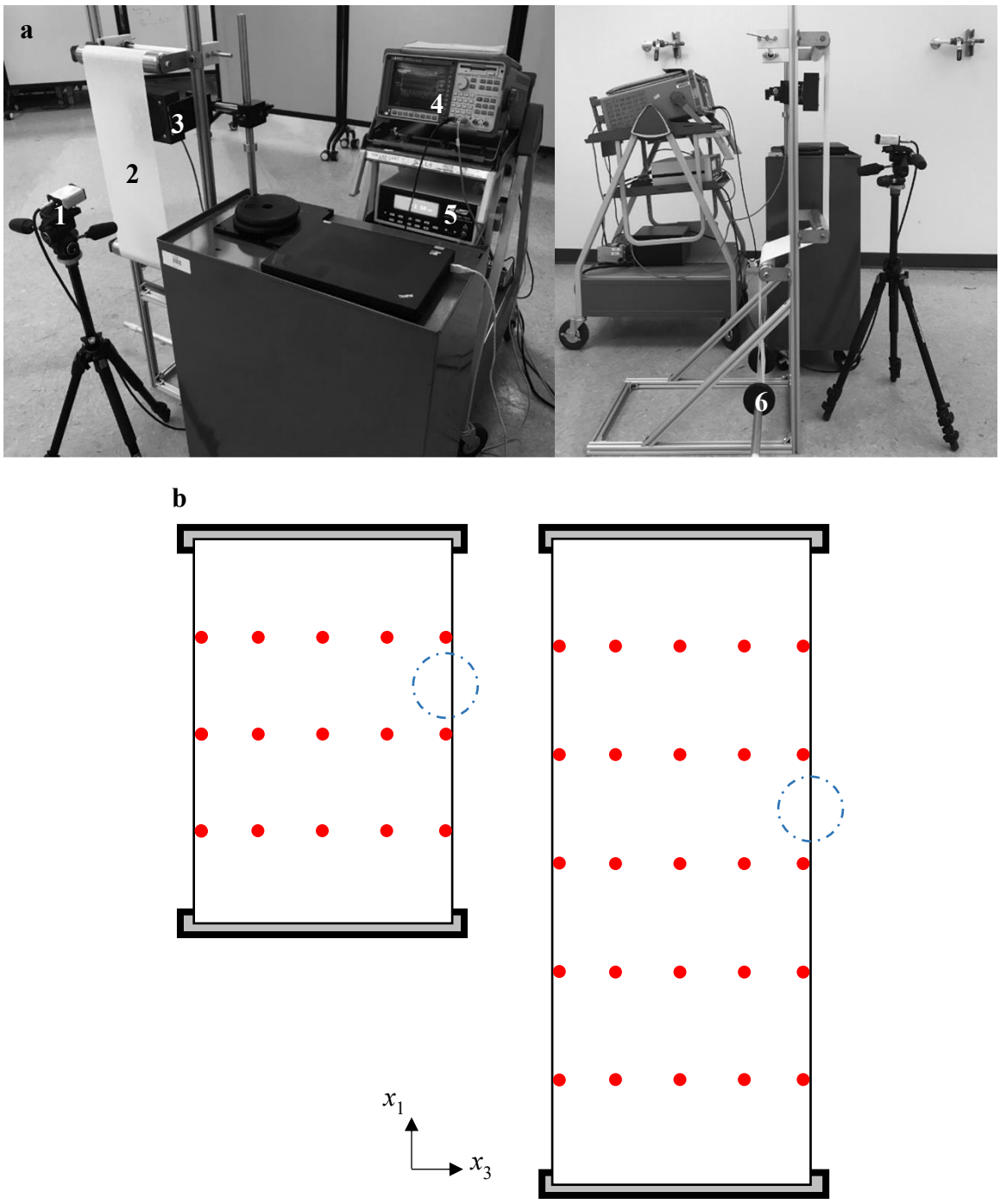

Figure 3.6. (a) Experimental setup: 1 sensor head, 2 web, 3 loudspeaker, 4 dynamic signal analyzer, 5 laser-based triangulation system controller, and 6 deadweight (dumbbell); (b) measurement grid on the web (left for $\kappa = 1.5,$ and $\kappa = 2$, right for $\kappa = 2.5,$ and $\kappa = 3$, each red dot denotes the measured point).

3.4 Results and Discussions

We experimentally validate the hydrodynamic functions through their effects on both the natural frequencies and mode shapes. As an example, Figure 3.7 shows one FRF gain and phase plots of a 127 μm DuPont Nomex 410 Paper with $\kappa = 2.5,$ and pre-tension $N_{11} = 111.64\ N/m$ excited acoustically by the speaker described earlier. Two amplitude peaks are distinct at resonant frequencies, 17.6 Hz and 22.4 Hz, and nearly 180 degrees phase across the peaks. The FRF gain and phase plots of other scenarios are very similar and not presented here; rather, the measured resonance frequencies from those measurements are recorded.

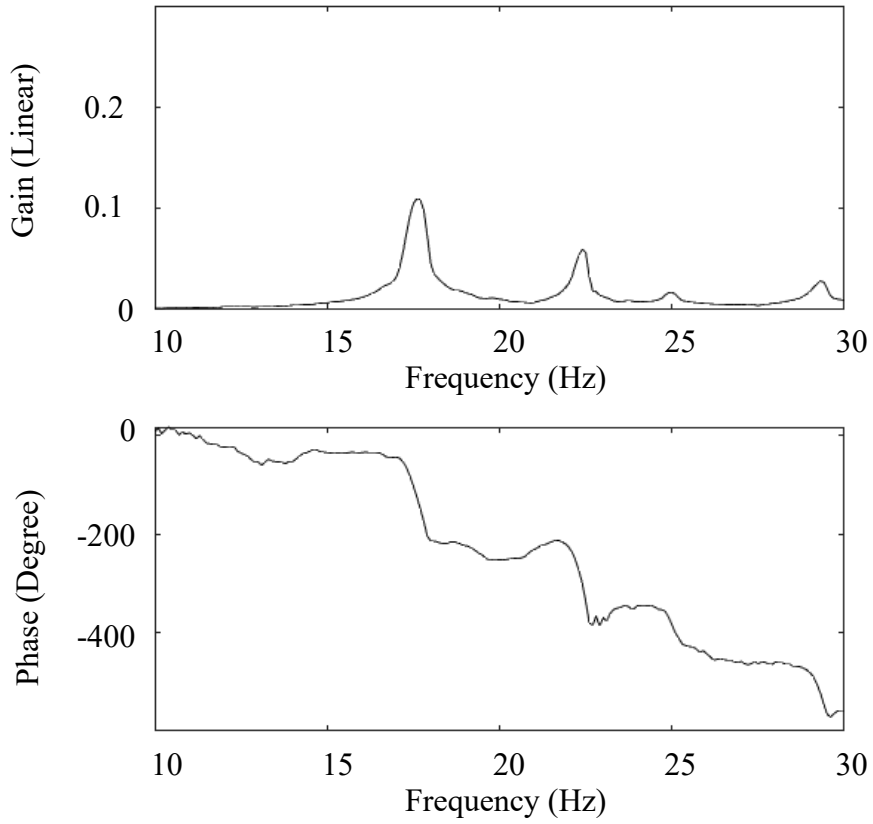

Figure 3.7. Averaged gain and phase of frequency response function of 127 μm DuPont Nomex 410 Paper with $\kappa = 2.5,$ and pre-tension $N_{11} = 111.64 N/m$.

Tables 3.3-3.5 present comparisons between the estimated frequencies by Eq. (3.32) and the measured resonant frequencies of the 50.8μm DuPont Nomex 410 Paper, the 127μm DuPont Nomex 410 Paper, and the 50.8μm DuPont polyimide film under two pre-tensions and four in-

span length to width ratios, respectively. The hydrodynamic functions allow the prediction of the first two web vibration frequencies to within 10% across all the measurements. Factors contributing to the discrepancies can be categorized into two aspects: web material anisotropy, non-uniform distribution of pre-tension, initial out-of-flatness of web, that are all effects not included in the mathematical model; and measurement, fitting, and parameter value uncertainties. For example, a 1% variation of air density, a one-σ variance of web areal mass density in Table 3.2 and a 2% fitting error in $F_{mn2}(\kappa)$ can cause up to 1.2% difference calculated by error propagation function,

$$\Delta\left(f_{air}\right)_{mn}=\sqrt{\left(\frac{\partial\left(f_{air}\right)_{mn}}{\partial\rho_{web}}\Delta\rho_{web}\right)^2+\left(\frac{\partial\left(f_{air}\right)_{mn}}{\partial\rho_{air}}\Delta\rho_{air}\right)^2+\left(\frac{\partial\left(f_{air}\right)_{mn}}{\partial F_{mn2}(\kappa)}\Delta F_{mn2}(\kappa)\right)^2}\ (Hz), \quad (3.34)$$

where Δ denotes the variation of a variable. The assumption of uniform pre-tension is also often hart to ensure in practice. Misalignment of rollers, friction characteristics between web and roller, anisotropic and inhomogeneous web material, residual stress in the web, and non-uniformity in applied pre-tension often produce in-plane strain energy variations crossing the web span.

Table 3.3. The estimated and measured resonant frequencies for $50.8\mu m$ DuPont Nomex 410 paper, $\rho_{web}=42.58g/m^2$

	$\left(f_{air}\right)_{11}$ (Hz)			$\left(f_{air}\right)_{12}$ (Hz)		
Pre-tension $N_{11}=111.64N/m$						
κ	Estimation	Experiment	Discrepancy	Estimation	Experiment	Discrepancy
1.5/1	36.20	33.10	8.55%	48.06	45.34	5.66%
2/1	26.17	24.35	6.94%	35.86	34.22	4.58%
2.5/1	20.47	18.78	8.27%	28.65	28.17	1.66%
3/1	16.81	15.39	8.47%	23.88	23.08	3.37%
Pre-tension $N_{11}=163.33N/m$						
1.5/1	43.78	40.11	8.38%	58.13	55.22	5.01%
2/1	31.65	29.44	6.98%	43.38	39.31	9.37%
2.5/1	24.76	22.44	9.38%	34.65	32.79	5.36%
3/1	20.34	19.26	5.29%	28.89	26.10	9.65%

Table 3.4. The estimated and measured resonant frequencies for $50.8\mu m$ DuPont Polyimide film, $\rho_{web} = 71.55 g/m^2$

	$(f_{air})_{11}$ (Hz)			$(f_{air})_{12}$ (Hz)		
Pre-tension $N_{11} = 111.64 N/m$						
κ	Estimation	Experiment	Discrepancy	Estimation	Experiment	Discrepancy
1.5/1	33.86	32.47	4.11%	42.96	42.02	2.19%
2/1	24.59	24.35	0.97%	32.09	29.76	7.26%
2.5/1	19.29	18.94	1.80%	25.64	24.67	3.79%
3/1	15.87	15.87	0.00%	21.38	19.58	8.40%
Pre-tension $N_{11} = 163.33 N/m$						
1.5/1	40.96	38.83	5.19%	51.97	49.02	5.67%
2/1	29.74	29.28	1.55%	38.81	37.56	3.23%
2.5/1	23.33	21.49	7.88%	31.01	30.08	3.01%
3/1	19.19	17.67	7.92%	25.86	24.35	5.82%

Table 3.5. The estimated and measured resonant frequencies for $127\mu m$ DuPont Nomex 410 paper, $\rho_{web} = 116.01 g/m^2$

	$(f_{air})_{11}$ (Hz)			$(f_{air})_{12}$ (Hz)		
Pre-tension $N_{11} = 111.64 N/m$						
κ	Estimation	Experiment	Discrepancy	Estimation	Experiment	Discrepancy
1.5/1	31.02	29.60	4.58%	37.56	37.56	0.00%
2/1	22.64	21.80	3.71%	28.08	27.85	0.82%
2.5/1	17.81	17.51	1.69%	22.44	22.28	0.73%
3/1	14.68	14.55	0.88%	18.71	18.62	0.48%
Pre-tension $N_{11} = 163.33 N/m$						
1.5/1	37.52	35.17	6.26%	45.43	43.13	5.06%
2/1	27.38	26.10	4.69%	33.97	33.10	2.55%
2.5/1	21.54	19.75	8.32%	27.15	26.10	3.86%
3/1	17.75	17.67	0.48%	22.63	21.18	6.41%

As seen in the experimental results, the air loading significantly changes both the natural frequencies and the mode shapes of the measured webs. Figure 3.8 illustrates the lowest symmetric and anti-symmetric experimental mode shapes for the associated resonant frequencies in Figure 3.7. Figures 3.8 a) to d) show the exact mode shapes, with a) and b) for the *in vacuo* case. In-air-coupled eigenmodes are computed using the AMM described in Section 2.2.1. Table 3.6 shows a convergence study of the order required in AMM. The computed in-air eigenmodes are shown in Figures 3.8 c) and d). We plot the mode shapes with 93×38 (3,534) nodes.

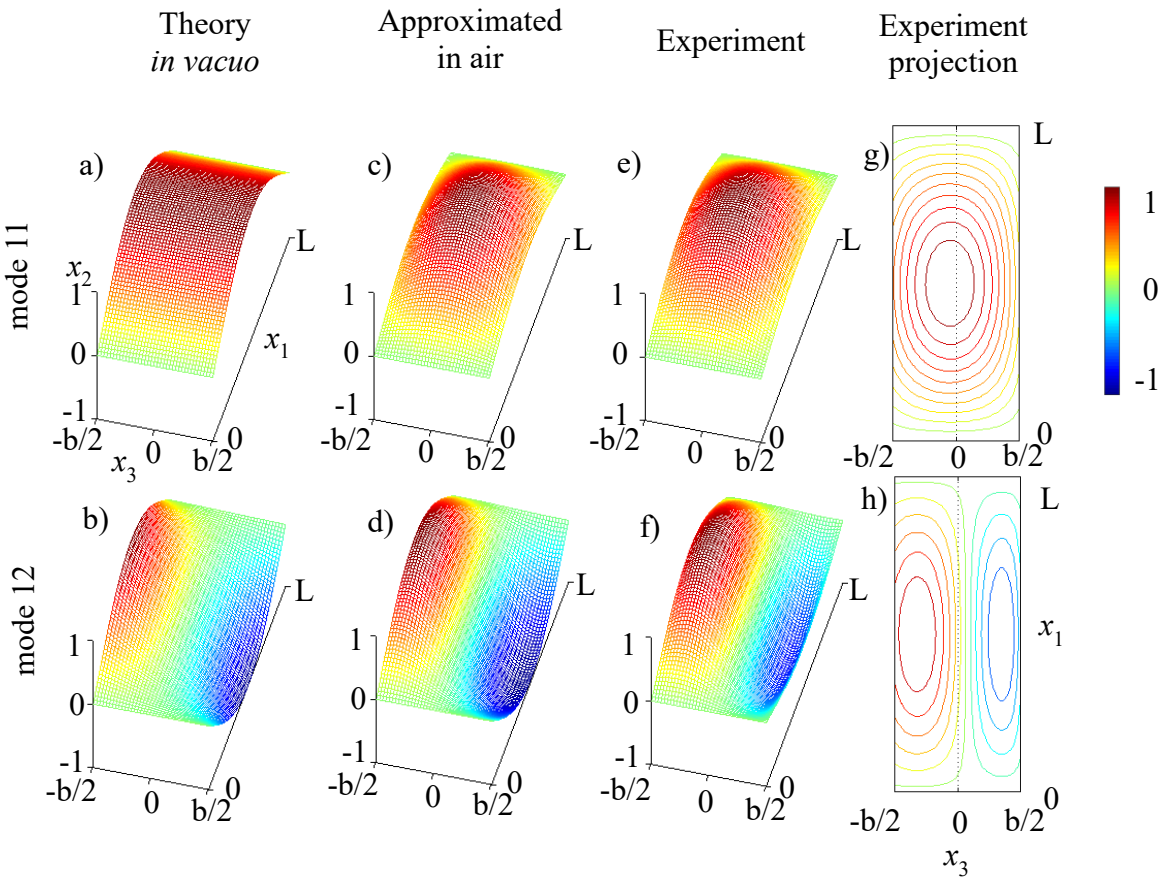

Figure 3.8. Three-dimensional representations of amplitude-normalized mode shapes of 127 μm DuPont Nomex 410 Paper with $\kappa = 2.5$, and pre-tension $N_{11} = 111.64 N/m$. a), c), and e) are the mode shapes for lowest symmetric mode; b), d), and f) are the mode shapes for lowest anti-symmetric mode. a) and b) are the *in vacuo* mode shapes from theoretically predictions; c) and d) are mode shapes of the case of a web surrounded by air by potential flow theory; e) and f) are the in air mode shapes fitted from experimental measured points by Eq. (3.33); g) and h) are the projections of e) and f) to the plane of the web (x_1-x_3 plane). The L-2 norm between c) and e) is 2.98; the L-2 norm between d) and f) is 10.56.

Table 3.6. L-2 norm of mode shapes from different AMM orders, 3,534 points, 127 μm DuPont Nomex 410 Paper with $\kappa = 2.5$, and pre-tension $N_{11} = 111.64 N/m$

AMM order *n*	in air mode shape 11 (approximated with symmetric *in vacuo* basis functions)	in air mode shape 12 (approximated with anti-symmetric *in vacuo* basis functions)
n = 1	41.96	24.83
n = 2	34.69	32.23
n = 3	34.00	31.56

The following are the key observations in comparing the computed and experimental in-air eigenmodes:

1. The experimental and predicted in-air eigenmodes clearly couple the basis functions. The corresponding *in vacuo* eigenmodes contribute the major characteristic to the in-air eigenmodes, but the effects of other coupled basis functions reduce the amplitude at the free edges. The off-diagonal terms in the added air mass matrix cause the coupling.
2. The AMM with three basis functions is able to closely predict the measured mode shapes. For symmetric case, the L-2 norms for the computed and experimental in air modes are 34.00 and 33.99 respectively; for the anti-symmetric case, the L-2 norms for the computed and experimental in air modes are 31.56 and 29.13 respectively.
3. The experimentally measured modeshapes are slightly asymmetric about the $x_3 = 0$ axis. The asymmetry in the contour plots of mode shapes shown in Figures 3.8 g) and h) indicate non-uniform distribution of pre-tension exists in the experiments. Because of the misalignment of rollers, friction characteristics between web and roller, anisotropic and inhomogeneous web material, the distributed pre-tension is always slightly non-uniform. The mode shapes of other scenarios are similar to these in Figure 3.8 in terms of web in-span deformation, thus they are not repetitively provided in this chapter.

3.5 Conclusions

Accurate prediction of transverse web vibrations in R2R manufacturing for flexible hybrid electronics and stretchable electronics can help improve process control and stability. We study in detail the discretized models of uniaxially tensioned Kirchoff plates surrounded by three-dimensional potential flow for different aspect ratios and web materials commonly used in flexible electronics manufacturing. We derive closed-form, semi-analytical hydrodynamic functions for the lowest two frequencies that are valid for arbitrary material and aspect ratio used in R2R processes. We experimentally validated both the predicted web frequencies from hydrodynamic functions and the corresponding mode shapes from potential flow theory using pointwise laser measurements of acoustically excited webs with different pre-tensions, web materials, and aspect ratios. The main results are as follows:

1. The hydrodynamic functions allow the prediction of the symmetric and anti-symmetric mode frequencies to within 10% across all the measurements. They provide R2R process designers a convenient way to predict the lowest frequencies of air-coupled web systems without need to resort to computationally intensive methods.
2. Based on computations, air-coupling reduces the lowest symmetric and anti-symmetric mode frequencies of webs from 20% to 60% compared to the *in vacuo* values in the range we investigated and separates the clustered frequencies.
3. Air-coupling changes the eigenmodes of webs by cross coupling various *in vacuo* modes. These are caused by the off-diagonal terms in the added air mass matrix.
4. The lowest symmetric and anti-symmetric mode frequencies using hydrodynamic functions are experimentally validated with 3 different materials (2 DuPont Nomex 410 Papers with different thickness, 1 Polyimide Film), 2 different pre-tensions, and four different aspect ratios representing materials, tensions, and aspect ratios commonly found in R2R flexible electronics manufacturing.
5. The lowest symmetric and anti-symmetric mode shapes are experimentally validated. The differences between L-2 norms for the computed and experimental in air modes are 0.03% for symmetric case and 7.70% for the anti-symmetric case.

We expect that the semi-analytical solutions to air-coupled web vibrations will find use among web system designers who are interested in avoiding the detrimental effects of web vibration on process quality and stability in R2R flexible electronics lines and / or in innovations that might exploit web vibrations for value added processes.

3.6 References

[1] Siegel, D., & Shivakumar, S. (Eds.). (2014). *The Flexible Electronics Opportunity*. National Academies Press.

[2] Cao, Q., Kim, H. S., Pimparkar, N., Kulkarni, J. P., Wang, C., Shim, M., ... & Rogers, J. A. (2008). Medium-scale carbon nanotube thin-film integrated circuits on flexible plastic substrates. *Nature*, *454*(7203), 495-500.

[3] Krebs, F. C., Tromholt, T., & Jørgensen, M. (2010). Upscaling of polymer solar cell fabrication using full roll-to-roll processing. *Nanoscale*, *2*(6), 873-886.

[4] Sekitani, T., Zschieschang, U., Klauk, H., & Someya, T. (2010). Flexible organic transistors and circuits with extreme bending stability. *Nature materials*, *9*(12), 1015-1022.

[5] Webb, R. C., Bonifas, A. P., Behnaz, A., Zhang, Y., Yu, K. J., Cheng, H., ... & Rogers, J. A. (2013). Ultrathin conformal devices for precise and continuous thermal characterization of human skin. *Nature materials*, *12*(10), 938-944.

[6] Palavesam, N., Marin, S., Hemmetzberger, D., Landesberger, C., Bock, K., & Kutter, C. (2018). Roll-to-roll processing of film substrates for hybrid integrated flexible electronics. *Flexible and Printed Electronics*, *3*(1), 014002.

[7] Cooper, K. P. (2019, May). Advanced and nano manufacturing research at NSF. In *Micro-and Nanotechnology Sensors, Systems, and Applications XI* (Vol. 10982, p. 1098213). International Society for Optics and Photonics.

[8] Lu, Y., & Pagilla, P. R. (2014). Modeling of temperature distribution in moving webs in roll-to-roll manufacturing. *Journal of Thermal Science and Engineering Applications*, *6*(4).

[9] Feng, D., & Raman, A. (2019). Thermomechanics of axially moving webs in roll-to-roll manufacturing processes. *International Journal of Heat and Mass Transfer*, *129*, 1317-1327.

[10] Raman, A., Wolf, K. D., & Hagedorn, P. (2000, June). Observations on the vibrations of paper webs. *11th Annual Symposium on Information Storage and Processing Systems*.

[11] Vaughan, M., & Raman, A. (2010). Aeroelastic stability of axially moving webs coupled to incompressible flows. *Journal of Applied Mechanics*, *77*(2).

[12] Nguyen, Q. C., & Hong, K. S. (2011). Transverse vibration control of axially moving membranes by regulation of axial velocity. *IEEE Transactions on Control Systems Technology*, *20*(4), 1124-1131.

[13] Subbaraman, H., Lin, X., Xu, X., Dodabalapur, A., Guo, L. J., & Chen, R. T. (2012, October). Metrology and instrumentation challenges with high-rate, roll-to-roll manufacturing of flexible electronic systems. In *Instrumentation, Metrology, and Standards for Nanomanufacturing, Optics, and Semiconductors VI* (Vol. 8466, p. 846603). International Society for Optics and Photonics.

[14] Kimbrough, B. (2015, September). In-line roll-to-roll metrology for flexible electronics. In *Applied Advanced Optical Metrology Solutions* (Vol. 9576, p. 957603). International Society for Optics and Photonics.

[15] Eum, S., Lee, J., & Nam, K. (2016, October). Robust tension control of roll to roll winding equipment based on a disturbance observer. In *IECON 2016-42nd Annual Conference of the IEEE Industrial Electronics Society* (pp. 625-630). IEEE.

[16] Ma, L., Chen, J., Tang, W., & Yin, Z. (2017). Transverse vibration and instability of axially travelling web subjected to non-homogeneous tension. *International Journal of Mechanical Sciences*, *133*, 752-758.

[17] Ma, L., Chen, J., Tang, W., & Yin, Z. (2017). Vibration-based estimation of tension for an axially travelling web in roll-to-roll manufacturing. *Measurement Science and Technology*, *29*(1), 015102.

[18] Ali, S., & Hawwa, M. A. (2019). A parametric study on the dynamics of two-span roll-to-roll microcontact printing system. *Sādhanā*, *44*(5), 1-11.

[19] Lee, J., Shin, K. H., & Kang, H. (2019). Design of a register controller considering inherent characteristics of a roll-to-roll continuous manufacturing system. *The International Journal of Advanced Manufacturing Technology*, *102*(9), 3725-3737.

[20] Dorrestijn, M., Bietsch, A., Açıkalın, T., Raman, A., Hegner, M., Meyer, E., & Gerber, C. (2007). Chladni figures revisited based on nanomechanics. *Physical review letters*, *98*(2), 026102.

[21] Vuillermet, G., Gires, P. Y., Casset, F., & Poulain, C. (2016). Chladni patterns in a liquid at microscale. *Physical review letters*, *116*(18), 184501.

[22] Shabaniverki, S., Thorud, S., & Juárez, J. J. (2018). Protocol for assembling micro-and nanoparticles in a viscous liquid above a vibrating plate. *MethodsX*, *5*, 1156-1165.

[23] Shabaniverki, S., Thorud, S., & Juarez, J. J. (2018). Vibrationally directed assembly of micro-and nanoparticle-polymer composites. *Chemical Engineering Science*, *192*, 1209-1217.

[24] Finn III, M., Martens, C. J., Zaretski, A. V., Roth, B., Søndergaard, R. R., Krebs, F. C., & Lipomi, D. J. (2018). Mechanical stability of roll-to-roll printed solar cells under cyclic bending and torsion. *Solar Energy Materials and Solar Cells*, *174*, 7-15.

[25] Niemi, J., & Pramila, A. (1987). FEM-analysis of transverse vibrations of an axially moving membrane immersed in ideal fluid. *International journal for numerical methods in engineering*, *24*(12), 2301-2313.

[26] Koivurova, H., & Pramila, A. (1997). Nonlinear vibration of axially moving membrane by finite element method. *Computational Mechanics*, *20*(6), 573-581.

[27] Chang, Y. B., & Moretti, P. M. (2002). Flow-induced vibration of free edges of thin films. *Journal of fluids and structures*, *16*(7), 989-1008.

[28] Hara, K., & Watanabe, M. (2013). Stability analysis of rectangular plates in incompressible flow with Fourier multiplier operators. In *ASME 2013 Pressure Vessels and Piping Conference*. American Society of Mechanical Engineers Digital Collection.

[29] Hara, K., & Watanabe, M. (2014, July). Formulation of the Aeroelastic Instability Problem of Rectangular Plates in Uniform Flow Based on the Hamiltonian Mechanics for the Constrained System. In *Pressure Vessels and Piping Conference* (Vol. 46018, p. V004T04A060). American Society of Mechanical Engineers.

[30] Yao, G., & Zhang, Y. M. (2016). Dynamics and stability of an axially moving plate interacting with surrounding airflow. *Meccanica*, *51*(9), 2111-2119.

[31] Kulachenko, A., Gradin, P., & Koivurova, H. (2007). Modelling the dynamical behaviour of a paper web. Part II. *Computers & Structures*, *85*(3-4), 148-157.

[32] Bidkar, R. A., Raman, A., & Bajaj, A. K. (2008). Aeroelastic stability of wide webs and narrow ribbons in cross flow. *Journal of applied mechanics*, *75*(4).

[33] Sader, J. E. (1998). Frequency response of cantilever beams immersed in viscous fluids with applications to the atomic force microscope. *Journal of applied physics*, *84*(1), 64-76.

[34] Green, C. P., & Sader, J. E. (2002). Torsional frequency response of cantilever beams immersed in viscous fluids with applications to the atomic force microscope. *Journal of applied physics*, *92*(10), 6262-6274.

[35] Chu, W. H. (1968). Vibrations of fully submerged cantilever plates in water. *South West Research Institute, San Antonio, Texas, Department of Mechanical Sciences, Published in: Schiffstechnik, Band 15, Heft 78*.

[36] Meyerhoff, W. K. (1970). Added masses of thin rectangular plates calculated from potential theory. *Journal of Ship Research*, *14*(02), 100-111.

[37] Yadykin, Y., Tenetov, V., & Levin, D. (2003). The added mass of a flexible plate oscillating in a fluid. *Journal of Fluids and Structures*, *17*(1), 115-123.

[38] Ulsoy, A. G., & Mote Jr, C. D. (1982). Vibration of wide band saw blades. *Journal of Engineering for Industry*, *104*(1), 71-78

[39] Turnbull, P. F., Perkins, N. C., & Schultz, W. W. (1995). Contact-induced nonlinearity in oscillating belts and webs. *Journal of Vibration and Control*, *1*(4), 459-479.

[40] ABAQUS 6.13 (2013) *Analysis User's Guide*. Dassault Systèmes Simulia Corp, Providence, RI.

[41] Applied Materials, Inc., Applied Smart Web. (2019, November 6). Retrieved from https://3.imimg.com/data3/LQ/YL/MY-956144/applied-smart-web.pdf

[42] TECNAU, Inc. (2019, November 6). Retrieved from https://www.tecnau.com/product/roll-20/

[43] Davis-Standard, LLC. (2019, November 6). Retrieved from https://davis-standard.com/DS_wordpress/wp-content/uploads/2018/04/EC_Overview_EN.pdf

[44] Dupont, Inc. (2019, November 6). Retrieved from https://www.dupont.com/content/dam/dupont/products-and-services/membranes-and-films/polyimde-films/documents/DEC-Kapton-summary-of-properties.pdf

[45] Dupont, Inc. (2019, November 6). Retrieved from https://www.dupont.com/content/dam/assets/products-and-services/electronic-electrical-materials/assets/DPT16_21668_Nomex_410_Tech_Data_Sheet_me03_REFERENCE.pdf

4. MEASURING NONUNIFORM WEB TENSION FOR ROLL-TO-ROLL MANUFACTURING OF FLEXIBLE AND PRINTED ELECTRONICS

4.1 Introduction

Thin film transistors [1-4], supercapacitors [5-8], organic light emitting diodes [9-12], solar cells [13-17], antennas [18, 19], and sensors [20-27] are applications where roll-to-roll (R2R) processes provide a low-cost and high-throughput scheme for large scale manufacturing of devices. The global market for R2R flexible devices is projected to double between 2018 and 2023 [28]. The main barrier in the scalability of R2R flexible electronics is low device yield rate in fabrication, which requires costly post-process product testing to control. Maximizing the yield rate requires cost-effective schemes in modeling and control of processes, in-line metrology, in-line characterization, and effective utilization of new materials [29].

Stresses in R2R fabricated flexible devices arise during manufacturing due to a combination of applied web tension and process-induced stresses [30,31] from printing (*i.e.* ink jetting, gravure, screen, and slot-die) [1-4, 8-27], chemical vapor deposition [5, 16], laser/ heat annealing [6, 7, 10], UV curing [11, 12, 18, 27], and /or hot embossing [27]. Such combined stresses are significant in R2R manufactured devices since the underlying substrates such as PET, PEN, and polyimide are already under tension, unlike in silicon wafers used for integrated circuit manufacturing. When the web is diced or cut to release the printed flexible devices, these stresses generate residual stresses. The performance of printed electronics devices can depend on residual stresses [32, 33]. Thus, nonuniform applied tension within the web which is caused by nonuniform friction between web and rollers, roller-web misalignment, and roller-roller misalignment can lead to nonuniform device performance crossing the width of web, or worse, to web wrinkling. Monitoring and correcting for nonuniform web tension are important considerations to understand the residual stresses, which can help in feedback quality control of R2R processes to maximize device yields.

There are different basic types of web tension measuring methods in literature. Instrumented rollers are the most common tension measurement tools in R2R industry. Koç *et al*. and Jeong *et al.* used tension sensors (load cells and dancer, respectively) with speed sensors to measure and control web tension with velocity in multiple spans under a uniform tension assumption [34, 35]. Schultheis invented a method with a pressure sensor wound on a roller to measure continuous web tension [36]. However, instrumented rollers methods need investment in customized rollers and

need re-calibration when the web path changes. Moreover, they assume that the tension in the web wrapped around the roller is unchanged by the friction. In addition, these sensors tend to drift and are sensitive to the environmental temperature and vibrations [37]. Several authors have used fundamental vibration frequency measurements to infer web tension; however, they did not consider non-uniform web tension and the effect of air loading [38-42]. Our previous works on vibrations of air-coupled web systems showed air effect significantly changes the frequencies and mode shapes of webs with typical tensions used by commercial R2R systems [43-45]. Scientists in VTT Information Technology developed a system to measure the nonuniform web tension using air film pressure [37]. This system only works for high web speed in air R2R processes and needs re-calibration when the web path changes. In addition, they assumed the cross-width web contact stiffness is uniform which, as we will demonstrate in this chapter, cannot occur in finite width systems even the tension is uniform. Jin et al. experimentally fitted web tension and the contact force under a fixed web deflection on the web [46]; however, this approach is specific to the exact web properties, web geometry, and roller configuration of their experiment, and needs recalibration for each specific web measured. Overall, comprehensive, accurate, reliable, and inexpensive methods for measuring nonuniform web tension in R2R processes are an unsolved problem.

In this chapter, we develop and test a non-contact resonance (NCR) method and a gentle contact stiffness mapping (GCSM) method for measuring average web tension and its linear variation. These methods can supplement the in-line metrology process of existing in air or *in vacuo* R2R systems, without the need for expensive instrumented rollers. Both methods can accurately measure web tension for a wide range of web properties, web path, web tension, measurement configurations, and environmental conditions. Both methods are based on first principles mechanics models of a tensioned plate. The NCR method includes the plate's interactions with a surrounding fluid. The methods are cross validated on a stationary test stand and the NCR method is used to study the web tension distribution within a commercial R2R system.

4.2 Modeling

We choose a 2D isotropic, linearly elastic, uniaxially tensioned, rectangular Kirchhoff plate model to simulate a single span in R2R systems as shown in Figure 4.1(a). To identify average web tension and the linear variation of tension, we present an NCR method which can distinguish

the lowest symmetric and antisymmetric resonance frequencies and a GCSM method with accurate web contact stiffness profile. There is no tension applied in the cross-span direction, thus we use a tensioned plate model instead of a linear membrane model to define the spatial dependence of eigenmodes in that direction, which includes a very small but finite web bending stiffness. In addition, the effect of the web line speed to frequencies is very small in the operation range of R2R systems in flexible electronics manufacturing [13, 40, 47, 48], we choose the partial differential equation of motion for out-of-plane vibrations of a stationary tensioned plate [49]

$$\rho_{web}\ddot{w}(x_1,x_3,\tau)+D\nabla^4 w(x_1,x_3,\tau)-N_{11}(x_3)w_{,11}(x_1,x_3,\tau)=P(x_1,x_3,\tau). \tag{4.1}$$

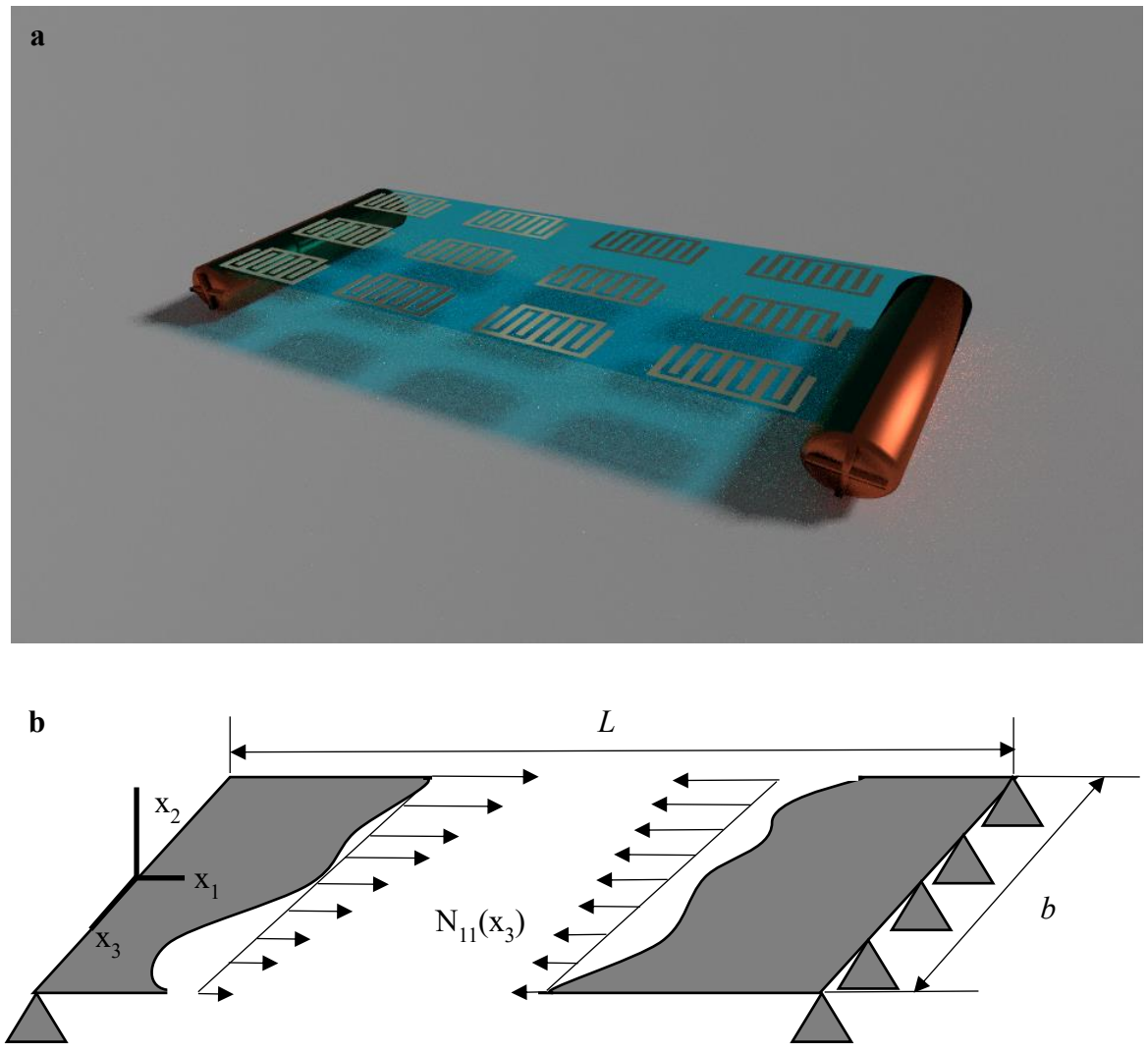

Figure 4.1. (a) A schematic for a single web in a functional R2R machine, (b) outline of the mechanics model with span geometry, coordinate systems, and nonuniform tension.

As shown in Figure 4.1(b), x_1, x_2, and x_3 are the coordinates along longitudinal (in the plane of the web and along the direction of web tension), transverse (normal to the web surface), and lateral (in the plane of the web but normal to the direction of web tension) directions, respectively; L is the in-span length of the web in the longitudinal direction; b is the cross-span width of the web in the lateral direction; τ is the time; $w(x_1, x_3, \tau)$ is the web deflection in the transverse direction; ρ_{web} is the web areal mass density; $D = Eh^3/[12(1-\upsilon^2)]$ is the web bending stiffness, with E, h, and υ denoting Young's modulus, thickness, and Poisson's ratio of the web, respectively; ∇^4 is the biharmonic operator; $N_{11}(x_3)$ is the web's uniaxial tension per unit width; $P(x_1, x_3, \tau)$ is the web surface pressure, such as air pressure in air-coupled web vibrations and pressure by contact force. We assume the tension varies linearly as

$$N_{11}(x_3) = N_{11}^{ave}\left(1 + \sigma\frac{2x_3}{b}\right), \tag{4.2}$$

where N_{11}^{ave} is the average web tension, σ is a dimensionless ratio for the linear variation of tension describing the discrepancy between maximum or minimum tension to N_{11}^{ave}. Especially, $N_{11}(\pm b/2) = 2N_{11}^{ave}$ or 0 when $|\sigma| = 1$, which indicates there is no tension applied on one of the free edge. So that, $|\sigma| = 1$ is a critical tension variation for local web wrinkling close to one of the free edges. We substitute Eq. (4.2) into Eq. (4.1)

$$\rho_{web}\ddot{w}(x_1, x_3, \tau) + D\nabla^4 w(x_1, x_3, \tau) - N_{11}^{ave}\left(1 + \sigma\frac{2x_3}{b}\right)w_{,11}(x_1, x_3, \tau) = P(x_1, x_3, \tau). \tag{4.3}$$

Turnbull *et al.* [50] has proved that simply supported boundary conditions can accurately predict linear vibrations of pre-tensioned webs across finite radius rollers. So that we use the following boundary conditions for both NCR and GCSM analyses:

1. the web is simply supported on the upstream and downstream rollers

$$\rho_{web}\ddot{w}(x_1, x_3, \tau) + D\nabla^4 w(x_1, x_3, \tau) - N_{11}^{ave}\left(1 + \sigma\frac{2x_3}{b}\right)w_{,11}(x_1, x_3, \tau) = P(x_1, x_3, \tau). \tag{4.4}$$

2. there is no shear force or bending moment for the free edges

$$\begin{aligned} &w_{,33}(x_1, \pm b/2, \tau) + \upsilon w_{,11}(x_1, \pm b/2, \tau) = 0, \\ &w_{,333}(x_1, \pm b/2, \tau) + (2-\upsilon)w_{,311}(x_1, \pm b/2, \tau) = 0. \end{aligned} \tag{4.5}$$

4.2.1 NCR Method

We develop an NCR method to measure N_{11}^{ave} and σ using the lowest symmetric transverse resonance frequency f_{11} and the lowest antisymmetric transverse resonance frequency f_{12} of a web. The eigenmodes of f_{11} and f_{12} are coupled by the nonuniform tension.

To describe the method in a consistent way for both in air and *in vacuo* R2R processes, we derive the key results in the presence of air effect. Our previous work predicted f_{11} and f_{12} for an air-coupled web system semi-analytically [45] but used a uniform tension assumption. In this paper, we improve on the previous work and assume that the web tension varies linearly. We derive the results and perform the convergence study as shown in Appendix C and obtain the lowest two web frequencies as

$$f_{11} = \sqrt{\frac{N_{11}^{ave}}{8L^2}\left[\left(\frac{1}{\bar{M}_{11}}+\frac{1}{\bar{M}_{12}}\right)-\sqrt{\left(\frac{1}{\bar{M}_{11}}-\frac{1}{\bar{M}_{12}}\right)^2+\frac{4\sigma^2}{3\bar{M}_{11}\bar{M}_{12}}}\right]}\,(\text{Hz}), \tag{4.6}$$

$$f_{12} = \sqrt{\frac{N_{11}^{ave}}{8L^2}\left[\left(\frac{1}{\bar{M}_{11}}+\frac{1}{\bar{M}_{12}}\right)+\sqrt{\left(\frac{1}{\bar{M}_{11}}-\frac{1}{\bar{M}_{12}}\right)^2+\frac{4\sigma^2}{3\bar{M}_{11}\bar{M}_{12}}}\right]}\,(\text{Hz}). \tag{4.7}$$

where the value of $\bar{M}_{11}$ and $\bar{M}_{12}$ are shown in Eqs. (C.32) and (C.33) and are described as functions of the hydrodynamic functions in (C.25), the web dimensions L and b, the web areal mass density ρ_{web}, and the air density ρ_{air}. We choose $\rho_{air} = 0$ for the *in vacuo* web systems, so that $\bar{M}_{11} = \bar{M}_{12} = \rho_{web}$ and

$$f_{11} = \sqrt{\frac{N_{11}^{ave}}{4\rho_{web}L^2}\left(1-\frac{|\sigma|}{\sqrt{3}}\right)}\,(\text{Hz}), \tag{4.8}$$

$$f_{12} = \sqrt{\frac{N_{11}^{ave}}{4\rho_{web}L^2}\left(1+\frac{|\sigma|}{\sqrt{3}}\right)}\,(\text{Hz}). \tag{4.9}$$

The linear variation of tension σ changes significantly the frequencies and their corresponding mode shapes compared to the uniform tension case. Figure 4.2 shows the effect of σ to f_{11}, f_{12} for both in air and *in vacuo* web systems. The substrate is chosen to be a PET web with the same properties as in the experimental cross validation, which are $L = 228.6$ mm,

$b = 152.4$ mm, $\rho_{web} = 178.67$ g/m^2 (these three properties are measured), $h = 127$ μm, $E = 4.8$ GPa (these two properties are provided by DuPont [51]), and $\upsilon = 0.33$ [52]. The air density $\rho_{air} = 1.208$ kg/m^3 and the average tension $N_{11}^{ave} = 150.47$ N/m . The frequencies are calculated by Eqs. (4.6) - (4.9). The corresponding mode shapes with $\sigma = 0$ and 0.5 are obtained by 4×4 AMM with Eq. (C.17) and the matrices in Eqs. (C.22) - (C.24). For the *in vacuo* web systems, $\mathbf{M}'^{(4\times4)}_{air} = \mathbf{0}$. The small boxes with grey bars show the contributions of basis functions W_{11}, W_{12}, W_{13}, and W_{14} (see in Eq. (C.21)) to their corresponding mode shapes. The following are key observations:

1. In both *in vacuo* and in air cases, increasing σ reduces the lowest symmetric frequency f_{11} and increases the lowest antisymmetric frequency f_{12}.
2. f_{11} and f_{12} are tightly clustered for the *in vacuo* web system under uniform tension (*i.e.* $\sigma = 0$) but split apart by nonuniform tension.
3. The f_{11} and f_{12} of an uniform tensioned in air web system are separated since they have different magnitudes of added air masses.
4. From the grey bars with $\sigma = 0$, we can see that the modes 11 and 12 are purely symmetric and antisymmetric, respectively. There is no cross coupling between symmetric and antisymmetric basis functions in a uniform tensioned web system.
5. Nonuniform tension causes coupling between symmetric and antisymmetric basis functions in the mode shapes and changes mode shapes for both *in vacuo* and in air cases.

To measure N_{11}^{ave} and σ by f_{11} and f_{12}, we rewriting Eqs. (4.6) and (4.7) inversely and obtain a closed-form expression as

$$N_{11}^{ave} = \frac{4L^2 \bar{M}_{11} \bar{M}_{12} (f_{11}^2 + f_{12}^2)}{\bar{M}_{11} + \bar{M}_{12}}, \tag{4.10}$$

$$\sigma = \pm \sqrt{3 - \frac{3\left(\bar{M}_{11} + \bar{M}_{12}\right)^2 f_{11}^2 f_{12}^2}{\bar{M}_{11} \bar{M}_{12} \left(f_{11}^2 + f_{12}^2\right)^2}}. \tag{4.11}$$

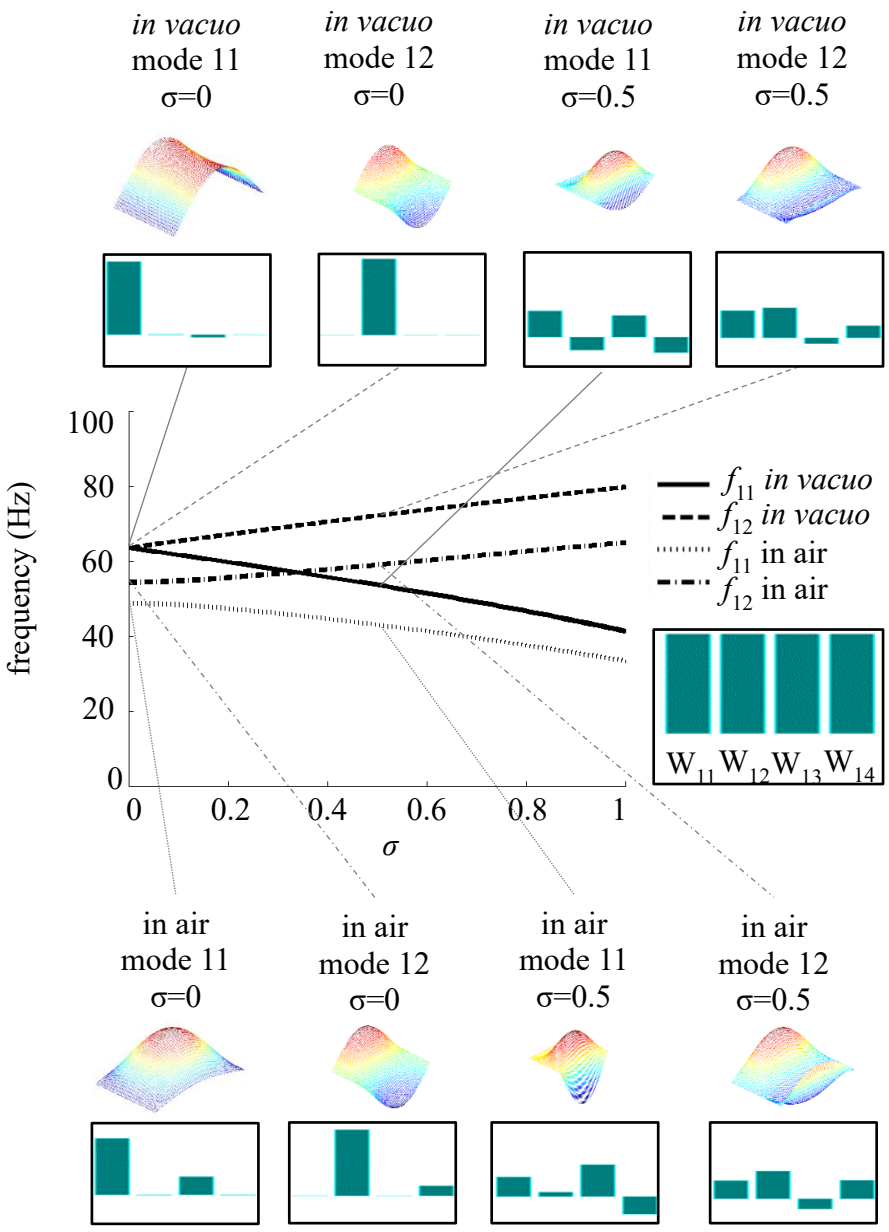

Figure 4.2. f_{11} and f_{12} as a function of σ for in air and *in vacuo* web systems with the corresponding mode shapes when $\sigma = 0$ and 0.5. The grey bars show the contribution of each basis functions in the mode shapes. The basis functions W_{11}, W_{12}, W_{13}, and W_{14} used here are shown in Eq. (A.21). A PET web is chosen with the properties $L = 228.6$ mm, $b = 152.4$ mm, $\rho_{web} = 178.67$ g/m^2, $h = 127$ μm, $E = 4.8$ GPa, $\upsilon = 0.33$, $\rho_{air} = 1.208$ kg/m^3, $N_{11}^{ave} = 150.47$ N/m.

Note that the NCR method can solve the linear variation of tension but not its direction, since both positive and negative value of σ gives the same frequencies as shown in Eqs. (4.6) - (4.9). There is no air loading in *in vacuo* R2R systems, and we simplify Eqs. (4.10) and (4.11) as

$$N_{11}^{ave} = 2L^2\rho_{web}(f_{11}^2 + f_{12}^2), \tag{4.12}$$

$$\sigma = \pm\sqrt{3 - \frac{12 f_{11}^2 f_{12}^2}{\left(f_{11}^2 + f_{12}^2\right)^2}}. \tag{4.13}$$

4.2.2 GCSM Method

The second method we developed is a GCSM method. In this method, we gently apply multiple contact forces in at least two locations along the web width and measure the deflections. The forces are applied gently to make sure the web deforms far below its plastic deformation region. The web tension distribution (N_{11}^{ave} and σ) is obtained by nonlinear regression of local contact stiffness in different locations. In each contact location, multiple local contact forces are fitted with their deflections cubically to extract the local contact stiffness for a linear elastic model. In addition, plastic deformation locally damages the web and reduces the accuracy of measurement. To avoid the local plastic deformation, we apply the contact force gently and with a large contact sphere as a Ping-Pong ball to make sure that all the work done by contact force is absorbed by the web strain energy in the elastic region.

To understand the relation between web tension distribution, web deflections, and web stiffness, we assume the web deflection determined by Eq. (4.1) in the quasi static loading case (*i.e.* $\ddot{w} = 0$) is a linear combination of admissible basis functions as

$$W(x_1, x_3) = \sum_{m=1}^{M}\sum_{n=1}^{N} \sin\frac{m\pi x_1}{L}\left[A_{mn}\sin\frac{(2n-1)\pi x_3}{b} + B_{mn}\cos\frac{(2n-2)\pi x_3}{b}\right], \tag{4.14}$$

where M and N are the number of functions along x_1 and x_3 directions, respectively. A_{mn} and B_{mn} are the amplitude of antisymmetric and symmetric components, respectively. In Appendix D, we show the details of derivations from Eqs. (4.3) - (4.5) and (4.14) and obtain Eq. (4.15) to describe the relation between A_{mn}, B_{mn}, N_{11}^{ave}, σ, and the local contact force F as

$$\begin{bmatrix}\mathbf{C}_1 & \mathbf{C}_2\\ \mathbf{C}_3 & \mathbf{C}_4\end{bmatrix}\begin{Bmatrix}\mathbf{A}\\ \mathbf{B}\end{Bmatrix} = \sin\frac{m\pi X_1}{L}\begin{Bmatrix}\mathbf{C}_5\\ \mathbf{C}_6\end{Bmatrix}, \tag{4.15}$$

the descriptions of matrices $\mathbf{C}_1$ to $\mathbf{C}_4$ and vectors $\mathbf{A}$, $\mathbf{B}$, $\mathbf{C}_5$, and $\mathbf{C}_6$ are shown in Eqs. (D.8) - (D.15). X_1 is the coordinate of the contact location in x_1 direction. Once the deflection of a web under the contact force is obtained, we can solve the local contact stiffness as

$$k(X_1, X_3) = \frac{F}{W(X_1, X_3)} = \frac{1}{\sum_{m=1}^{M}\sum_{n=1}^{N} \sin\frac{m\pi X_1}{L}\left[A'_{mn}\sin\frac{(2n-1)\pi X_3}{b} + B'_{mn}\cos\frac{(2n-2)\pi X_3}{b}\right]}. \tag{4.16}$$

where X_3 is the coordinate of the contact location in x_3 direction, $A'_{mn} = \frac{A_{mn}}{F}$, and $B'_{mn} = \frac{B_{mn}}{F}$. In Appendix D, a convergence study on deflections of the center of the web $(X_1, X_3) = \left(\frac{L}{2}, 0\right)$ and the center of a free edge $(X_1, X_3) = \left(\frac{L}{2}, -\frac{b}{2}\right)$ shows choosing $M = 51$ and $N = 18$ ensures a 1% discrepancy to $M = 1\text{E}4$ and $N = 1\text{E}4$. A R2R process designer could also choose to use $M = 3$ and $N = 5$ with a 20% compensation in their calculations.

From Table D.1 we can see that applying the same contact force on different locations gives different local deflections. To understand the deflection shape of the entire web with respect to the contact location, we plot 3D deflection profiles of a PET web with a same contact force $F = 0.1\,\text{N}$ on four different locations with $(X_1, X_3) = \left(\frac{L}{2}, 0\right), \left(\frac{L}{2}, -\frac{b}{2}\right), \left(\frac{L}{4}, 0\right)$, and $\left(\frac{L}{4}, -\frac{b}{2}\right)$, as shown in Figure 4.3. The web properties are the same as used in Figure 4.2 but with $\sigma = 0$. We choose the number of basis functions as $M = 51$ and $N = 18$. The results show under a same contact force, along x_1 direction the deflection is larger on the center than close to the rollers, which agrees with the restriction of simply supported boundary conditions in Eq. (4.4); while along x_3 direction, the web deflects more with a contact force on the free edge than on the center, which means there is an edge effect of web stiffness.

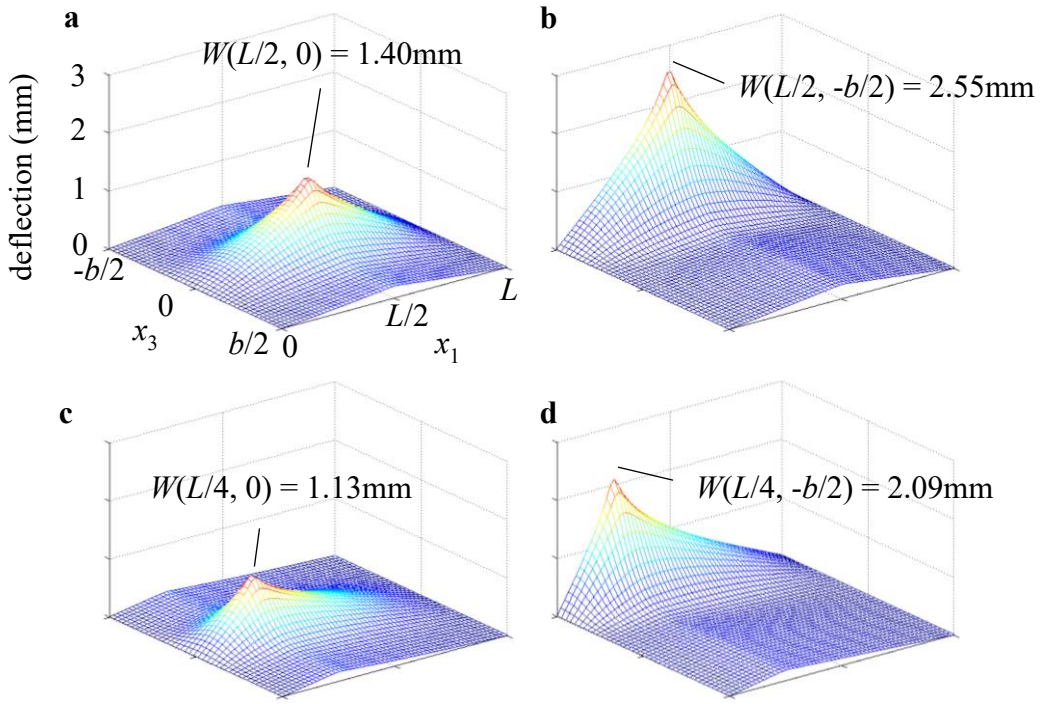

Figure 4.3. 3D deflections profile of a PET web under a 0.1 N contact force applied on four different locations (a) $(X_1, X_3) = \left(\frac{L}{2}, 0\right)$, (b) $(X_1, X_3) = \left(\frac{L}{2}, -\frac{b}{2}\right)$, (c) $(X_1, X_3) = \left(\frac{L}{4}, 0\right)$, and (d) $(X_1, X_3) = \left(\frac{L}{4}, -\frac{b}{2}\right)$. The basis functions are chosen with $M = 51$ and $N = 18$. The web properties are $L = 228.6$ mm, $b = 152.4$ mm, $\rho_{web} = 178.67$ g/m^2, $h = 127$ μm, $E = 4.8$ GPa, and $\upsilon = 0.33$, with a uniform tension of $N_{11}^{ave} = 150.47$ N/m and $\sigma = 0$.

To understand the spatial variations of the web's contact stiffness, we plot the stiffness profiles of a web under a same N_{11}^{ave} but different σ's in Figure 4.4. The contact stiffness is solved by Eqs. (4.15) and (4.16). We choose all other web properties the same as for Figures 4.2 and 4.3. Figures 4.4(a) to (c) show the 3D web contact stiffness profiles of the web with $\sigma = 0,\ 0.2$, and $0.4,$ respectively and their 2D projected contours on the $x_1 - x_3$ plane. They are plotted in the region with $x_1 \in [0.05L, 0.95L]$, because the web is simply supported at $x_1 = 0$ and L where the web contact stiffness is infinity. Figure 4.4(d) is the corresponding cross-span profiles of web contact stiffness at $x_1 = L/2$. The following are key observations:

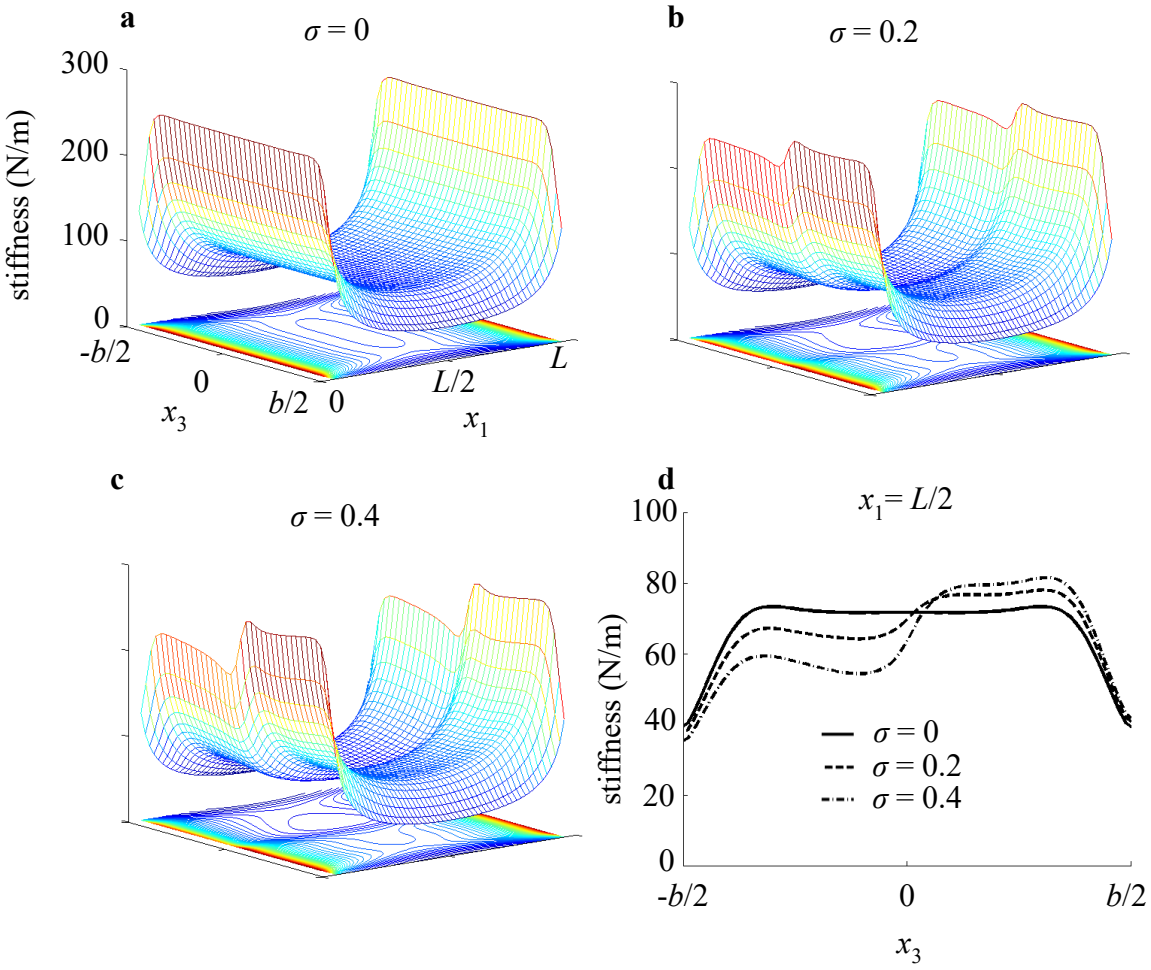

Figure 4.4. The contact stiffness profiles of a PET web with $L = 228.6$ mm, $b = 152.4$ mm, $\rho_{web} = 178.67$ g/m^2, $h = 127$ μm, $E = 4.8$ GPa, $\upsilon = 0.33$, and $N_{11}^{ave} = 150.47$ N/m. The basis functions are chosen with $M = 51$ and $N = 18$. (a), (b), and (c) are the 3D contact stiffness profiles of the web with $\sigma = 0$, 0.2, and 0.4, respectively and their 2D projected contours on the $x_1 - x_3$ plane. They are all plotted in the region with $x_1 \in [0.05L, 0.95L]$, since the web is simply supported with infinity web stiffness at $x_1 = 0$ and L. d) shows the cross-span contact stiffness profiles at $x_1 = L/2$ for the web with $\sigma = 0$, 0.2, and 0.4.

1. Along the longitudinal direction, the contact stiffness close to the simply supported boundaries is higher than the center region. Eventually, the contact stiffness is infinity on these boundaries,
2. There are edge effects close to the free edges. Along the lateral direction, the local contact stiffness close to the edges can drop down to half of it in the central region.

3. When the web is under a uniform distributed tension, its contact stiffness profile is symmetric to both $x_1 = L/2$ and $x_3 = 0$.
4. Nonuniform tension changes the contact stiffness profile to asymmetric to $x_3 = 0$.

With the linear elastic Kirchhoff plate model, we need to extract the local contact stiffness in a linear elastic deformation region from contact force and web deflection before solving N_{11}^{ave} and σ. The web deflection by a gentle contact force can easily beyond the web thickness, so that the Kirchhoff hypothesis is not suitable [53]. Taking the example in Table D.1 and Figure 4.3, a 0.1 N contact force on 127 μm thick web can deflect the web in millimeters. Von Kármán theory is used for large deformation of plates [54]. Based on the strain-displacement relations in Von Kármán theory and the antisymmetric contact force and web deflection relation on two sides of the web in transverse direction, we write the following equation

$$F = k_1' \frac{W(X_1, X_3)}{h} + k_3' \left(\frac{W(X_1, X_3)}{h} \right)^3, \tag{4.17}$$

where k_1' and k_3' are the linear and cubic coefficient to the deflection to web thickness ratio. So that, we measure the web deflection under multiple local contact forces on the same location of the web to obtain k_1' and k_3' with least squares fitting. The local contact stiffness in linear elastic deformation region yields

$$k = \frac{k_1'}{h}. \tag{4.18}$$

After measuring the contact stiffnesses in at least two locations with different X_3's, we can solve N_{11}^{ave} and σ of the web. Solving contact stiffness from known N_{11}^{ave} and σ is straight forward by using Eqs. (4.15) and (4.16), however a closed-form solution to solve N_{11}^{ave} and σ from the contact stiffness is not available. We use nonlinear regression with the trust-region-reflective algorithm to solve N_{11}^{ave} and σ. In the optimization procedure, we minimize the root mean square error between the measured stiffnesses and the model as

$$e = \sqrt{\frac{1}{r} \sum_{i=1}^{r} \left(k(X_1, X_3^{(i)}) - k^{(\text{model})}(X_1, X_3^{(i)}) \right)^2}, \tag{4.19}$$

where r is the total number of locations being measured. The gradients of e to N_{11}^{ave} and σ in each iteration step is chosen to be those between ±10% of current estimated N_{11}^{ave} and σ, respectively.

4.3 Experimental Procedure

We perform two experimental tests of the developed methods. First, we sequentially test both NCR and GCSM on a stationary test stand. This enables cross validation of the two methods. Next, we use the NCR method to do in-line monitoring of a commercial R2R system. This demonstrates the performance of the technique in a realistic manufacturing environment.

4.3.1 Cross Validation Experiment

Schematics and pictures of the stationary test scan used for cross validation is shown in Figure 4.5. Figure 4.5(a) is a schematic of our implementation of the NCR method. The web is excited by a speaker (VISATON® FR 10, Art. No. 2020, 20 Watt, 4 Ω, VISATON GmbH & Co. KG, Berlin, Germany) and the response is measured by a laser sensor (Microtrak 7000, MTI Instruments Inc., Albany, NY). Figures 4.5 (b) and (c) show a picture of this setup. Experiments are done with a PET film matching properties and dimensions as used in the simulations shown in Figures 4.3 and 4.4. A section of the PET web is painted white to facilitate measurements with the laser sensor. Tension is applied by hanging either a 2.34 kg or 2.85 kg low-carbon steel rod at the end of the web. Careful roller and web alignment is performed to minimize tension nonuniformity. A data acquisition system (NI PXIe-1071, NI PXIe-8102, NI PXIe-6124, NI BNC-2120, National Instruments™, Austin, TX), an amplifier (Vernier Software & Technology, Beaverton, OR) and the speaker are used to excite the web and record the response of the laser sensor. A chirp signal that varies from 1 Hz to 100 Hz in 200 sec with an amplitude 0.005 V is used to drive the speaker. The amplitude and phase of the laser sensor response is computed with a Fast Fourier Transform. The transfer function of the web is found from the radio of amplitudes and the differences of phases of a measurement on the web and a measurement directly on the speaker. The resonance frequencies are obtained by a single degree-of-freedom (SDOF) fitting of the transfer function to its half-power bandwidth as shown in Appendix E. Figures 4.5 (d) and (e) are the system schematic and a picture of our implementation of the GCSM method. A force gauge (VTSYIQI HF-5 Digital

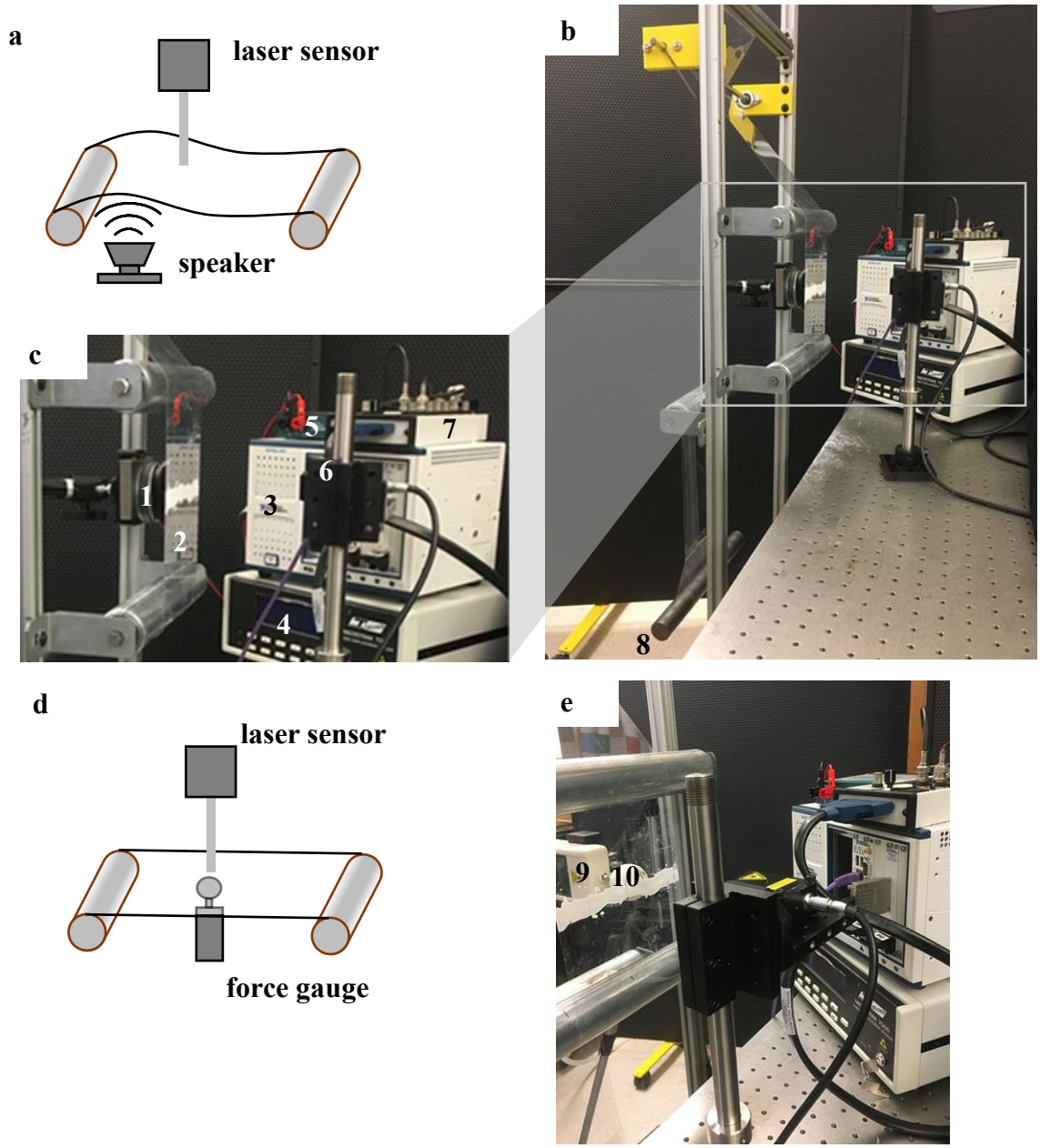

Figure 4.5. The sketches of measurement systems and experimental setups for the cross validations. (a) A sketch of NCR measurement system; (b) a home-made stationary test stand with a PET web with tension applied by a hanging low-carbon steel rod labelled as 8; (c) zooming in of measurement component in (b) for the NCR, 1 speaker, 2 PET web, 3 a chassis with embedded controller and multifunction data acquisition device, 4 Laser-based triangulation system controller, 5 power amplifier, 6 laser sensor head, 7 terminal block; d) a sketch of GCSM measurement system; e) the measurement component for the GCSM measurement, 9 force gauge, 10 Ping-Pong ball contact head.

Push Pull Force Gauge, Vetus Electronic Technology Co., Ltd., Hefei, China) with a Ping-Pong ball contact head is used to both deform the web and measure the resulting force. The same laser sensor and data acquisition system as the NCR method is used to measure and record the web deformation at the loading location. Use of the Ping-Pong ball contact head with its relatively large contact area minimizes local plastic deformation of the web. Forces from 0.06 N to 0.13 N in increments of between 0.004 N and 0.01 N are applied to the web with corresponding web deformations varying between 0.55 mm to 1.10 mm.

4.3.2 In-line Monitoring Experimental Setup

To demonstrate the applicability of our method on a commercial R2R system, we use the NCR method to in-line measure the web tension distribution in two spans of a DICEweb digital inkjet printer R2R system (Prototype & Production Systems, Inc., Minneapolis, MN). A picture of this setup is shown in Figure 4.6. In the DICEweb system, the web tension is applied by the torque from the unwind roller servo motor and the web line speed is adjusted by the torque from the rewind roller servo motor. Both rollers have sensors to measure the radii of rolls to control the applied torques. The DICEweb system has no feedback control for the tension and speed dynamics. For these measurements we use an opaque PET web, whose properties are $\rho_{web} = 111.18$ g/m^2, $h = 76.2$ μm, $b = 152.4$ mm, $E = 4.8$ GPa, and $\upsilon = 0.33$. The in-span lengths of span 1 and span 2 are 292.1 mm and 107.95 mm, respectively. As shown in Figure 4.6(a), Span 1 is upstream, where a module was originally set up for cutting the web to replace a running out unwind roll with a new one. Span 2 is in the functional area of inkjet printers. Figures 4.6(b) and (c) show the setup of the laser sensor and speaker in the two spans. We place the laser head with its laser sensor orientation orthogonal to the web moving direction.

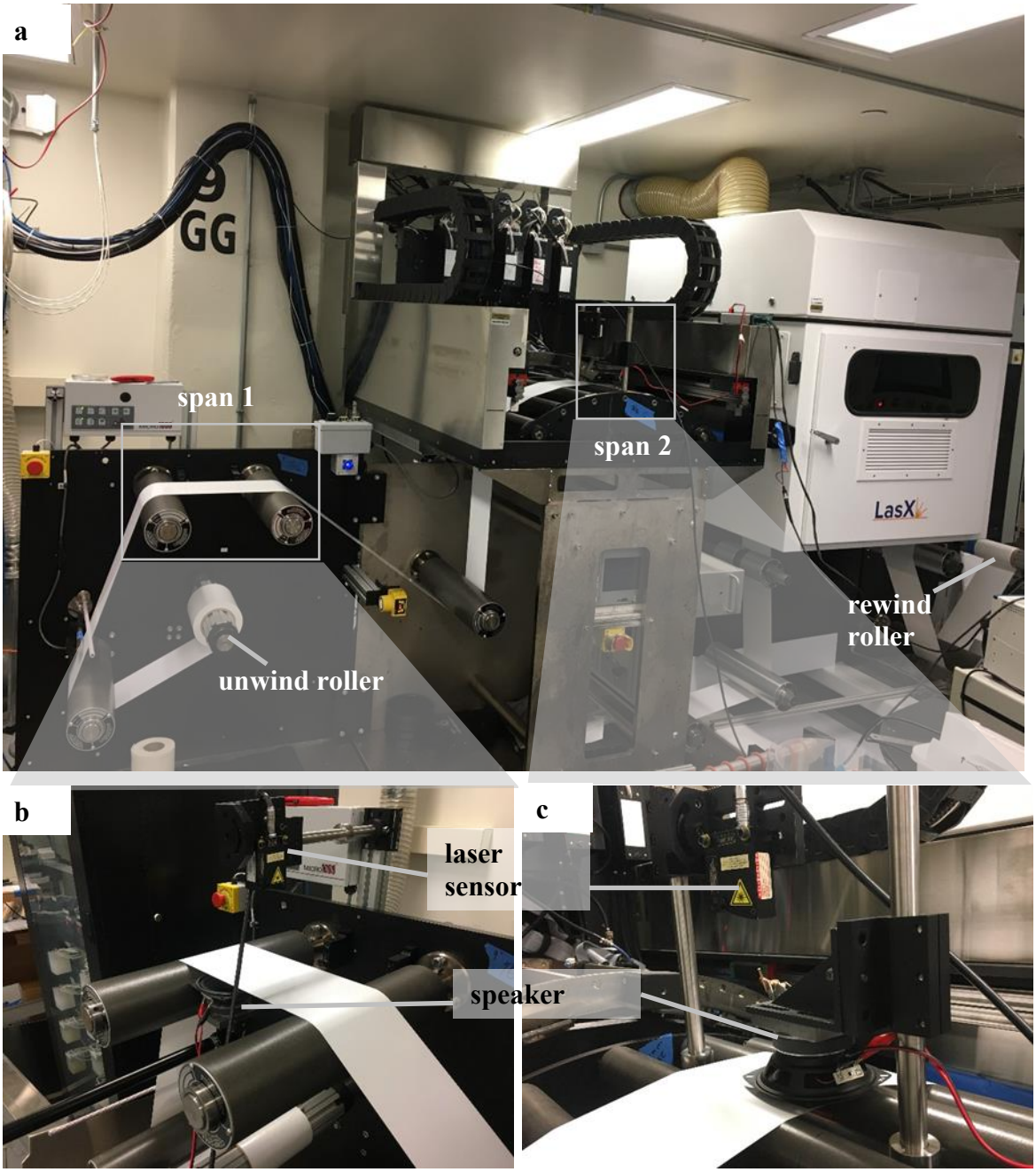

Figure 4.6. (a) A DICEweb digital inkjet print R2R system with the locations of two spans for measurements, (b) and (c) the setups of laser sensor and speaker in span 1 and 2, respectively.

4.4 Experimental Results and Discussion

Figure 4.7 shows the results of the NCR and GCSM cross-validation experiment. We applied the NCR method with a fixed speaker position and seven laser sensor positions ($X_1 = 101.6$ mm,

$X_3 = 0$ mm, ± 22.86 mm, ± 45.72 mm, ± 68.58 mm). The GCSM mothed is applied with the contact head positioned at the same seven locations. Figures 4.7(a) to (c) are for a PET web with the 2.34 kg hanging mass and Figure 4.7(d) is for the same PET web with the 2.85 kg hanging mass.

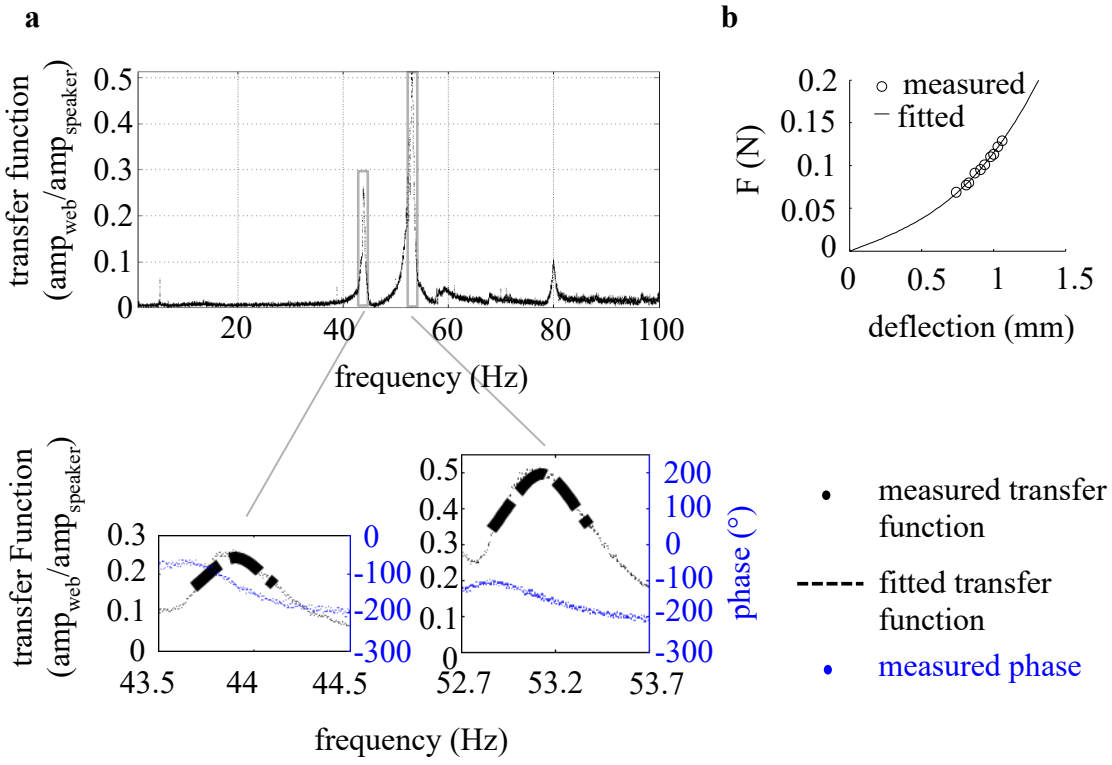

Figure 4.7. The results of cross validation experiment with a PET web with $L = 228.6$ mm, $b = 152.4$ mm, $\rho_{web} = 178.67$ g/m^2, $h = 127$ μm, $E = 4.8$ GPa, and $\upsilon = 0.33$. The web tension of experiment in (a) to (c) are applied with 2.34 kg hanging mass, and in (d) is 2.85 kg hanging mass. (a) The frequency response function on $X_1 = 101.6$ mm, $X_3 = -45.72$ mm with the inserted graphs showing the local measured transfer functions, phases, and SDOF fitted transfer functions of the lowest two frequencies. (b) The fitting of multiple contact force and deflections on $X_1 = 101.6$ mm, $X_3 = -45.72$ mm using Eq. (4.17). (c) The comparison of contact stiffness and web tension using NCR method and GCSM method with tension applied by a low-carbon steel rod (1 feet length, 1.375 inch diameter, McMaster-Carr), $\rho_{air} = 1.208$ kg/m^3. (d) The comparison of contact stiffness and web tension using NCR method and GCSM method with tension applied by a low-carbon steel rod (1 feet length, 1.5 inch diameter, McMaster-Carr), $\rho_{air} = 1.198$ kg/m^3.

Figure 4.7 continued

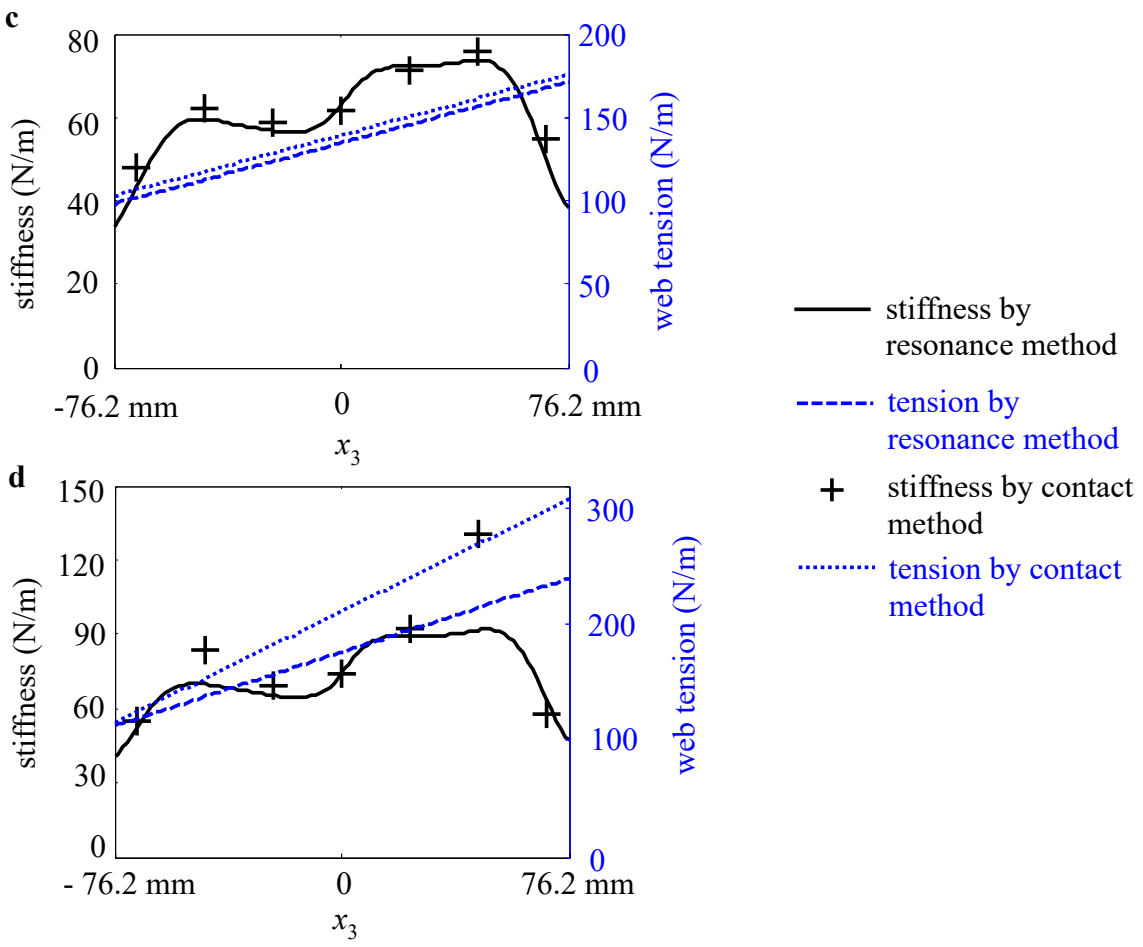

Figures 4.7(a) and (b) show the raw experiential data for the measurement with the 2.34 kg hanging mass and at $X_1 = 101.6$ mm, $X_3 = -45.72$ mm. Figure 4.7(a) shows the frequency response function between 1 Hz to 100Hz with inserted graphics showing the resonance peaks. The expected 180° shift in phase is observed as the frequency moves across the resonance regions. The average value and one standard deviation of the first two resonance frequencies are $f_{11} = 43.89 \pm 0.02$ Hz and $f_{12} = 53.22 \pm 0.06$ Hz. Figure 4.7(b) shows the results of fitting the contact force and deflection with Von Kármán theory for the GCSM method. Local contact stiffness in the linear elastic deformation region is extracted using Eqs. (4.17) and (4.18), resulting $k_1' = 0.007909 \pm 0.000223$, $k_3' = 0.000107 \pm 0.000005$, and $k = 62.27 \pm 1.76$ N/m.

Figure 4.7(c) shows the comparison of contact stiffness and web tension using the NCR and GCSM methods with the 2.34 kg hanging mass. The environmental conditions of the lab during

this measurement are 102.67 kPa air pressure, 21 ℃ air temperature, and 68% relative humidity resulting in a calculated air density of $\rho_{air} = 1.208\ \text{kg/m}^3$ [55]. The root mean square error between the stiffnesses of the seven contact locations by the NCR method and as measured by the GCSM method is 3.00 N/m. The NCR method measures a web tension with $N_{11}^{ave} = 134.49$ N/m and $\sigma = \pm 0.2724$, while GCSM method gives $N_{11}^{ave} = 139.26$ N/m and $\sigma = 0.2619$ with a regression error (Eq. (4.19)) $e = 2.4594$. Since the NCR method could not identify the sign of σ, we choose σ from the NCR method to have the same sign as that from the GCSM method to plot in Figure 4.7(c) and solve the discrepancies of N_{11}^{ave}, maximum tension $N_{11}^{ave}\left(1+|\sigma|\right)$, and minimum tension $N_{11}^{ave}\left(1-|\sigma|\right)$ between two methods to be 3.43%, 2.62%, and 4.78%, respectively. The ratio of cross-span tension variation to average tension (2σ) is 54.48%. This amount of variation can significantly affect the performance of printed electronics devices and was present despite our best effects at web alignment. In addition, observations show the edge effect of contact stiffness agrees with theory.

Figure 4.7(d) shows the comparison of contact stiffness and web tension using the NCR and GCSM methods with the 2.85 kg hanging mass. The environmental conditions for this measurement were 101.84 kPa air pressure, 21 ℃ air temperature, and 76% relative humidity with a calculated air density $\rho_{air} = 1.198\ \text{kg/m}^3$. The measured resonance frequencies are $f_{11} = 49.01 \pm 0.06$ Hz and $f_{12} = 62.16 \pm 0.55$ Hz. The root mean square error between the contact stiffness solved by the NCR method and the GCSM method is 15.84 N/m. The average web tension and the linear variation of tension by the NCR method are $N_{11}^{ave} = 176.59$ N/m and $\sigma = \pm 0.3602$, while the GCSM method gives $N_{11}^{ave} = 211.84$ N/m and $\sigma = 0.4542$ with $e = 12.6698$. The discrepancies of N_{11}^{ave}, maximum tension, and minimum tension between two methods are 16.64%, 28.25%, and 2.34%, respectively. We observe anomalously high contact stiffness at $X_3 = \pm 45.72$ mm from GCSM method on this web. The larger local contact stiffness may cause local web wrinkles to appear with high applied tension. In that case, the GCSM method is not accurate and predicts both higher average tension and linear variation of tension.

From the results in Figures 4.7(c) and (d), the contact stiffness from two methods agrees at most locations. The NCR method measures N_{11}^{ave} and σ accurately, but cannot accurately predict

local anomalously high contact stiffness. The GCSM method can measure local contact stiffness accurately, but fails to predict N_{11}^{ave} and σ with local anomalously high contact stiffness. Not including the two local anomalously high contact stiffness in Figure 4.7(d), we obtain $N_{11}^{ave} = 175.33$ N/m and $\sigma = 0.2894$ with $e = 2.9621$. Compared with the results by the NCR method, the discrepancies of N_{11}^{ave}, maximum tension, and minimum tension between two methods reduce to 0.72%, 5.88%, and 10.27% when excluding the two anomalously high contact stiffness measurements.

The two methods NCR and GCSM can also be used for moving webs so long as the transport speeds are much smaller than the critical speed of the web. As speed of the web approaches critical transport speed, the resonance frequencies drop down to zero [48].

To demonstrate the performance of the NCR method in a realistic manufacturing environment, we perform single spot location measurements at three different line speeds, and over two different spans on a commercial R2R system. Table 4.1 summarizes these results. The environmental conditions during the measurements are 102.71 kPa air pressure, 21℃ air temperature, 43% humidity, and an air density $\rho_{air} = 1.212$ kg/m^3. The frequency is swept between 40 Hz and 100 Hz to measure resonances in span 1 and between 140 Hz and 200 Hz to measure resonances in span 2. The cross span linear variation in tension is negligible in span 2, but varies by up to 35.58% in span 1, showing that different spans of a R2R system can have different variations of tension. The average tension is between 21.46% and 28.29% smaller in span 2 compared to span 1.

When the linear variation of tension is small, we observe cases where σ^2 takes on a small negative value (*i.e.* imaginary σ, see Appendix F). This is caused by neglecting higher order variation of tension and errors in fitting and measurements; however, this does not significantly affect the use of the NCR method as it is reasonable to approximate cases with small negative σ^2 as having uniform tension.

We performed the in-line measurements over a range of speed typical for flexible printed electronics manufacturing [13, 47]. As described in Appendix G, we use an axially moving string model to estimate the web's critical transport speed. We define the normalized line speed as the ratio of the line speed to the critical speed. For our measurements, the maximum tested line speed of 2 m/min is much less than the critical transport speeds, which are between 53.57 m/sec and

55.89 m/sec for span 1 and between 47.32 m/sec and 47.48 m/sec for span 2, indicating it is safe to neglect the effect of web speed in our methods. However, the measured tension of the stationary case in span 1 is significantly smaller than in the moving cases. We hypothesize that this is the effect of the motion of the unwind and rewind motors on the web tension. When the web start to move, the resistance by frictions between web and rollers changes and lead to tension variation in some spans.

Table 4.1. Results of in-line measurement of the web tension distribution in two spans of the DICEweb digital inkjet print R2R system, $\rho_{air} = 1.212$ kg/m^3.

Line speed (m/min)	Normalized line speed	f_{11} (Hz)	f_{12} (Hz)	N_{11}^{ave} (N/m)	σ^2	Real(2σ)
Span 1, L = 292.1 mm, b = 152.4 mm						
0	0	60.37±0.00	73.20±0.00	319.08	0.0316	0.3558
0.98 to 1.26	2.92×10^{-4} to 3.76×10^{-4}	63.45±0.11	75.98±0.04	347.30	0.0180	0.2680
1.93 to 2.24	5.77×10^{-4} to 6.70×10^{-4}	63.09±0.04	75.90±0.18	345.25	0.0229	0.3029
Span 2, L = 107.95 mm, b = 152.4 mm						
0	0	165.57±0.00	178.65±0.00	250.62	-0.0029	0
1.07 to 1.31	3.77×10^{-4} to 4.61×10^{-4}	164.54±0.02	178.56±0.03	249.05	-0.0002	0
1.85 to 2.22	6.52×10^{-4} to 7.82×10^{-4}	164.47±0.06	178.53±0.01	248.91	-0.0001	0

Figures 4.8 (a) to (c) show the transfer function and the SDOF fittings used to extract resonance frequencies at line speeds set to 0, 1 m/min, and 2 m/min, respectively. The actual line speed fluctuates by up to 0.26 m/min when the web moves. The transfer functions of the moving webs are noisier than those of the stationary web. There are several probable causes for this noise. The first is the effect of nonuniformity and roughness of the web surface on the output of the laser

sensor. As the web moves, imperfections in the web surface could be falsely detected as web deflection. The second possible cause is noise from the motor driving the web motion being transmitted through the web causing it to vibrate. Such spurious vibrations can be detected by the laser sensor and captured in the data analysis. A final possible source of this noise is variation in web tension induced by the unwind and rewind motors as they move. Ultimately, this noise does not stop us from correctly identifying the web's resonance frequencies and therefore is not an impediment to implementing the NCR method.

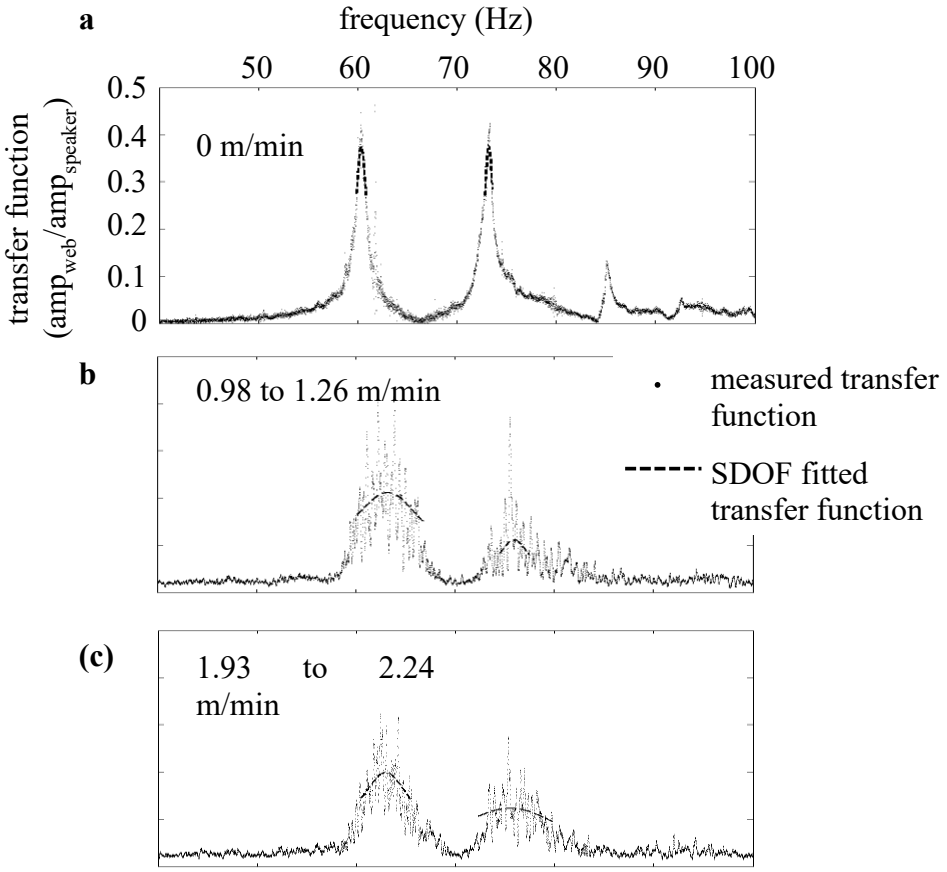

Figure 4.8. The frequency response function under an up-chirp frequency sweep signal from 40 to 100Hz with the half-power bandwidth SDOF fittings in span 1. (a) stationary web, (b) moving web with line speed between 0.98 and 1.26 m/min (setup value is 1 m/min) during the measurement, (c) moving web with line speed between 1.93 and 2.24 m/min (setup value is 2 m/min) during the measurement.

4.5 Conclusions

Nonuniform web tension in R2R processes can lead to nonuniform device performance crossing the width of web. We develop and cross validate an NCR method and a GCSM method to measure the average web tension and its linear variation. These methods are in-expensive and friendly to adapt to different spans with different web path flexibly without the needs of new calibration. In addition, we in-line measure the tension distribution in two spans of a commercial R2R system. The main results are as follows:

1. Increasing linear variation of tension reduces the lowest symmetric frequency and increases the lowest antisymmetric frequency, who are tightly clustered *in vacuo* with uniform tension.
2. The linear varied tension coupled symmetric and antisymmetric basis functions.
3. We developed an NCR method with a closed-form expression to measure average tension and its linear variation by the lowest symmetric and antisymmetric frequencies.
4. The local contact stiffness close to the free edges of a web is smaller than its central region. On the other word, the web deforms more with a contact force on its edge than with a same contact force on its central region.
5. Nonuniform tension changes the contact stiffness profile to asymmetric to its cross-span center.
6. We developed a GCSM method to measure the average web tension and its linear variation from local contact stiffness by nonlinear regression.
7. The NCR method and GCSM method are experimentally cross validated with 3.43% discrepancy in the average web tension and 4.12% discrepancy in the linear variation of tension when there is no local wrinkling.
8. We use the NCR method to in-line measure the tension in two spans of a commercial R2R system under three different line speeds, respectively.
9. Different spans in a same R2R system can have different average tension and different linear variation of tension.
10. In the commercial R2R system we tested, the cross-span linear variation can be up to 35.58%.

Overall, we expect these methods provide accurate, reliable, and inexpensive manners for measuring nonuniform web tension to improve quality control of R2R processes for flexible and printed electronics and maximize device yields.

4.6 References

[1] Noh, J., Jung, M., Jung, K., Lee, G., Lim, S., Kim, D., ... & Cho, G. (2011). Integrable single walled carbon nanotube (SWNT) network based thin film transistors using roll-to-roll gravure and inkjet. *Organic Electronics*, *12*(12), 2185-2191.

[2] Hassinen, T., Ruotsalainen, T., Laakso, P., Penttilä, R., & Sandberg, H. G. (2014). Roll-to-roll compatible organic thin film transistor manufacturing technique by printing, lamination, and laser ablation. *Thin Solid Films*, *571*, 212-217.

[3] Kim, J., Hassinen, T., Lee, W. H., & Ko, S. (2017). Fully solution-processed organic thin-film transistors by consecutive roll-to-roll gravure printing. *Organic Electronics*, *42*, 361-366.

[4] Grubb, P. M., Mokhtari Koushyar, F., Lenz, T., Asghari, A., Gan, G., Xia, W., ... & Chen, R. T. (2019). High speed roll-to-roll printable transistor enabled by a pulsed light curable CNT ink. *Journal of Manufacturing and Materials Processing*, *3*(2), 33.

[5] Arcila-Velez, M. R., Zhu, J., Childress, A., Karakaya, M., Podila, R., Rao, A. M., & Roberts, M. E. (2014). Roll-to-roll synthesis of vertically aligned carbon nanotube electrodes for electrical double layer capacitors. *Nano Energy*, *8*, 9-16.

[6] Yeo, J., Kim, G., Hong, S., Kim, M. S., Kim, D., Lee, J., ... & Ko, S. H. (2014). Flexible supercapacitor fabrication by room temperature rapid laser processing of roll-to-roll printed metal nanoparticle ink for wearable electronics application. *Journal of Power Sources*, *246*, 562-568.

[7] Kang, S., Lim, K., Park, H., Park, J. B., Park, S. C., Cho, S. P., Kang, K., & Hong, B. H. (2018). Roll-to-Roll Laser-Printed Graphene–Graphitic Carbon Electrodes for High-Performance Supercapacitors. *ACS applied materials & interfaces*, *10*(1), 1033-1038.

[8] Li, H., Guo, H., Tong, S., Huang, K., Zhang, C., Wang, X., ... & Yang, J. (2019). High-performance supercapacitor carbon electrode fabricated by large-scale roll-to-roll micro-gravure printing. *Journal of Physics D: Applied Physics*, *52*(11), 115501.

[9] Sandström, A., Dam, H. F., Krebs, F. C., & Edman, L. (2012). Ambient fabrication of flexible and large-area organic light-emitting devices using slot-die coating. *Nature communications*, *3*(1), 1-5.

[10] Furukawa, T., & Koden, M. (2017). Novel Roll-to-Roll Deposition and Patterning of ITO on Ultra-Thin Glass for Flexible OLEDs. *IEICE Transactions on Electronics*, *100*(11), 949-954.

[11] Jung, E., Kim, C., Kim, M., Chae, H., Cho, J. H., & Cho, S. M. (2017). Roll-to-roll preparation of silver-nanowire transparent electrode and its application to large-area organic light-emitting diodes. *Organic Electronics*, *41*, 190-197.

[12] Sim, H., Kim, C., Bok, S., Kim, M. K., Oh, H., Lim, G. H., ... & Lim, B. (2018). Five-minute synthesis of silver nanowires and their roll-to-roll processing for large-area organic light emitting diodes. *Nanoscale*, *10*(25), 12087-12092.

[13] Krebs, F. C., Tromholt, T., & Jørgensen, M. (2010). Upscaling of polymer solar cell fabrication using full roll-to-roll processing. *Nanoscale*, *2*(6), 873-886.

[14] Park, Y. S., & Kim, H. K. (2010). Flexible indium zinc oxide/Ag/indium zinc oxide multilayer electrode grown on polyethersulfone substrate by cost-efficient roll-to-roll sputtering for flexible organic photovoltaics. *Journal of Vacuum Science & Technology A: Vacuum, Surfaces, and Films*, *28*(1), 41-47.

[15] Søndergaard, R., Hösel, M., Angmo, D., Larsen-Olsen, T. T., & Krebs, F. C. (2012). Roll-to-roll fabrication of polymer solar cells. *Materials today*, *15*(1-2), 36-49.

[16] Griffith, M. J., Cooling, N. A., Vaughan, B., Elkington, D. C., Hart, A. S., Lyons, A. G., ... & Dastoor, P. C. (2015). Combining printing, coating, and vacuum deposition on the roll-to-roll scale: a hybrid organic photovoltaics fabrication. *IEEE Journal of Selected Topics in Quantum Electronics*, *22*(1), 112-125.

[17] Hwang, K., Jung, Y. S., Heo, Y. J., Scholes, F. H., Watkins, S. E., Subbiah, J., ... & Vak, D. (2015). Toward large scale roll-to-roll production of fully printed perovskite solar cells. *Advanced materials*, *27*(7), 1241-1247.

[18] Jung, M., Kim, J., Noh, J., Lim, N., Lim, C., Lee, G., ... & Cho, G. (2010). All-printed and roll-to-roll-printable 13.56-MHz-operated 1-bit RF tag on plastic foils. *IEEE Transactions on Electron Devices*, *57*(3), 571-580.

[19] Zichner, R., & Baumann, R. R. (2013). Roll-to-roll screen printed radio frequency identification transponder antennas for vehicle tracking systems. *Japanese Journal of Applied Physics*, *52*(5S1), 05DC24.

[20] Wi, J. S., Lee, S., Lee, S. H., Oh, D. K., Lee, K. T., Park, I., ... & Ok, J. G. (2017). Facile three-dimensional nanoarchitecturing of double-bent gold strips on roll-to-roll nanoimprinted transparent nanogratings for flexible and scalable plasmonic sensors. *Nanoscale*, *9*(4), 1398-1402.

[21] Bariya, M., Shahpar, Z., Park, H., Sun, J., Jung, Y., Gao, W., ... & Javey, A. (2018). Roll-to-roll gravure printed electrochemical sensors for wearable and medical devices. *ACS nano*, *12*(7), 6978-6987.

[22] Park, J., Nam, D., Park, S., & Lee, D. (2018). Fabrication of flexible strain sensors via roll-to-roll gravure printing of silver ink. *Smart Materials and Structures*, *27*(8), 085014.

[23] Jeong, H., Noh, Y., & Lee, D. (2019). Highly stable and sensitive resistive flexible humidity sensors by means of roll-to-roll printed electrodes and flower-like TiO2 nanostructures. *Ceramics International*, *45*(1), 985-992.

[24] Lee, S. H., & Lee, S. (2019). Fabrication and Characterization of Roll-to-Roll Printed Air-Gap Touch Sensors. *Polymers*, *11*(2), 245.

[25] Lee, S. H., & Lee, S. (2020). Cantilever Type Acceleration Sensors Made by Roll-to-Roll Slot-Die Coating. *Sensors*, *20*(13), 3748.

[26] Lee, S. H., & Lee, S. (2020). Fabrication and Characterization of Roll-to-Roll-Coated Cantilever-Structured Touch Sensors. *ACS Applied Materials & Interfaces*, *12*(41), 46797-46803.

[27] Liedert, C., Rannaste, L., Kokkonen, A., Huttunen, O. H., Liedert, R., Hiltunen, J., & Hakalahti, L. (2020). Roll-to-roll manufacturing of integrated immunodetection sensors. *ACS sensors*, *5*(7), 2010-2017.

[28] Gagliardi, Margareth. (2019, May). *Global Markets for Roll-to-roll Technologies for Flexible Devices*. BCC Research database: SMC082C.

[29] Morse, J. (2012). Accelerating Progress for Advanced Manufacturing: Enabling Technologies, Barriers, Infrastructure, and Partnership Models for Roll-to-Roll Nanofabrication. *NNN Newsletter*, *5*(6).

[30] Huang, Y., Chen, J., Yin, Z., & Xiong, Y. (2011). Roll-to-roll processing of flexible heterogeneous electronics with low interfacial residual stress. *IEEE Transactions on Components, Packaging and Manufacturing Technology*, *1*(9), 1368-1377.

[31] Feng, D., & Raman, A. (2019). Thermomechanics of axially moving webs in roll-to-roll manufacturing processes. *International Journal of Heat and Mass Transfer*, *129*, 1317-1327.

[32] Dumont, P., Tornare, G., Leterrier, Y., & Månson, J. A. (2007). Intrinsic, thermal and hygroscopic residual stresses in thin gas-barrier films on polymer substrates. *Thin Solid Films*, *515*(19), 7437-7441.

[33] Sun, L., Qin, G., Huang, H., Zhou, H., Behdad, N., Zhou, W., & Ma, Z. (2010). Flexible high-frequency microwave inductors and capacitors integrated on a polyethylene terephthalate substrate. *Applied Physics Letters*, *96*(1), 013509.

[34] Koç, H., Knittel, D., De Mathelin, M., & Abba, G. (2002). Modeling and robust control of winding systems for elastic webs. *IEEE Transactions on control systems technology*, *10*(2), 197-208.

[35] Jeong, J., Gafurov, A. N., Park, P., Kim, I., Kim, H., Kang, D., ... & Lee, T. M. (2021). Tension Modeling and Precise Tension Control of Roll-to-Roll System for Flexible Electronics. *Flexible and Printed Electronics*, *6*, 015005

[36] Schultheis, F. (2007). *U.S. Patent Application No. 11/175,628*.

[37] Linna, H., Parola, M., & Virtanen, J. (2001). Better productivity by measuring web tension profile. In *55th Appita Annual Conference, Hobart, Australia 30 April-2 May 2001: Proceedings* (p. 305). Appita Inc.

[38] Eriksson, L. (1978). *U.S. Patent No. 4,109,520*. Washington, DC: U.S. Patent and Trademark Office.

[39] Strom, V. E., Johansson, B. L. I., & Karlsson, H. I. (1987). *U.S. Patent No. 4,655,093*. Washington, DC: U.S. Patent and Trademark Office.

[40] Vedrines, M., Gassmann, V., & Knittel, D. (2008). Moving web-tension determination by out-of-plane vibration measurements using a laser. *IEEE Transactions on Instrumentation and Measurement*, *58*(1), 207-213.

[41] Ma, L., Chen, J., Tang, W., & Yin, Z. (2017). Vibration-based estimation of tension for an axially travelling web in roll-to-roll manufacturing. *Measurement Science and Technology*, *29*(1), 015102.

[42] Yan, J., & Du, X. (2020). Real-time web tension prediction using web moving speed and natural vibration frequency. *Measurement Science and Technology*, *31*(11), 115205.

[43] Raman, A., Wolf, K. D., & Hagedorn, P. (2001). Observations on the vibrations of paper webs. *Proceedings of 11th Annual Symposium on Information Storage and Processing Systems*, Santa Clara, CA, June 10–13, pp. 415–429.

[44] Vaughan, M., & Raman, A. (2010). Aeroelastic stability of axially moving webs coupled to incompressible flows. *Journal of Applied Mechanics*, *77*(2).

[45] Feng, D., Wang, J., Chiu, G. T. C., & Raman, A. (2021). Vibrations of air-coupled web systems. *Journal of Vibration and Acoustics*, *143*(1): 011004.

[46] Jin, Y., Chen, J., & Yin, Z. (2020). Web Tension Estimation by Local Contact Force Measurement in Roll-to-Roll Manufacturing. *International Journal of Precision Engineering and Manufacturing*, *21*(11), 2067-2075.

[47] Palavesam, N., Marin, S., Hemmetzberger, D., Landesberger, C., Bock, K., & Kutter, C. (2018). Roll-to-roll processing of film substrates for hybrid integrated flexible electronics. *Flexible and Printed Electronics*, *3*(1), 014002.

[48] Wickert, J. A., & Mote Jr, C. D. (1990). Classical vibration analysis of axially moving continua. *ASME Journal of Applied Mechanics*, *57*(3): 738–744.

[49] Ulsoy, A. G., & Mote Jr, C. D. (1982). Vibration of wide band saw blades. *ASME Journal of Manufacturing Science and Engineering*, *104*(1): 71-78.

[50] Turnbull, P. F., Perkins, N. C., & Schultz, W. W. (1995). Contact-induced nonlinearity in oscillating belts and webs. *Journal of Vibration and Control*, *1*(4), 459-479.

[51] DuPont Teijin Films, Mylar Physical Properties. (2021, February 3). Retrieved from http://usa.dupontteijinfilms.com/wp-content/uploads/2017/01/Mylar_Physical_Properties.pdf

[52] Wilson, I., Ladizesky, N. H., & Ward, I. M. (1976). The determination of Poisson's ratio and extensional modulus for polyethylene terephthalate sheets by an optical technique. *Journal of Materials Science*, *11*(12), 2177-2180.

[53] Timoshenko, S. P., & Woinowsky-Krieger, S. (1959). *Theory of plates and shells*. McGraw-hill.

[54] Kármán, T. V. (1907). Festigkeitsprobleme im maschinenbau. In *Mechanik* (pp. 311-385). Vieweg+ Teubner Verlag, Wiesbaden.

[55] Czernia, D., & Szyk, B., Air Density Calculator. (2021, February 3). Retrieved from https://www.omnicalculator.com/physics/air-density

5. CONCLUSIONS AND FUTURE DIRECTIONS

5.1 Conclusions

In this dissertation, we investigated multi-physics problems of R2R processes for flexible devices including the in-plane thermomechancs of axially moving webs, the vibrations of air-coupled web systems, and the methods for nonuniform web tension measurements. We expect these analyses could benefit the process control and product quality to improve the development of low-cost and high-throughput manufacturing of flexible devices with maximize device yields.

In Chapter 2, we theoretically develop and experimentally validate an accurate thermomechanics model of an axially moving web subjecting to arbitrary heat flux. We study the cases for both in air R2R and *in vacuo* R2R processes. The web transport significantly influences the temperature and stress distribution. With a fixed heat flux, the magnitudes of peak temperature and compressive stress decrease when increasing web line speed. With the help of this model, process designer can adjust the laser power and web line speed to control the local web temperature and local web wrinkling in a workable range for the process.

In Chapter 3, we develop closed-form, semi-analytical, universal hydrodynamic functions to predict the lowest symmetric and anti-symmetric mode frequencies to within 10% across all the measurements with three different materials, two different applied tensions, and four different web aspect ratios representing materials, tensions, and aspect ratios commonly found in R2R flexible devices manufacturing. They provide R2R process designers a convenient way to predict the lowest frequencies of air-coupled web system without the need to resort to computationally intensive methods. The air-coupling significantly affects the web frequencies and reduces them from 20% to 60% compared to those *in vacuo* and separates the clustered frequencies. It also changes the eigenmodes of webs by cross coupling various *in vacuo* modes which are experimentally validated. These are caused by the off-diagonal terms in the added air mass matrix.

In Chapter 4, we develop and cross validate an NCR method and a GCSM method to measure the average web tension and its linear variation. The NCR method measures the average tension and its linear variation with a closed-form expression of the lowest symmetric and antisymmetric frequencies. It shows that that the lowest symmetric frequency and increases the lowest antisymmetric frequency separate and the symmetric and antisymmetric basis functions are

coupled when the tension is linearly variated. The GCSM method measures them from local contact stiffness by nonlinear regression. Both the two methods are in-expensive and friendly to adapt to different spans with different web path flexibly without the needs of new calibration. The two method are experimentally cross validated with 3.43% discrepancy in the average web tension and 4.12% discrepancy in the linear variation of tension when there is no local wrinkling. In addition, we in-line measure the tension distribution in two spans of a commercial R2R system under three different line speeds, respectively. The two spans in a same R2R system can have different average tension and different linear variation of tension. In the commercial R2R system we tested, the cross-span linear variation can be up to 35.58%.

5.2 Future Research Directions

Although we have discussed many aspects of multi-physics analysis of thin webs in R2R manufacturing for flexible devices, additional research is needed to improve the process stability and product quality. Future topics for research include the following:

1. The thermomechanics solver we used in Chapter 2 can be used to solve the reaction region and depth of heat /leaser annealing zone. Such information provides tools to direct and predict the selective carbonization of polymers [1], directional crystallization of polymers [2], and self-assembly of block copolymers [3].
2. The acoustics excitation we used in Chapters 3 and 4 is invalid for the *in vacuo* R2R processes, where photothermal excitation could be an alternative method. Photothermal excitation has been used in micro-electrical mechanical systems [4, 5] and in atomic force microscopy [6-8], however more works need to be done to find an efficient way to excite those high width to thickness ratio thin webs used in R2R processes with high signal to noise ratio. Some locally pre-coated strips on the thin web may work to enhance the through thickness temperature gradient.
3. We have developed two methods to measure the linearly variation of tension in tensioned webs. Photoelasticity could be used to measure the nonlinear tension or the local stress of a web. Previous tests have been done recently with two commonly used web materials in R2R processes for flexible devices, which are PET [9] and polyimide [10]. Such research projects could be done for the in-line test in a R2R system and be validated with the two method we discussed in Chapter 4. It is also worth to measure the variation of

cross-width performance of flexible products after being cut for assembly and compare with the nonuniform tension.

4. Bending and torsional tests are used to measure the products' fatigue life. Existing methods for flexible devices are using either off-line [11] or contact [12] approach. The off-line approach cannot provide feedback to the R2R control systems efficiently. While the contact approach may not be accurate since the contacts may change the test results. Our studies of air-coupled web vibrations provide a way for in-line noncontact bending and torsional test for R2R manufacturing.

5.3 References

[1] In, J. B., Hsia, B., Yoo, J. H., Hyun, S., Carraro, C., Maboudian, R., & Grigoropoulos, C. P. (2015). Facile fabrication of flexible all solid-state micro-supercapacitor by direct laser writing of porous carbon in polyimide. *Carbon, 83*, 144-151.

[2] Ye, C., Wang, C., Wang, J., Wiener, C. G., Xia, X., Cheng, S. Z., ... & Vogt, B. D. (2017). Rapid assessment of crystal orientation in semi-crystalline polymer films using rotational zone annealing and impact of orientation on mechanical properties. *Soft matter, 13*(39), 7074-7084.

[3] Albert, J. N., & Epps III, T. H. (2010). Self-assembly of block copolymer thin films. *Materials Today, 13*(6), 24-33.

[4] Thornton, K. E. B., Uttamchandani, D., & Culshaw, B. (1988). Novel optically excited resonant pressure sensor. *Electronics Letters*, *24*(10), 573-574.

[5] Liu, Y. M., Liu, J., & Zhu, C. (2000, October). Performance of optically excited silicon microresonators with coating film. In *Advanced Photonic Sensors: Technology and Applications* (Vol. 4220, pp. 221-225). International Society for Optics and Photonics.

[6] Umeda, N., Ishizaki, S., & Uwai, H. (1991). Scanning attractive force microscope using photothermal vibration. *Journal of Vacuum Science & Technology B: Microelectronics and Nanometer Structures Processing, Measurement, and Phenomena*, *9*(2), 1318-1322.

[7] Kiracofe, D., Kobayashi, K., Labuda, A., Raman, A., & Yamada, H. (2011). High efficiency laser photothermal excitation of microcantilever vibrations in air and liquids. *Review of Scientific Instruments*, *82*(1), 013702.

[8] Wagner, R., & Killgore, J. P. (2015). Photothermally excited force modulation microscopy for broadband nanomechanical property measurements. *Applied physics letters*, *107*(20), 203111.

[9] Prasath, R. G. R., Newton, T., & Danyluk, S. (2018). Stress monitoring of PET beverage bottles by Digital Photoelasticity. *Manufacturing Letters*, *15*, 9-13.

[10] Gao, G., Mao, D., Jiang, R., Li, Z., Liu, X., Lei, B., ... & Fan, B. (2020). Investigation of photoelastic property and stress analysis for optical polyimide membrane through stress birefringence method. *Coatings*, *10*(1), 56.

[11] Finn III, M., Martens, C. J., Zaretski, A. V., Roth, B., Søndergaard, R. R., Krebs, F. C., & Lipomi, D. J. (2018). Mechanical stability of roll-to-roll printed solar cells under cyclic bending and torsion. *Solar Energy Materials and Solar Cells*, *174*, 7-15.

[12] Palavesam, N., Marin, S., Hemmetzberger, D., Landesberger, C., Bock, K., & Kutter, C. (2018). Roll-to-roll processing of film substrates for hybrid integrated flexible electronics. *Flexible and Printed Electronics*, *3*(1), 014002.

APPENDIX A. FEM INCLUDING NONLINEAR TEMPERATURE AND DEFORMATION COUPLING TERM

Including nonlinear temperature and deformation coupling term in the FEM solver, we rewrite the governing equations (2.14), (2.15), and (2.17) in matrix-vector form for finite element analysis as

$$[K_{1\_u1}]_{m\times m}\{u_1\}_{m\times 1}+[K_{1\_u3}]_{m\times m}\{u_3\}_{m\times 1}+[K_{1\_T}]_{m\times m}\{T\}_{m\times 1}=0, \tag{A.1}$$

$$[K_{2\_u1}]_{m\times m}\{u_1\}_{m\times 1}+[K_{2\_u3}]_{m\times m}\{u_3\}_{m\times 1}+[K_{2\_T}]_{m\times m}\{T\}_{m\times 1}=0, \tag{A.2}$$

$$\underbrace{[K_{Tu1}]_{m\times m}\{Tu_1\}_{m\times 1}}_{\text{term 1}}+[K_{Tu3}]_{m\times m}\{Tu_3\}_{m\times 1}+\underbrace{[K_{cond\_T}]_{m\times m}\{T\}_{m\times 1}}_{\text{term 2}}+\underbrace{[K_{conv\_T}]_{m\times m}\{T\}_{m\times 1}}_{\text{term 3}}+\underbrace{[K_{rad\_T}]_{m\times m}\{T^4\}_{m\times 1}}_{\text{term 4}}=\{F\}_{m\times 1}=\{Q_{flux}\}_{m\times 1}+\{Q_{conv}\}_{m\times 1}+\{Q_{rad}\}_{m\times 1}, \tag{A.3}$$

where the elements of stiffness matrices $[K_{Tu1}]$ and $[K_{Tu3}]$ are

$$[K_{Tu1}^{(e)}]=-\{N\}_{,1}\frac{E}{1-\upsilon}\alpha_T U_1^*\{N\}_{,1}^{\ T};[K_{Tu3}^{(e)}]=-\{N\}_{,3}\frac{E}{1-\upsilon}\alpha_T U_1^*\{N\}_{,1}^{\ T}. \tag{A.4}$$

The convection coefficient under each speed in term 3 is chosen as the average of nonlinear fitted convection coefficients from 300 K to 700 K. Figure A.1. shows the contribution percentage to peak temperature by each term in Eq. (A.3) under the heat flux as shown in Figure 2.2(a). The following are the conclusions from Figure A.1.:

1. The nonlinear temperature and deformation coupling term (term 1) is negligible compared with other terms no matter in which web speed.
2. The contribution of conductivity term (term 2) grows with increasing web speed, since the internal convection part is directly proportional to web speed as shown in Eq. (2.22).
3. The contribution of thermal radiation term (term 4) decreases with web speed increasing because the contributions from internal and external convection through terms 2 and term 3 increase with transport speed.

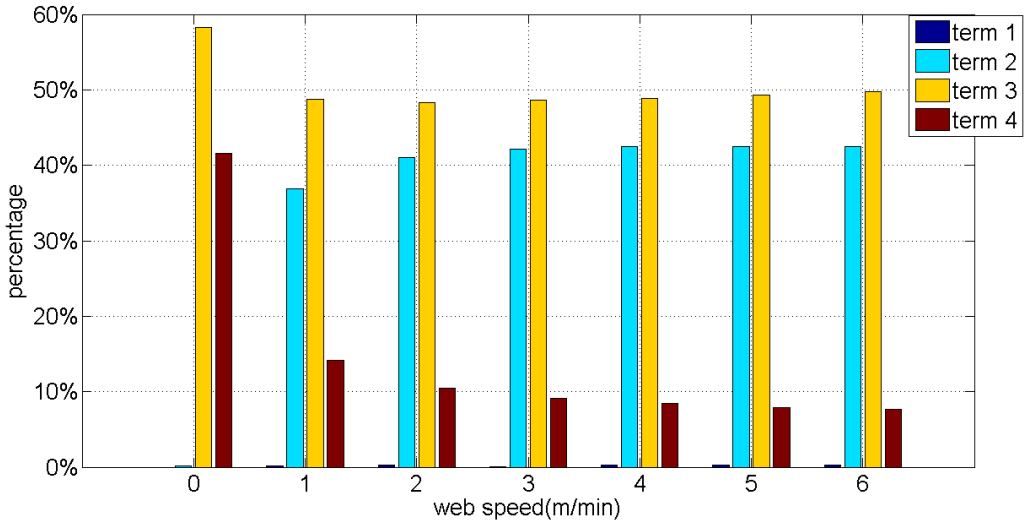

Figure A.1. Contribution percentage to peak temperature by each term in Eq. (A.3) under different web speeds. Term 1 is the nonlinear temperature and deformation coupling term. Term 2 is conductivity term, including heat conduction and internal convection. Term 3 is convection term, describing the convective heat transfer between web and gas (external convection). Term 4 is the radiation term.

APPENDIX B. FREE CONVECTION AND FORCED CONVECTION

Both free convection and forced convection should be involved in the model. An indication of the relative importance of free and forced convection is determined as: Free convection is dominant if $Gr / Re^2 >> 1$ and can be neglected when $Gr / Re^2 << 1$. Both free and forced convection should be taken into account if $Gr / Re^2 \approx 1$ [1]. Grashof number Gr represents the ratio of buoyancy force to viscous force. Reynolds number Re represents the ratio of inertial force to viscous force:

$$Gr = \frac{g(T - T_a)L_{ch}{}^3}{T_{bl}\tilde{\upsilon}_a{}^2}, \tag{B.1}$$

$$Re = \frac{U_1^* L_{ch}}{\tilde{\upsilon}_a}. \tag{B.2}$$

From Eqs. (2.23), (B.1), and (B.2), we obtain

$$Gr / Re^2 = \frac{2g(T - T_a)L_{ch}}{(T + T_a)U_1^{*2}}. \tag{B.3}$$

Choosing T_{bl} = 60 °C, T_a = 25 °C, g = 9.8 m/s^2, b = 75 mm, Figure B.1. shows the values of free, forced convection coefficients and the Gr/Re^2 ratio under various web speeds. In the range of web speed, we discuss in Chapter 2, both free and forced convection should be taken into account.

Reference

[1] Bergman, T. L., Incropera, F. P., DeWitt, D. P., & Lavine, A. S. (2011). *Fundamentals of heat and mass transfer*. John Wiley & Sons.

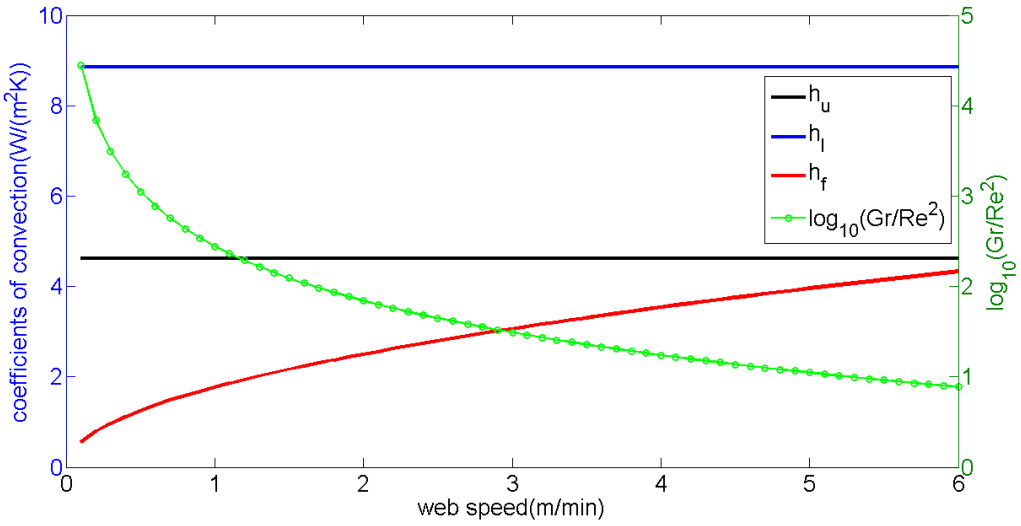

Figure B.1. The values of free convection coefficients on the upper and lower surface h_u (black line), h_l (blue line), forced convection coefficient on one side of the web h_f (red line), and Gr / Re^2 ratio (the logarithm of the ratio is shown as the green line with circles) at different web speeds. Free convection is dominant if $Gr / Re^2 >> 1$, forced convection is dominant if $Gr / Re^2 << 1$.

APPENDIX C. DERIVATION OF NCR METHOD

We assume the surrounding air is initially quiescent (no bulk velocity or transport), and is incompressible, inviscid, and irrotational to choose a 3D potential flow theory for the aerodynamics of it. The surface pressure differential between the bottom surface and upper surface of the vibrating web [1-3]

$$P(x_1, x_3, \tau) = 2\rho_{air}\dot{\phi}(x_1, 0^+, x_3, \tau), \tag{C.1}$$

where the factor "2" comes from the anti-symmetric aerodynamic pressure on the bottom surface and upper surface; ρ_{air} is the air density (we choose $\rho_{air} = 0$ for the *in vacuo* R2R processes); $\phi(x_1, 0^+, x_3, \tau)$ is the velocity potential of air on the web. Substituting Eq. (C.1) into Eq. (4.3), the governing equation for the air-coupled web system is

$$\rho_{web}\ddot{w}(x_1, x_3, \tau) + D\nabla^4 w(x_1, x_3, \tau) - N_{11}^{ave}\left(1 + \sigma\frac{2x_3}{b}\right)w_{,11}(x_1, x_3, \tau) = 2\rho_{air}\dot{\phi}(x_1, 0^+, x_3, \tau). \tag{C.2}$$

The aerodynamics of surrounding air follows the continuity equation

$$\nabla^2\phi(x_1, x_2, x_3, \tau) = \frac{\partial^2\phi(x_1, x_2, x_3, \tau)}{\partial x_1^2} + \frac{\partial^2\phi(x_1, x_2, x_3, \tau)}{\partial x_2^2} + \frac{\partial^2\phi(x_1, x_2, x_3, \tau)}{\partial x_3^2} = 0, \tag{C.3}$$

where ∇^2 is the Laplace operator, $\phi(x_1, x_2, x_3, \tau)$ is the 3D velocity potential of surrounding air. The air velocity on the web surface and normal to the web is identical to that of the vibrating web

$$-\phi_{,2}(x_1, 0^+, x_3, \tau) = \dot{w}(x_1, x_3, \tau). \tag{C.4}$$

We nondimensionalize the governing equations using the definitions

$$\begin{aligned} &x_1' = \frac{x_1}{L}, x_2' = \frac{x_2}{L}, w' = \frac{w}{L}, x_3' = \frac{x_3}{L}, \kappa \equiv \frac{L}{b}, \\ &\varepsilon = \frac{D}{L^2 N_{11}^{ave}}, \Lambda = \frac{L\rho_{air}}{\rho_{web}}, \tau' = \frac{\tau}{L}\sqrt{\frac{N_{11}^{ave}}{\rho_{web}}}, \phi' = \frac{\phi}{L}\sqrt{\frac{\rho_{web}}{N_{11}^{ave}}}, \end{aligned} \tag{C.5}$$

where κ is the in-span length to width ratio (i.e. aspect ratio) of web, ε is the bending stiffness to tension ratio, Λ is a measure of air density to areal mass density of web, the primes denote the nondimensional quantities. Thus, the nondimensional forms of Eqs. (4.4), (4.5), (C.2) - (C.4) are

$$w'(0, x_3', \tau') = w'(1, x_3', \tau') = 0, w_{,11}'(0, x_3', \tau') = w_{,11}'(1, x_3', \tau') = 0; \tag{C.6}$$

$$w'_{,33}(x'_1,\pm 1/(2\kappa),\tau')+\upsilon w'_{,11}(x'_1,\pm 1/(2\kappa),\tau)=0,$$
$$w'_{,333}(x'_1,\pm 1/(2\kappa),\tau')+(2-\upsilon)w'_{,311}(x'_1,\pm 1/(2\kappa),\tau')=0; \tag{C.7}$$

$$\ddot{w}'(x'_1,x'_3,\tau')+\varepsilon\nabla^4 w'(x'_1,x'_3,\tau')-(1+2\kappa\sigma x'_3)w'_{,11}(x'_1,x'_3,\tau')=2\Lambda\dot{\phi}'(x'_1,0^+,x'_3,\tau'); \tag{C.8}$$

$$\nabla^2\phi'(x'_1,x'_2,x'_3,\tau')=0; \tag{C.9}$$

$$-\phi'_{,2}(x'_1,0^+,x'_3,\tau')=\dot{w}'(x'_1,x'_3,\tau'). \tag{C.10}$$

The boundary conditions for the 3D air are

1. the air can exchange outside the area of web, *i.e.* the web is unbaffled

$$\phi'(x'_1,0,x'_3,\tau')=0; \tag{C.11}$$

2. the air is stationary in the far field

$$\lim_{\sqrt{x_1'^2+x_2'^2+x_3'^2}\to\infty}\phi'_{,normal}(x'_1,x'_2,x'_3,\tau')=0. \tag{C.12}$$

Eqs. (C.8) - (C.10) are discretized using Assumed Modes Method (AMM) with the separable forms

$$w'(x'_1,x'_3,\tau')=\sum_{m=1}^{\infty}\sum_{n=1}^{\infty}q'_{mn}(\tau')W'_{mn}(x'_1,x'_3), \tag{C.13}$$

$$\phi'(x'_1,x'_2,x'_3,\tau')=\sum_{m=1}^{\infty}\sum_{n=1}^{\infty}A'_{mn}(\tau')\varphi'_{mn}(x'_1,x'_2,x'_3). \tag{C.14}$$

where $W'_{mn}(x'_1,x'_3)$ is the nondimensional admissible basis functions for web vibration and normalized as $\int_{-1/(2\kappa)}^{1/(2\kappa)}\int_0^1 W'^2_{mn}(x'_1,x'_3)dx'_1dx'_3=1$, $q'_{mn}(\tau')$ is the generalized coordinate, m and n are their notations along longitudinal and lateral directions, respectively. The odd-numbered m and n values describe symmetric basis functions with respect to $x'_1=0.5$ and $x'_3=0$, respectively; while the even-numbered ones correspond to anti-symmetric basis functions with respect to $x'_1=0.5$ and $x'_3=0$, respectively. φ'_{mn} is the velocity potential with respect to web vibration in the corresponding basis function $W'_{mn}(x'_1,x'_3)$. We do not include initial cross flow along longitudinal or lateral direction in this model [2, 3]. Substituting Eqs. (C.13) and (C.14) into Eq. (C.10) yields

$$A'_{mn}(\tau')=-\dot{q}'_{mn}(\tau'), \tag{C.15}$$

$$\varphi'_{mn,2}(x'_1,0^+,x'_3)=W'_{mn}(x'_1,x'_3). \tag{C.16}$$

We combine Eqs. (C.2), (C.13) - (C.16) and apply AMM with inner products with W'_{mn}

$$(\mathbf{I} + 2\Lambda\mathbf{M}'_{air})\ddot{\mathbf{q}}' + (\mathbf{K}'_{web} + \sigma\mathbf{K}'_{\sigma})\mathbf{q}' = 0, \tag{C.17}$$

where

$$(\mathbf{M}'_{air})_{ij;mn} = \int_{-1/(2\kappa)}^{1/(2\kappa)} \int_0^1 W'_{ij}(x'_1, x'_3)\varphi'_{mn}(x'_1, 0^+, x'_3)dx'_1dx'_3. \tag{C.18}$$

$$\begin{aligned}(\mathbf{K}'_{web})_{ij;mn} = \int_{-1/(2\kappa)}^{1/(2\kappa)} \int_0^1 \{&\varepsilon[W'_{ij,11}(x'_1, x'_3)W'_{mn,11}(x'_1, x'_3) + W'_{ij,33}(x'_1, x'_3)W'_{mn,33}(x'_1, x'_3) \\ &+2(1-\upsilon)W'_{ij,13}(x'_1, x'_3)W'_{mn,13}(x'_1, x'_3) + \upsilon W'_{ij,11}(x'_1, x'_3)W'_{mn,33}(x'_1, x'_3) \\ &+\upsilon W'_{ij,33}(x'_1, x'_3)W'_{mn,11}(x'_1, x'_3)] + W'_{ij,1}(x'_1, x'_3)W'_{mn,1}(x'_1, x'_3)\}dx'_1dx'_3,\end{aligned} \tag{C.19}$$

$$(\mathbf{K}'_{\sigma})_{ij;mn} = \int_{-1/(2\kappa)}^{1/(2\kappa)} \int_0^1 2\kappa x'_3 W'_{ij,1}(x'_1, x'_3)W'_{mn,1}(x'_1, x'_3)dx'_1dx' \tag{C.20}$$

$\mathbf{M}'_{air}$ is the added air mass matrix [3], which is zero for the *in vacuo* R2R processes. $\mathbf{q}'$ is the vector of the generalized coordinates $q'_{mn}(\tau')$. $\mathbf{K}'_{web}$ and $\mathbf{K}'_{\sigma}$ are the stiffness matrices corresponding to the average web tension and σ, respectively.

Based on the convergence study we presented in our previous works in Chapter 2 [3], we start from 4×4 AMM with polynomial admissible function basis to find the analytical formulas that relate f_{11} and f_{12} to N_{11}^{ave} and σ. We choose an orthogonal set of admissible basis functions

$$\begin{aligned}W'_{11} &= \sqrt{2\kappa}\sin(\pi x'_1), \\ W'_{12} &= \sqrt{24\kappa}\sin(\pi x'_1)\kappa x'_3, \\ W'_{13} &= 6\sqrt{10\kappa}\sin(\pi x'_1)(-\kappa^2 x'^2_3 + \frac{1}{12}), \\ W'_{14} &= 20\sqrt{14\kappa}\sin(\pi x'_1)(-\kappa^3 x'^3_3 + \frac{3\kappa x'_3}{20}).\end{aligned} \tag{C.21}$$

We substitute Eq. (C.21) into Eq. (C.17) and obtain

$$\mathbf{M}'^{(4\times4)}_{air} = \begin{bmatrix} 0.25524F_{1111}(\kappa) & 0 & 0.07000F_{1113}(\kappa) & 0 \\ 0 & 0.13075F_{1212}(\kappa) & 0 & 0.05354F_{1214}(\kappa) \\ 0.07000F_{1113}(\kappa) & 0 & 0.10435F_{1313}(\kappa) & 0 \\ 0 & 0.05354F_{1214}(\kappa) & 0 & 0.08353F_{1414}(\kappa) \end{bmatrix}, \tag{C.22}$$

$$\mathbf{K}_{web}'^{(4\times4)} = \pi^2\mathbf{I}^{(4\times4)} + \pi^4\varepsilon\begin{bmatrix} 1 & 0 & 12\sqrt{5}\upsilon\dfrac{\kappa^2}{\pi^2} & 0 \\ 0 & 1+24(1-\upsilon)\dfrac{\kappa^2}{\pi^2} & 0 & \sqrt{21}(28\upsilon-8)\dfrac{\kappa^2}{\pi^2} \\ 12\sqrt{5}\upsilon\dfrac{\kappa^2}{\pi^2} & 0 & 1+120(1-\upsilon)\dfrac{\kappa^2}{\pi^2}+720\dfrac{\kappa^4}{\pi^4} & 0 \\ 0 & \sqrt{21}(28\upsilon-8)\dfrac{\kappa^2}{\pi^2} & 0 & 1+336(1-\upsilon)\dfrac{\kappa^2}{\pi^2}+8400\dfrac{\kappa^4}{\pi^4} \end{bmatrix}, \tag{C.23}$$

$$\mathbf{K}_{\sigma}'^{(4\times4)} = \pi^2\begin{bmatrix} 0 & \dfrac{1}{\sqrt{3}} & 0 & 0 \\ \dfrac{1}{\sqrt{3}} & 0 & -\dfrac{2}{\sqrt{15}} & 0 \\ 0 & -\dfrac{2}{\sqrt{15}} & 0 & \dfrac{6}{\sqrt{35}} \\ 0 & 0 & \dfrac{6}{\sqrt{35}} & 0 \end{bmatrix}, \tag{C.24}$$

where $F_{ijmn}(\kappa)$'s are the hydrodynamic functions fitted following the derivation we presented in our previous work with κ from 0.1 to 10 [3]. Their formulas are

$$\begin{aligned}
&F_{1111}(\kappa) = 1-1.17557[\log_{10}(\kappa)]-0.10578[\log_{10}(\kappa)]^2+0.54019[\log_{10}(\kappa)]^3 \\
&+0.16507[\log_{10}(\kappa)]^4-0.25226[\log_{10}(\kappa)]^5-0.00822[\log_{10}(\kappa)]^6, \\
&F_{1113}(\kappa) = 1-0.77187[\log_{10}(\kappa)]-0.65329[\log_{10}(\kappa)]^2+1.02506[\log_{10}(\kappa)]^3 \\
&+0.04640[\log_{10}(\kappa)]^4-0.45257[\log_{10}(\kappa)]^5+0.15403[\log_{10}(\kappa)]^6, \\
&F_{1212}(\kappa) = 1-1.91774[\log_{10}(\kappa)]+1.16202[\log_{10}(\kappa)]^2+0.46179[\log_{10}(\kappa)]^3 \\
&-0.82329[\log_{10}(\kappa)]^4-0.19040[\log_{10}(\kappa)]^5+0.38791[\log_{10}(\kappa)]^6, \\
&F_{1214}(\kappa) = 1-1.60774[\log_{10}(\kappa)]+0.85505[\log_{10}(\kappa)]^2+1.36084[\log_{10}(\kappa)]^3 \\
&-1.86201[\log_{10}(\kappa)]^4-0.45147[\log_{10}(\kappa)]^5+0.96468[\log_{10}(\kappa)]^6, \\
&F_{1313}(\kappa) = 1-1.83128[\log_{10}(\kappa)]+1.36260[\log_{10}(\kappa)]^2-0.05659[\log_{10}(\kappa)]^3 \\
&-0.78108[\log_{10}(\kappa)]^4+0.03040[\log_{10}(\kappa)]^5+0.38993[\log_{10}(\kappa)]^6, \\
&F_{1414}(\kappa) = 1-2.05520[\log_{10}(\kappa)]+1.67384[\log_{10}(\kappa)]^2-0.12247[\log_{10}(\kappa)]^3 \\
&-0.73177[\log_{10}(\kappa)]^4+0.02163[\log_{10}(\kappa)]^5+0.31820[\log_{10}(\kappa)]^6.
\end{aligned} \tag{C.25}$$

Air loading couples the symmetric basis functions to each other as shown in $\mathbf{M}'_{air}$, as well as the antisymmetric basis functions. On the other hand, symmetric and antisymmetric basis functions are coupled in $\mathbf{K}'_{\sigma}$ because of the nonuniform tension.

Analytical solutions to the eigenvalue problem with 4×4 AMM are not easily available, however we develop a higher order mass approximation method to obtain an analytical solution with the same accuracy but reduced size. In R2R processes for flexible and printed electronics, the web bending stiffness to tension ratio ε is very small, typically from 10^{-6} to 10^{-4}, so that we assume $\varepsilon\approx0$ and start from the 2×2 AMM with W'_{11} and W'_{12} to solve the eigenvalue problem of Eq. (C.17), and obtain

$$f_{11}^{(W'_{11},W'_{12})}=\sqrt{\frac{N_{11}^{ave}}{8L^2}\left[\left(\frac{1}{M_{11}}+\frac{1}{M_{12}}\right)-\sqrt{\left(\frac{1}{M_{11}}-\frac{1}{M_{12}}\right)^2+\frac{4\sigma^2}{3M_{11}M_{12}}}\right]}\text{(Hz)}, \tag{C.26}$$

$$f_{12}^{(W'_{11},W'_{12})}=\sqrt{\frac{N_{11}^{ave}}{8L^2}\left[\left(\frac{1}{M_{11}}+\frac{1}{M_{12}}\right)+\sqrt{\left(\frac{1}{M_{11}}-\frac{1}{M_{12}}\right)^2+\frac{4\sigma^2}{3M_{11}M_{12}}}\right]}\text{(Hz)}, \tag{C.27}$$

where $M_{11}=\rho_{web}+0.51048L\rho_{air}F_{1111}(\kappa)$, $M_{12}=\rho_{web}+0.26150L\rho_{air}F_{1212}(\kappa)$. Then we apply 2×2 AMM with W'_{11} and W'_{13} for an equivalent value $\bar{M}_{11}$ to update M_{11}

$$\mathbf{M}'^{(W'_{11},W'_{13})}_{air}=\begin{bmatrix}0.25524F_{1111}(\kappa) & 0.07000F_{1113}(\kappa)\\ 0.07000F_{1113}(\kappa) & 0.10435F_{1313}(\kappa)\end{bmatrix}, \tag{C.28}$$

$$\mathbf{K}'^{(W'_{11},W'_{13})}_{web}\approx\pi^2\mathbf{I}^{(2\times2)}, \tag{C.29}$$

$$\mathbf{K}'^{(W'_{11},W'_{13})}_{\sigma}=\mathbf{0}^{(2\times2)}. \tag{C.30}$$

Solving the eigenvalue problem of Eq. (C.17), we obtain

$$f_{11}^{(W'_{11},W'_{13})}=\frac{1}{2L}\sqrt{\frac{N_{11}}{\bar{M}_{11}}}\text{(Hz)}, \tag{C.31}$$

where

$$\begin{aligned}\bar{M}_{11}=\rho_{web}+\frac{L\rho_{air}}{2}&[0.51048F_{1111}(\kappa)+0.20871F_{1313}(\kappa)\\&+\sqrt{(0.51048F_{1111}(\kappa)-0.20871F_{1313}(\kappa))^2+0.07841F_{1113}^2(\kappa)}].\end{aligned} \tag{C.32}$$

Similarly, an equivalent value $\bar{M}_{12}$ from with W'_{12} and W'_{14} is

$$\bar{M}_{12} = \rho_{web} + \frac{L\rho_{air}}{2}[0.26150F_{1212}(\kappa) + 0.16707F_{1414}(\kappa) + \sqrt{(0.26150F_{1212}(\kappa) - 0.16707F_{1414}(\kappa))^2 + 0.04586F_{1214}^2(\kappa)}]. \quad \text{(C.33)}$$

Updating M_{11} and M_{12} by $\bar{M}_{11}$ and $\bar{M}_{12}$ respectively in Eqs. (C.26) and (C.27), we obtain the new frequencies as shown in Eqs (4.6) and (4.7).

Table C.1 shows the convergence study of different AMM orders from Eq. (C.17) and the higher order mass approximation from Eqs. (4.6) and (4.7). We choose a PET web with the same system properties as used in Figure 4.2. Recalling our previous works [3] show that 4×4 AMM with polynomial admissible function basis can accurately predict the lowest two frequencies, we compare the higher order approximation results with 4×4 AMM. In the range of small linear variation of tension with σ from 0 to 0.2, higher order mass approximation estimates f_{11} with less than 1.7% error and f_{12} with less than 2.6% error in comparison to those by 4×4 AMM. When there is a none-zero σ, higher order mass approximation under predicts f_{11} and over predicts f_{12}.

Table C.1. Convergence study of AMM method from Eq. (C.17) with higher order mass approximation from Eqs. (4.6) and (4.7). The web is a PET web with properties $L = 228.6$ mm, $b = 152.4$ mm, $h = 127$ μm, $\rho_{web} = 178.67$ g/m^2, $E = 4.8$ GPa, $\upsilon = 0.33$, $N_{11}^{ave} = 150.47$ N/m, $\rho_{air} = 1.208$ kg/m^3.

σ	0		0.1		0.2	
	f_{11} (Hz)	f_{12} (Hz)	f_{11} (Hz)	f_{12} (Hz)	f_{11} (Hz)	f_{12} (Hz)
1 × 1 AMM	49.81	-	49.81	-	49.81	-
2 × 2 AMM	49.81	56.19	49.45	56.51	48.50	57.33
3 × 3 AMM	48.95	56.19	48.79	55.57	48.26	54.39
4 × 4 AMM	48.95	55.80	48.74	54.47	48.14	54.27
higher order mass	48.71	54.33	48.32	54.68	47.34	55.52

Reference

[1] Raman, A., Wolf, K. D., & Hagedorn, P. (2001). Observations on the vibrations of paper webs. *Proceedings of 11th Annual Symposium on Information Storage and Processing Systems*, Santa Clara, CA, June 10–13, pp. 415–429.

[2] Vaughan, M., & Raman, A. (2010). Aeroelastic stability of axially moving webs coupled to incompressible flows. *Journal of Applied Mechanics*, *77*(2).

[3] Feng, D., Wang, J., Chiu, G. T. C., & Raman, A. (2021). Vibrations of air-coupled web systems. *Journal of Vibration and Acoustics*, *143*(1): 011004.

APPENDIX D. DERIVATION OF GCSM METHOD

To mathematically find the relation between local contact stiffness and web tension distribution, we choose a point load to describe the contact pressure in the linearly elastic model as

$$P(x_1, x_3, \tau) = F\delta(X_1, X_3, \tau), \tag{D.1}$$

where F is the contact force, δ is the Dirac delta function, X_1 and X_3 are the coordinates of the contact location in x_1 and x_3, respectively. Substituting Eq. (D.1) into Eq. (4.3) and evaluating the time derivative to zero give

$$D\nabla^4 W(x_1, x_3) - N_{11}^{ave}\left(1+\sigma\frac{2x_3}{b}\right)W_{,11}(x_1, x_3) = F\delta(X_1, X_3). \tag{D.2}$$

Applying inner products of Eq. (D.2) with a trail function φ_i and the boundary conditions in Eqs. (4.4) and (4.5) to its weak form, we obtain

$$\begin{aligned}&\int_0^L \int_{-\frac{b}{2}}^{\frac{b}{2}} \{D[W_{,11}\varphi_{i,11} + 2\upsilon W_{,11}\varphi_{i,33} + 2(1-\upsilon)W_{,13}\varphi_{i,13} + W_{,33}\varphi_{i,33}] \\ &+ N_{11}^{ave}\left(1+\sigma\frac{2x_3}{b}\right)W_{,1}\varphi_{i,1} - F\delta(X_1, X_3)\varphi_i\} dx_3 dx_1 = 0.\end{aligned} \tag{D.3}$$

We assume the web deflection as shown in Eq. (4.14) and choose two trail functions as

$$\varphi_1 = A_{pq}\sin\frac{p\pi x_1}{L}\sin\frac{(2q-1)\pi x_3}{b}, \tag{D.4}$$

$$\varphi_2 = B_{pq}\sin\frac{p\pi x_1}{L}\cos\frac{(2q-2)\pi x_3}{b}, \tag{D.5}$$

where p and q are the integers from 1 to M and 1 to N, respectively. Substituting Eqs. (4.14) and (D.4) into Eq. (D.3) gives

$$\begin{aligned}&A_{pq}\left\{\frac{D\pi^4}{4b^3L^3}\left[p^2b^2 + (2q-1)^2L^2\right]^2 + \frac{p^2b\pi^2}{4L}N_{11}^{ave}\right\} \\ &+ \frac{2p^2b\sigma N_{11}^{ave}}{L}\sum_{n=1}^{N} B_{pn}\frac{(2q-1)^2 + (2n-2)^2}{\left[(2q-1)^2 - (2n-2)^2\right]^2} = F\sin\frac{p\pi X_1}{L}\sin\frac{(2q-1)\pi X_3}{b},\end{aligned} \tag{D.6}$$

Similarly, substituting Eqs. (4.14) and (D.5) into Eq. (D.3) gives

$$B_{pq}\left\{\frac{\pi^4 D}{4b^3L^3}\left[p^2b^2+(2q-2)^2L^2\right]^2+\frac{p^2b\pi^2}{4L}N_{11}^{ave}\right\}$$
$$+\frac{2p^2b\sigma N_{11}^{ave}}{L}\sum_{n=1}^{N}A_{pn}\frac{(2n-1)^2+(2q-2)^2}{\left[(2n-1)^2-(2q-2)^2\right]^2}=F\sin\frac{p\pi X_1}{L}\cos\frac{(2q-2)\pi X_3}{b}. \quad \text{(D.7)}$$

We combine and rewrite Eqs. (D.6) and (D.7) in a matrix form as Eq. (4.15), where

$$\mathbf{C}_1=\begin{bmatrix} C_1(1) & 0 & 0 & 0 & 0 \\ 0 & \ddots & 0 & 0 & 0 \\ 0 & 0 & C_1(q) & 0 & 0 \\ 0 & 0 & 0 & \ddots & 0 \\ 0 & 0 & 0 & 0 & C_1(N) \end{bmatrix}, \quad \text{(D.8)}$$

$$C_1(q)=\frac{D\pi^4}{4b^3L^3}\left[m^2b^2+(2q-1)^2L^2\right]^2+\frac{m^2b\pi^2}{4L}N_{11}^{ave},$$

$$\mathbf{C}_2=\begin{bmatrix} C_2(1,1) & \cdots & C_2(1,n) & \cdots & C_2(1,N) \\ \vdots & \ddots & \vdots & \iddots & \vdots \\ C_2(q,1) & \cdots & C_2(q,n) & \cdots & C_2(q,N) \\ \vdots & \iddots & \vdots & \ddots & \vdots \\ C_2(N,1) & \cdots & C_2(N,n) & \cdots & C_2(N,N) \end{bmatrix}, \quad \text{(D.9)}$$

$$C_2(q,n)=\frac{2m^2b\sigma N_{11}^{ave}}{L}\frac{(2q-1)^2+(2n-2)^2}{\left[(2q-1)^2-(2n-2)^2\right]^2},$$

$$\mathbf{C}_3=\begin{bmatrix} C_3(1,1) & \cdots & C_3(1,n) & \cdots & C_3(1,N) \\ \vdots & \ddots & \vdots & \iddots & \vdots \\ C_3(q,1) & \cdots & C_3(q,n) & \cdots & C_3(q,N) \\ \vdots & \iddots & \vdots & \ddots & \vdots \\ C_3(N,1) & \cdots & C_3(N,n) & \cdots & C_3(N,N) \end{bmatrix}, \quad \text{(D.10)}$$

$$C_3(q,n)=C_2(n,q),$$

$$\mathbf{C}_4=\begin{bmatrix} C_4(1) & 0 & 0 & 0 & 0 \\ 0 & \ddots & 0 & 0 & 0 \\ 0 & 0 & C_4(q) & 0 & 0 \\ 0 & 0 & 0 & \ddots & 0 \\ 0 & 0 & 0 & 0 & C_4(N) \end{bmatrix}, \quad \text{(D.11)}$$

$$C_4(q)=\frac{\pi^4 D}{4b^3L^3}\left[m^2b^2+(2q-2)^2L^2\right]^2+\frac{m^2b\pi^2}{4L}N_{11}^{ave},$$

$$\mathbf{A}=\left\{A'_{m1}\quad\cdots\quad A'_{mn}\quad\cdots\quad A'_{mN}\right\}^T, \tag{D.12}$$

$$A'_{mn}=\frac{A_{mn}}{F},$$

$$\mathbf{B}=\left\{B'_{m1}\quad\cdots\quad B'_{mn}\quad\cdots\quad B'_{mN}\right\}^T, \tag{D.13}$$

$$B'_{mn}=\frac{B_{mn}}{F},$$

$$\mathbf{C}_5=\left\{C_5(1)\quad\cdots\quad C_5(q)\quad\cdots\quad C_5(N)\right\}^T, \tag{D.14}$$

$$C_5(q)=\sin\frac{(2q-1)\pi X_3}{b},$$

$$\mathbf{C}_6=\left\{C_6(1)\quad\cdots\quad C_6(q)\quad\cdots\quad C_6(N)\right\}^T, \tag{D.15}$$

$$C_6(q)=\cos\frac{(2q-2)\pi X_3}{b}.$$

Once the deflection of a web under the contact force is obtained, we can solve the local contact stiffness as in Eq. (4.16)

To identify the number of M and N, we compare the convergence of web deflection under a known contact force and with known web tension. A same PET web as used in Figure 4.2 is chosen here with the web tension as $N_{11}^{ave}=150.47$ N/m and $\sigma=0$. We choose a contact force $F=0.1$ N applied on the center of the web $(X_1,X_3)=\left(\frac{L}{2},0\right)$ and the center of a free edge $(X_1,X_3)=\left(\frac{L}{2},-\frac{b}{2}\right)$, which are the two critical locations on the web where the maximum number of basis functions may be needed to ensure convergence. We solve A_{mn} and B_{mn} from Eqs. (4.15) and (D.8) - (D.15). Substituting the values of A_{mn} and B_{mn} into Eq. (4.14), we obtain the web deflection. The convergence results with $\sigma\neq 0$ is similar to those with $\sigma=0$, so we choose to only present those with $\sigma=0$ in Table D.1. The deflections in Table D.1 are in the contact locations, which is the maximum local deflections of the web under that contact force. The

discrepancies are from the comparison of deflections with the chosen numbers of M and N to those with $M = 1\text{E}4$ and $N = 1\text{E}4$. We choose the results with discrepancies just under 20%, 15%, 10%, 5%, and 1% and with minimum total number of admissible basis functions ($M \times N$) to present. To make sure the entire is under a 1% discrepancy, we choose $M = 51$ and $N = 18$ in our investigation. However, for the convenience of a R2R process users $M = 3$ and $N = 5$ can also be chosen with a 20% error in their calculations.

Table D.1. Convergence study for GCSM method. Web properties are $L = 228.6$ mm, $b = 152.4$ mm, $\rho_{web} = 178.67$ g/m, $h = 127$ μm, $E = 4.8$ GPa, and $\upsilon = 0.33$. A contact force $F = 0.1$ N is applied on the web with tension $N_{11}^{ave} = 150.47$ N/m and $\sigma = 0$. The deflections are those on the contact locations, which are the maximum deflection of the web.

contact locations	$(X_1, X_3) = (L/2, 0)$		$(X_1, X_3) = (L/2, -b/2)$	
# of basis functions	deflection (mm)	discrepancy	deflection (mm)	Discrepancy
M=3, *N*=5, (15 in total)	1.1409	19.03%	2.0642	19.79%
M=5, *N*=5, (25 in total)	1.2033	14.60%	2.1836	15.15%
M=5, *N*=6, (30 in total)	1.2198	13.43%	2.2119	14.05%
M=9, *N*=6, (54 in total)	1.2775	9.34%	2.3229	9.74%
M=15, *N*=9, (135 in total)	1.3394	4.95%	2.4389	5.23%
M=15, *N*=10, (150 in total)	1.3434	4.66%	2.4462	4.95%
M=51, *N*=17, (867 in total)	1.3952	0.99%	2.5463	1.06%
M=51, *N*=18, (918 in total)	1.3961	0.93%	2.5479	1.00%
M=1E4, *N*=1E4	1.4091	0	2.5736	0

APPENDIX E. SDOF fitting

We obtain the frequencies from frequency response functions by a SDOF fitting. The equation of motion of a damped SDOF system is

$$m\ddot{x} + c\dot{x} + kx = A\cos\omega\tau, \tag{E.1}$$

where m, c, and k are the mass, viscous damping coefficient, and stiffness, respectively. A is the magnitude of harmonic excitation with frequency ω in rad/sec. By assuming the particular solution as

$$x_p(\tau) = X\cos(\omega\tau - \theta), \tag{E.2}$$

where and X is the magnitude of response, θ is the phase between excitation and response, and substituting Eq. (E.2) into Eq. (E.1) we obtain the transfer function G as

$$G = \frac{X}{A} = \frac{1}{\sqrt{(k - m\omega^2)^2 + c^2\omega^2}} = \frac{1/k}{\sqrt{(1 - \frac{\omega^2}{\omega_n^2})^2 + \frac{\omega^2}{Q^2\omega_n^2}}}, \tag{E.3}$$

where $\omega_n = \sqrt{\frac{k}{m}}$ is the nature frequency of the system with a unit rad/sec, $Q = \frac{\sqrt{km}}{c}$ is the quality factor. So that we can rewrite Eq. (E.3) as

$$\frac{1}{G^2} = a_0 + a_2\omega^2 + a_4\omega^4, \tag{E.4}$$

where $a_0 = k^2$, $a_2 = \left(\frac{1}{Q^2} - 2\right)\frac{k^2}{\omega_n^2}$, and $a_4 = \frac{k^2}{\omega_n^4}$. We obtain a_0, a_2, and a_4 by least squares regression in the half-power bandwidth of a peak magnitude in the frequency response functions. So that we can solve the nature frequency and quality factor as

$$\omega_n = \left(\frac{a_0}{a_4}\right)^{\frac{1}{4}} (\text{rad s}^{-1}), \text{ or } f_n = \frac{1}{2\pi}\left(\frac{a_0}{a_4}\right)^{\frac{1}{4}} (\text{Hz}), \tag{E.5}$$

$$Q = \left[a_2\left(a_0 a_4\right)^{-\frac{1}{2}} + 2\right]^{-\frac{1}{2}}. \tag{E.6}$$

The standard error of f_n is

$$\Delta f_n = \left[\left(\frac{\partial f_n}{\partial a_0} \Delta a_0 \right)^2 + \left(\frac{\partial f_n}{\partial a_4} \Delta a_4 \right)^2 \right]^{\frac{1}{2}} = \frac{1}{8\pi} \left[\left(a_0^{-\frac{3}{4}} a_4^{-\frac{1}{4}} \Delta a_0 \right)^2 + \left(a_0^{\frac{1}{4}} a_4^{-\frac{5}{4}} \Delta a_4 \right)^2 \right]^{\frac{1}{2}}, \quad \text{(E.7)}$$

where Δa_0 and Δa_4 can be solved as [1]

$$\Delta a_0 = \left[\sum_i^J \left(a_0 - \frac{1}{G_i^2} + a_2 \omega_i^2 + a_4 \omega_i^4 \right)^2 \right]^{\frac{1}{2}} (J-2)^{-\frac{1}{2}}, \quad \text{(E.8)}$$

$$\Delta a_4 = \left[\sum_i^J \left(a_4 - \frac{1}{G_i^2 \omega_i^4} + \frac{a_0}{\omega_i^4} + \frac{a_2}{\omega_i^2} \right)^2 \right]^{\frac{1}{2}} (J-2)^{-\frac{1}{2}}, \quad \text{(E.9)}$$

J is the total number of data points used in the regression.

Reference

[1] Coleman, H. W., & Steele, W. G. (2018). *Experimentation, validation, and uncertainty analysis for engineers*. John Wiley & Sons.

APPENDIX F. SLIGHTLY NEGATIVE σ^2

It is easy to obtain slightly negative σ^2 (*i.e.* imaginary σ) when the tension is near uniform. From Eq. (4.11), we have

$$\sigma^2 = 3 - \frac{3\left(\bar{M}_{11} + \bar{M}_{12}\right)^2 f_{11}^2 f_{12}^2}{\bar{M}_{11}\bar{M}_{12}\left(f_{11}^2 + f_{12}^2\right)^2}. \tag{F.1}$$

Negative σ^2 yields

$$3 - \frac{3\left(\bar{M}_{11} + \bar{M}_{12}\right)^2 f_{11}^2 f_{12}^2}{\bar{M}_{11}\bar{M}_{12}\left(f_{11}^2 + f_{12}^2\right)^2} < 0. \tag{F.2}$$

We rewrite Eq. (F.2) as

$$(\bar{M}_{11} f_{11}^2 - \bar{M}_{12} f_{12}^2)(\bar{M}_{12} f_{11}^2 - \bar{M}_{11} f_{12}^2) < 0, \tag{F.3}$$

Combining Eqs. (C.32) and (C.33) yields

$$\begin{aligned} &\frac{2\left(\bar{M}_{11} - \bar{M}_{12}\right)}{L\rho_{air}} \\ &= 0.51048F_{1111}(\kappa) + 0.20871F_{1313}(\kappa) - 0.26150F_{1212}(\kappa) - 0.16707F_{1414}(\kappa) \\ &+\sqrt{(0.51048F_{1111}(\kappa) - 0.20871F_{1313}(\kappa))^2 + 0.07841F_{1113}^2(\kappa)} \\ &-\sqrt{(0.26150F_{1212}(\kappa) - 0.16707F_{1414}(\kappa))^2 + 0.04586F_{1214}^2(\kappa)}. \end{aligned} \tag{F.4}$$

We plot the value of $\frac{2\left(\bar{M}_{11} - \bar{M}_{12}\right)}{L\rho_{air}}$ in Figure F.1 with κ from 0.1 to 10 and find that it is always positive in that range, so that

$$\bar{M}_{11} > \bar{M}_{12} \qquad (0.1<\kappa<10). \tag{F.5}$$

On the other hand, we know that $f_{11} \le f_{12}$ from Eqs. (4.6) and (4.7). Hence in the above range

$$\bar{M}_{12} f_{11}^2 - \bar{M}_{11} f_{12}^2 \le 0. \tag{F.6}$$

We substitute Eq. (F.6) into Eq. (F.3) and obtain

$$\bar{M}_{11} f_{11}^2 - \bar{M}_{12} f_{12}^2 > 0. \tag{F.7}$$

So that we rewrite Eq. (F.7) and can obtain negative σ^2 when

$$\frac{f_{11}^2}{f_{12}^2} > \frac{\bar{M}_{12}}{\bar{M}_{11}}. \tag{F.8}$$

The error or uncertainty of frequencies can cause slightly negative σ^2 when the tension is near uniform.

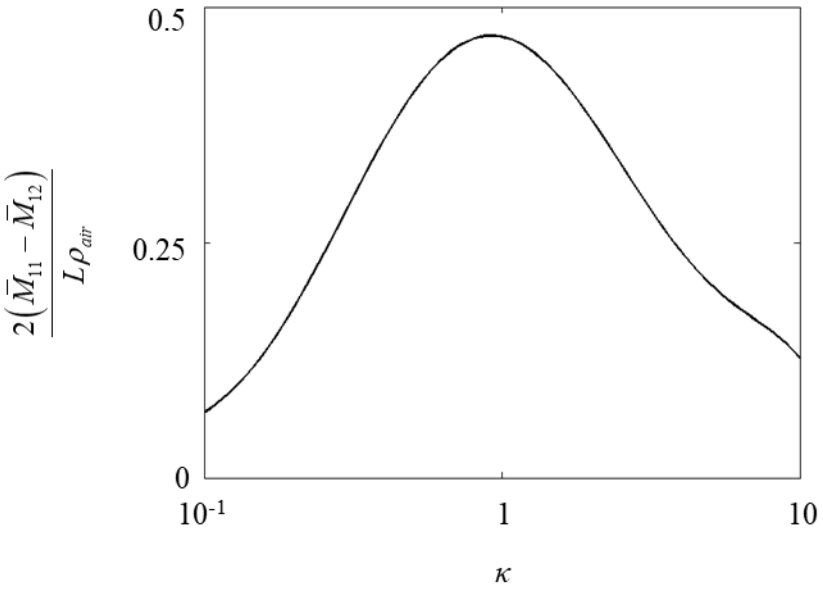

Figure F.1. The value of $\frac{2\left(\bar{M}_{11}-\bar{M}_{12}\right)}{L\rho_{air}}$ with κ from 0.1 to 10.

APPENDIX G. CRITICAL TRANSPORT SPEED

We consider the web to be stationary in our analysis since the R2R processes for flexible and printed electronics are operated at extremely low speeds [1, 2] compared with their critical transport speeds. Since the web bending stiffness to tension ratio ε is very small, typically from 10^{-6} to 10^{-4}, so that we assume $\varepsilon \approx 0$ and use the critical transport speed of an axially moving string by Wickert and Mote [3] to estimate the effect of web line speed to web vibrations

$$U_{cr} = \sqrt{\frac{\int_{-b/2}^{b/2} N_{11}(x_3)dx_3}{\int_{-b/2}^{b/2} \rho_{web} dx_3}} = \sqrt{\frac{N_{11}^{ave}}{\rho_{web}}}. \tag{G.1}$$

The ratio of frequency of moving web $f^{(U_{11})}$ to frequency of stationary web $f^{(0)}$ is [3]

$$\frac{f^{(U_{11})}}{f^{(0)}} = 1 - U_{11}'^2, \tag{G.2}$$

where U_{11} is the web line speed,

$$U_{11}' = \frac{U_{11}}{U_{cr}} \tag{G.3}$$

is the normalized line speed. Thus, when the web line speed increases to its critical transport speed, the frequency of moving web reduces to zero.

Reference

[1] Krebs, F. C., Tromholt, T., & Jørgensen, M. (2010). Upscaling of polymer solar cell fabrication using full roll-to-roll processing. *Nanoscale, 2*(6), 873-886.

[2] Palavesam, N., Marin, S., Hemmetzberger, D., Landesberger, C., Bock, K., & Kutter, C. (2018). Roll-to-roll processing of film substrates for hybrid integrated flexible electronics. *Flexible and Printed Electronics, 3*(1), 014002.

[3] Wickert, J. A., & Mote Jr, C. D. (1990). Classical vibration analysis of axially moving continua. *ASME Journal of Applied Mechanics, 57*(3): 738–744.

VITA

Dan Feng was born in Wuhu, Anhui, China. He received his B. Eng. degree in Machine Design, Manufacturing, and Automation from School of Mechanical Science and Engineering at Huazhong University of Science and Technology, Wuhan, China in June 2009. His undergraduate research was supervised by Dr. Honghai Zhang and his thesis title was "Development and Experiments of Three-Dimensional Printing Fast Model Manufacture System", which was awarded as the Excellent Bachelor Thesis of Hubei Province. He graduated from University of Missouri-Columbia, Missouri, United State, with his M.S. degree in Mechanical Engineering in December 2012. He did his master's degree under Dr. Frank P. Pai with the thesis title as "Theory and Development of a Camera-Based Noncontact Vibration Measurement System". In August 2013, he enrolled at Purdue University to pursue a Ph.D. in Mechanical Engineering with Dr. Arvind Raman as his advisor. His research interests are in multi-physics for roll-to-roll and 3D printing processes.